THE UNIVERSITY OF
WARWICK

University of Warwick institutional repository: http://go.warwick.ac.uk/wrap

A Thesis Submitted for the Degree of PhD at the University of Warwick

http://go.warwick.ac.uk/wrap/3186

This thesis is made available online and is protected by original copyright.

Please scroll down to view the document itself.

Please refer to the repository record for this item for information to help you to cite it. Our policy information is available from the repository home page.

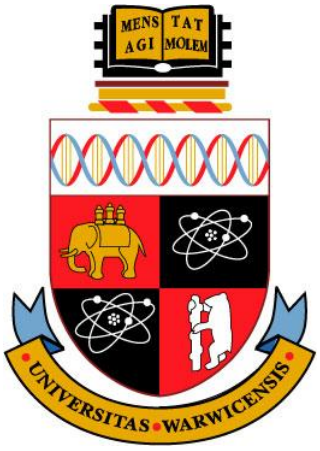

Development and Application of Evanescent Wave Cavity Ring-Down Spectroscopy as a Probe of Biologically Relevant Interfaces

by

Hayley Victoria Powell

A thesis submitted to the University of Warwick for the degree of Doctor of Philosophy

Molecular Organisation and Assembly in Cells Doctoral Training Centre

December 2009

Contents

List of Figures

Acknowledgments

I would like to say a huge thank you to my supervisor Prof. Pat Unwin. I would not have got this far without your undying patience, support and enthusiasm. You have been able to inspire and motivate me even when I feel like everything has gone wrong, and I have never left a meeting with you without feeling like I can conquer the world (at least the world of chemistry). Thanks also to Prof. Alison Rodger for your support, understanding and patience and for always having faith in me, and to Dr Stuart Mackenzie for many extremely helpful discussions and for all of your technical input to the project.

To Mathias, my lab-guru. Little did you know that on your first day as a PhD student at Warwick you would be teaching fellow cavity ring-downers (i.e. me) to make solutions! Hopefully I have come a long way since then, which is largely due to your help and support. Your attention to detail, depth of knowledge, and commitment to all that you do is an inspiration to me. You are a fantastic scientist and I have truly enjoyed every moment of working with you.

I would also like to extend my gratitude to Meiqin for all of your help in the lab. Thanks to Prof. Julie Macpherson and Dr. Teresa Pinheiro for all of your helpful discussions and great ideas, and to everyone else in the Warwick Electrochemistry Group and in MOAC for making the last three years good fun.

To Mum, Dad and Scott, you'll be pleased to hear my reign of perpetual studenthood has come to an end. Thank you for all of your love and support, particularly during my university years.

Last, but by no means least, my eternal love and gratitude (and apologies for being a complete nightmare over the last three years) goes to JDP. Put quite simply, I could not have got this far without you.

Declarations

The work contained within this thesis is my own except where outlined below. I confirm that this thesis has not been submitted for any degree at another university.

The experiments described in Chapter 4 were done in collaboration with Mathias Schnippering. The data for the polarisation-dependent EW-CRDS measurements of TMPyP adsorption at the silica-water interface shown in Figure 5.13 amd Figure 5.17 were supplied by Simon Neil of the Physical and Theoretical Chemistry Department at the University of Oxford. The remainder of the experiments in Chapter 5 were done in collaboration with Dr. Meiwin Zhang. The AFM images of the silica surface after the adsorption of cationic vesicles shown in Figure 6.5 and Figure 6.6 were acquired by Michael O Connell.

Parts of this thesis have been published or submitted for publication as detailed below:

Powell, H. V.; Schnippering, M.; Mazurenka, M.; Macpherson, J. V.; Mackenzie, S. R.; Unwin, P.R. "Evanescent Wave Cavity Ring-Down Spectroscopy as a Probe of Interfacial Adsorption: Interaction of Tris(2,2'-bipyridine)ruthenium(II) with Silica Surfaces and Polyelectrolyte Films", *Langmuir*, **2009**, *25*, 248-255.

Zhang, M.; **Powell, H. V.**; Mackenzie, S. R.; Unwin, P. R. "Kinetics of porphyrin adsorption and DNA-assisted desorption at the silica – water interface", submitted for publication.

Powell, H. V.; Schnippering, M; Cheung, M.; Macpherson, J. V.; Mackenzie,S. R.; Stavros, V.; Unwin, P. R. "A Novel Approach to Study Electron Transfer between Redox Proteins", in preparation.

Powell, H. V.; Zhang, M.; O' Connell, M.; Mackenzie, S. R.; Unwin, P. R. "Following the Formation of Supported Lipid Bilayers with Evanescent Wave Cavity Ring-Down Spectroscopy", in preparation.

Abstract

The application of a hybrid instrument combining Evanescent Wave Cavity Ring-Down Spectroscopy (EW-CRDS) with electrochemical and fluidic methods is described. The electrochemical/fluidic methods were used to induce a surface process, the effects of which were subsequently monitored *in situ* and in real time with exquisite spectral sensitivity and excellent temporal resolution by EW-CRDS. The well-defined manner in which the surface processes were initiated allowed the extraction of kinetic rate constants by fitting the EW-CRDS data to mathematical models of the surface process coupled to convection-diffusion.

The investigations described include: the study of the thermodynamics and kinetics of the adsorption of tris(bipyridine)ruthenium(II) ($[Ru(bpy)_3]^{2+}$) to polypeptide films using EW-CRDS with chronoamperometry; the real-time electrochemistry of cytochrome *c* immobilised on silica by EW-CRDS with chronoamperometry; the kinetics of adsorption and DNA-assisted desorption of 5,10,15,20-tetra(N-methylpyridinium-4-yl)porphyrin at the silica-water interface using EW-CRDS with an impinging jet flow cell; and the monitoring the adsorption of cationic phospholipid vesicles at the silica-aqueous interface and the interaction of 5,10,15,20-Tetraphenyl-21*H*, 23*H*-porphine-*p*,*p*′,*p*″,*p*‴-tetrasulfonic acid tetrasodium hydrate with the resulting bilayer also using EW-CRDS with an impinging jet flow cell.

The work described in this thesis provides a platform on which EW-CRDS can be used to study dynamics at biointerfaces, such as the association of ions, peptides, proteins and drugs with phospholipid bilayers, the electron transfer between redox enzymes in a biomimetic environment, and the lateral diffusion of protons, ions and proteins at biomembranes. Such studies are essential to the understanding of many important cellular processes in addition to the development and optimisation of a number of bio-inspired technologies.

Abbreviations

Abbreviation	Description
AFM	Atomic Force Microscopy
ATP	Adenosine Triphosphate
ATR	Attenuated Total Internal Reflection
CD	Circular Dichroism
CLSM	Confocal Laser Scanning Microscopy
CRDS	Cavity Ring-Down Spectroscopy
CT-DNA	Calf Thymus DNA
DOPC	1,2-dioleoyl-sn-glycero-3-phosphocholine
DOTAP	1,2-dioleoyl-3-trimethylammonium-propane
ECL	Electrochemiluminescence
ET	Electron Transfer
EW-CRDS	Evanescent Wave Cavity Ring-Down Spectroscopy
$FeEDTA^-$	Ethylenediaminetetraacetic acid iron(III)
FRAP	Fluorescence Recovery After Photobleaching
HPLC	High Performance Liquid Chromatography
PBS	Phosphate Buffer Solution
PGA	Poly-L-Glutamic Acid
PFV	Protein Film Voltammetry
PLL	Poly-L-Lysine

PMT	Photomultiplier Tube
QCM	Quartz Crystal Microbalance
QCM-D	Quartz Crystal Microbalance with Dissipation
RLS	Resonance Light Scattering
RR	Resonance Raman
RU	Response Units
$[Ru(bpy)_3]^{2+}$	Tris(2,2′-bipyridine) dichlororuthenium(II)
SECM	Scanning Electrochemical Microscopy
SICM	Scanning Ion Conductance Microscopy
SLB	Supported Lipid Bilayer
SNOM	Scanning Near-Field Optical Microscopy
SPR	Surface Plasmon Resonance
STED	Stimulated Emission Depletion Microscopy
SUV	Small Unilamellar Vesicles
TBACl	Tetrabutylammonium Chloride
TMPyP	5,10,15,20-tetrakis(4-N-methylpyridiniumyl)porphyrin
TPPS	5,10,15,20-Tetraphenyl-21H, 23H-porphine-p,p′,p″,p‴-tetrasulfonic acid
UME	Ultra Micro Electrode

Chapter 1. Introduction: Functionalised Interfaces and Biomimetic Surfaces

This thesis describes the application of a novel instrument combining the spectroscopic sensitivity of Evanescent Wave Cavity Ring-Down Spectroscopy (EW-CRDS) with modern electrochemical and microfluidic methods, to the study of reactions at biologically relevant interfaces. In this chapter, the importance of investigating the dynamics of processes occurring at these interfaces is outlined, followed by a description of some of the main techniques currently available to study them.

1.1 The Importance of Interfacial Science in Biological Systems: An Overview of Key Applications

Surfaces play an important part in many processes in a wide variety of scientific disciplines, and the life sciences are no exception. Studying the interactions between biological molecules and surfaces, and the interactions between molecules at surfaces is not only important for understanding a large number of intracellular processes, but also for optimising a wide-variety of biologically-inspired technologies such as biofuel cells and sensors. This section provides a brief overview of the kinds of dynamic processes that occur at cell membranes (and models thereof), followed by a description of some of the technologies being built that exploit these processes.

1.1.1 Understanding Cellular Processes at Membranes

Membranes are ubiquitous within the biological cell and constitute the stage on which many essential physiological processes occur. There is a rich chemistry associated with biomembranes due to their compositional and functional diversity. This section gives only a brief overview of some of these processes to give insight into how vast the subject is. For more information and references, the reader is referred to numerous books on the subject.[1]

The foundation of all biomembranes in the cell is a bilayer of amphiphillic molecules called phospholipids arranged such that the hydrophobic fatty acid chains are shielded from the aqueous cell environment by their hydrophillic head groups.[1] In addition, the membrane hosts a wide variety of proteins, carbohydrates and other molecules which are essential to a number of its roles.[1] Different membranes within the cell are composed of different phospholipids and contain different proteins in order to perform a variety of functions, such as intercellular communication, cell-cell adhesion between basolateral membranes, energy transduction at the inner mitochondrial membrane and photosynthesis at the thylakoid membrane.[1]

Biomembranes are an extremely dynamic environment. The membrane itself is believed to be more like a 2D fluid than a rigid structure in order to deal with mechanical and thermal stresses, and to allow the lateral diffusion of lipids and membrane-bound proteins.[1] Transport of material in and out of the cell is constantly regulated by the membrane: ions and small molecules can diffuse through the membrane passively, by protein facilitation, or actively transported by proteins. Larger molecules, including proteins, can be shuttled across the membrane through a process known as endocytosis.

As well as transverse movement of material through membranes, lateral diffusion of molecules is also important.[1] For example, the lateral diffusion of both ubiquinone and protons is important for respiration. Interactions of membrane-bound receptors with ligands such as nutrients, metabolites, hormones and neurotransmitters are integral to cell-signalling. Electron transport between chains of proteins, either embedded in the membrane or bound to the surface, is important in the peroxisome for the oxidative breakdown of amino acids and fatty acids, in the mitochondria for the synthesis of ATP for energy, and in the chloroplasts where energy is produced by photosynthesis. Binding of molecules (ions, peptides, proteins) to biomembranes is important and some soluble enzymes, such as protein kinase C, need to associate with the membrane to function and can do so in a number of ways (e.g. anchoring, by electrostatically binding, binding through hydrophobic interactions, through covalent binding to lipids, by fully embedding in the membrane) and can be affected by many factors.[1] Understanding all of these processes is not only fundamentally interesting, but is also essential for comprehending membrane related diseases.

1.1.2 Development and Optimisation of Bio-Inspired Technologies

For many of the industrial processes today, nature has an equivalent or alternative way of obtaining the same result: solar cells convert sunlight into energy just as photosynthetic organisms do,[1b] sensors detect chemicals just as cell surface receptors do,[1b] and photosynthetic reactions produce hydrogen[1b] just as electrocatalysis at metal electrodes does. This has inspired the use of enzymes, oligonucleotides, and microbes in the place of inorganic materials in sensors, fuel cells and electronics, as described in the ensuing sections.

1.1.2.1 Biosensors and Biofuel Cells

The term biosensor can be applied to sensors for biomolecules, or sensors that use biomolecules to enhance the sensitivity and/or selectivity of the device.[2] A typical biosensor may consist of a film containing biomolecules attached to a transducer in some manner. The transducer is generally optical,[3] acoustic[3b] or electrical[4] such as any of the techniques described in Section 1.2. The optimisation of biosensor devices not only requires significant understanding of the interaction between analyte and the layer on the transducer, but also the processes involved in creating the bio-layer in the first place, in order to ensure that optimum concentrations and orientations of biomolecules are achieved in the films. Biosensors now exist for a wide range of chemicals, for a diversity of applications, including in medicine, food industry, security and defence, and the environmental sciences.[5]

The endeavour to find alternate energy sources to fossil fuels has sparked the further development of fuel cells. In a conventional fuel cell, hydrogen is oxidised at an anode (often Pt) and the resulting protons combine with oxygen and electrons at the cathode to produce water. Nature already provides the means to convert chemical into electrical energy using enzymes. The use of enzymes for this conversion offers several possible advantages, including operation at near-room temperature and neutral pH, and selective catalytic activity[6] in addition to the ability to use low cost, renewable fuels. The development of full scale biofuel cells has, so-far, been hampered by the low efficiency, low power output and short lifetime of such devices.[6] However, one exciting and realistic possible application of biofuel cells is the development of low-power devices for implantation in the human body (e.g. for powering an implanted biosensor that can

transmit data to an external device) that can run off substances found in the body.[6-7] As in biosensors, one of the principle components of such biofuel cell devices is a biofilm which, in this case, catalytically converts chemicals (e.g. glucose) into electrical energy. Therefore, optimisation of such devices requires characterisation of the films, and the processes involved, by surface science techniques. Biofuel cells have been created based on plant cell walls,[8] using glucose oxidase[9] and haem proteins.[10] On a related note, conventional hydrogen fuel cells clearly need a steady supply of hydrogen to produce electrical energy. This is typically done by electrolysis at Fe or Ni electrodes, but the process requires high temperatures and high overpotentials. Since nature has created means of efficiently cycling hydrogen in cellular processes such as photosynthesis and respiration using enzymes, Armstrong's group has explored the possibility of exploiting these enzymes to produce hydrogen.[11]

1.1.2.2 Biocompatible Surfaces

Biocompatibility is obviously an essential property of implanted materials. Since the non-specific adsorption of proteins to the surfaces of implants is believed to initiate the body’s immune response against such implants, significant research has been conducted into the development of protein-resistant materials.[12] More recently, the focus has been towards the development of 'smart' materials that interact with their biological environment, for example to promote tissue regeneration.[13] Additionally, the development of materials resistant to bacterial adhesion for catheters and cannulas could help to reduce the number of hospital acquired infections.

1.1.2.3 High-Throughput Screening of Interactions - Microarray Technology

The desire to be able to perform high-throughput screening of biological interactions has led to the development of microarray technologies. Arguably the most well-known are the DNA-microarrays, used commonly to quantify gene expression levels in an organism, but protein arrays also exist for the screening of protein-protein and protein-ligand interactions. Development of these technologies requires surface science techniques for a number of reasons. Firstly, some kind of read-out mechanism is needed. Microarray technology currently relies on fluorescence imaging of gene chips to detect hybridisation, but the application of other techniques such as electrochemical methods or other optical methods[14] could provide label-free methods of transduction. Secondly, in order to make such technologies quantitative and comparable from one chip to another, a thorough understanding of the surface interactions is necessary.[14]

1.1.2.4 Chemical Separation and Purification

To build any of the technologies described above based on biomolecules, and to characterise protein structure and function, it is necessary to purify the biomolecules from cell culture. There are numerous separation and purification techniques, but those that are considered to be the most selective are those based on affinity interactions. For example, separation by affinity chromatography relies on the interaction of proteins with affinity ligands attached to the matrix in the column and thus requires knowledge of these interactions.[15] Moreover, interactions between the column matrix and potential foulants also needs to be understood so that they can be inhibited.[16]

1.2 Surface Sensitive Techniques Applied to Biological Systems

A wide-range of techniques are available for studying biological surfaces, each with intrinsic merits and weaknesses. There exists a vast array of techniques available to characterise the structure, properties and morphology of bio-interfaces including electron microscopy, atomic force microscopy, x-ray diffraction, x-ray photoelectron spectroscopy, nuclear magnetic resonance, and mass-spectrometry, to name but a few. Since this thesis is concerned with the dynamics of bio-interfaces, this section focuses only those techniques applicable to the study of reasonably fast processes.

1.2.1 Electrochemical Probes

A number of the important biological pathways, including photosynthesis and respiration, rely on the shuttling of electrons between redox proteins and redox couples. Thus, electrochemistry ought to be ideally suited to the study of important redox couples in regulated cellular metabolic pathways such as nicotinamide adenine dinucleotide (NAD^+/NADH), cysteine/cystine, and metalloenzymes.[17] Additionally, modified electrodes are increasingly being used as the format for biosensors, as described below, which is partly due to the low cost and ease of miniaturisation of electrical sensing. Another advantage over techniques such as fluorescence is that analytes can be detected without the need to label them.

1.2.1.1 Protein Film Voltammetry

Protein film voltammetry (PFV) has proven powerful for understanding the mechanisms of redox enzyme kinetics[18], the development of biosensors,[19] biofuel cells and for the production of hydrogen.[11] As suggested by the name, PFV involves the

coating of an electrode with a film containing redox proteins in such a way that the proteins can undergo electron transfer with the electrode allowing the elucidation of the intrinsic electron transfer characteristics of the protein. Many different enzyme electrode designs have been adopted, depending on the application, but the key challenges are to ensure that the enzyme is adsorbed in its native state and in an orientation in which electron transfer is promoted. Proteins may be directly adsorbed to the electrode,[20] adsorbed to films on the electrode surface (for example self-assembled monolayers,[21] lipid bilayers,[22] polymer films,[23] carbon nanotubes[24] and other nanostructures[25]), or even tethered to the surface.[26] PFV is believed to be a good way to interrogate redox proteins as many electron transfer processes in the cell occur at bilayer membranes which have a high electric potential gradient, and immobilisation on the electrode overcomes the problem of sluggish diffusion of large biomolecules to the electrode surface, allowing fast kinetics to be accessed.

PFV can be used to study the thermodynamics and kinetics of electron transfer between the electrode and the immobilised protein,[27] intramolecular electron transfer[28] and of any coupled reactions, such as those catalysed by the enzyme.[29] Enzyme electrodes are also increasingly being used as the format for biosensors, probably the most famous of which is the glucose biosensor[30] which uses glucose oxidase to detect blood glucose. Other examples include immunoassays for tumour markers,[31] DNA-based electrochemical sensors[32] for the sensing of DNA-damage,[33] sequence-specific DNA detection,[34] and the detection of *salmonella* bacteria.[35] Signal transduction can be achieved by a variety of electrochemical methods including potentiometry,[36] amperometry,[37] and impedance.[38]

1.2.1.2 Scanning Electrochemical Microscopy

Scanning Electrochemical Microscopy (SECM) is a scanning probe technique in which the current response is measured at the tip of an ultramicroelectrode (UME) held over a substrate. Comprehensive descriptions of the technique can be found in a number of books[39] and reviews[40] but only the basic concepts are described here. If the UME is held far from the substrate and a potential applied, the measured steady-state current is given by

$$i_{\infty} = 4nFDc^{*}a \qquad (1.1)$$

where c^{*} and D are the bulk concentration and diffusion coefficient of the mediator in solution, n is the number of electrons transferred per electrochemical reaction, a is the tip radius of the UME and F is Faraday's constant. The factor of 4 is due to the electrode geometry and is only true for a disc-shaped electrode embedded in an infinitely large insulating sheath. On bringing the UME very close to the substrate, the current is perturbed by two effects: the blocking of diffusion of mediator to the tip by the substrate, causing a decrease in current, and the regeneration of mediator at the surface causing an increase in current at the tip. The latter could occur because the substrate is an electrode held at a potential to re-oxidise/reduce the mediator back into its original redox state, or because the substrate is coated with a redox couple capable of returning the mediator back to its original state. Two main detection modes exist: the feedback mode where the tip acts as the source and detector of the mediator, and the generation-collection mode where the tip acts purely as a detector for mediator generated at the substrate. Both are shown schematically in Figure 1.1. Feedback mode is typically better for imaging as it has improved spatial resolution over generation-collection mode, whereas generation-

collection mode tends to have greater sensitivity. It is also possible to use a combination of both feedback and generation-collection modes as demonstrated by Zhao and Wittstock.[41]

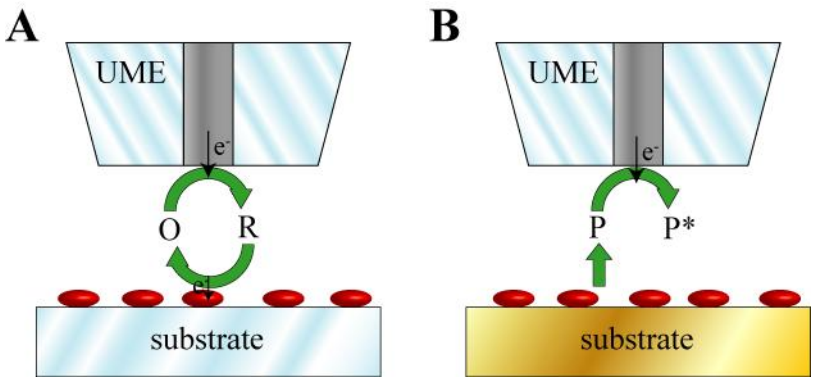

Figure 1.1 Schematic of the two main modes of operation of SECM. A) In feedback mode, oxidised mediator, O, is reduced (or equivalently oxidised) at the electrode to R, which is then re-oxidised (equivalently re-reduced) at the substrate surface. The regeneratioin of oxidised (equivalently reduced) mediator results in a greater current at the electrode. B) In generation-collection mode the product of a reaction at a substrate, P, is oxidised/reduced at the electrode to form P*. The current is thus a measure of the activity of the surface.

In both the feedback mode and generation-collection mode, the current is recorded as the UME tip is either scanned across a surface to produce a map of the topography and/or reactivity of the substrate, or moved perpendicular to the surface to produce an approach curve. Typical approach curves for a conducting substrate and a purely insulating substrate in feedback mode are shown in Figure 1.2. For a purely insulating (inert) substrate, the normalised current $I = i / i_{\infty}$ decreases as distance between the tip and substrate, d, decreases since diffusion is hindered causing a decrease in flux at the tip. For a conducting substrate, I increases with decreasing d due to the regeneration of mediator at the substrate surface causing greater fluxes at the tip. In general, the approach curve to an electrochemically active surface will lie somewhere in

between the curves shown in Figure 1.2A and Figure 1.2B. Clearly, at a constant d, the normalised current response is then a direct measure of the activity of the substrate and the surface reaction rate can be calculated.[42]

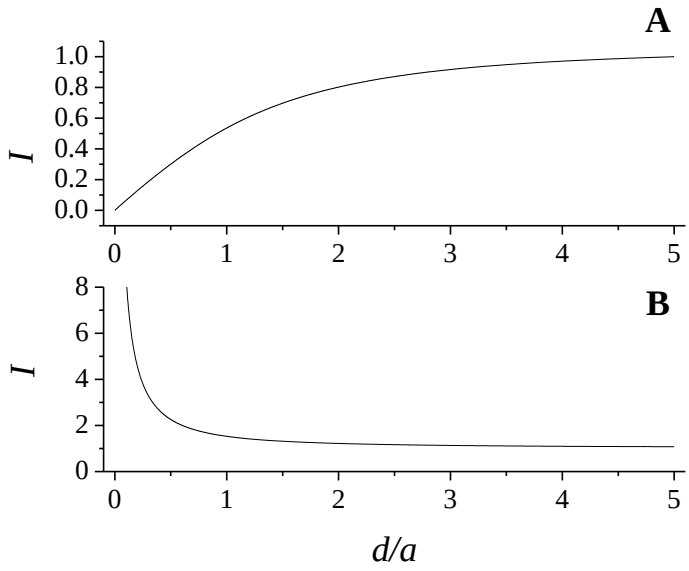

Figure 1.2 Normalised current response during an approach curve with A) a purely insulating and B) a conducting substrate.

There exist a large number of reports of the application of SECM to biological systems since the technique is non-destructive, allows the probing of a particular system repeatedly, and requires little or no pretreatment of the sample as in some optical techniques such as fluorescence. SECM has been succesfully applied to study a wide range of biological systems from multicellular organisms, to the activity of single cells and subcellular components, down to enzymes. Only a few of these applications are reported here to give a flavour of the types of systems studied. For further information the reader is referred to recent reviews on the subject.[40, 42-43]

SECM has been applied to the study of living cells by immobilising cells onto a substrate. In the generation-collection mode the consumption or production of chemicals during a number of cellular processes has been monitored. O_2 is a common species to monitor as it is involved in a wide variety of pathways. For example, O_2 production gives information on the rate of photosynthesis in plant leaf structures,[44] and respiration rates can be inferred from O_2 consumption.[45] Another interesting application has been to the study of exocytosis of adrenaline from chromaffin cells.[46] SECM has also been used to study the redox properties of immobilised enzymes, including cytochrome *c*, [47] glucose oxidase, [48] and horse radish peroxidase.[49] Imaging of patterns of surface-immobilised enzymes using SECM is important to the characterisation and optimisation of enzyme based sensors[50] and for the formation of biosensors, for example for the detection of breast cancer markers.[51]

1.2.1.3 Scanning Ion Conductance Microscopy

A closely related technique to SECM is Scanning Ion Conductance Microscopy (SICM).[52] In SICM, a micropipette in an electrolyte solution is employed as a probe. The ionic current between an electrode in the micropipette and an electrode in the electrolyte solution outside of the pipette is measured as the pipette is scanned over a surface or perpendicularly approaches a surface (see Figure 1.3). Surface topography can be determined from a scan as the conductance decreases as the distance between the surface and pipette decreases due to hindrance of the migration of ions into the pipette by the surface. SICM can also be used to monitor ion fluxes at a substrate and for the controlled delivery of substances to a substrate.[53]

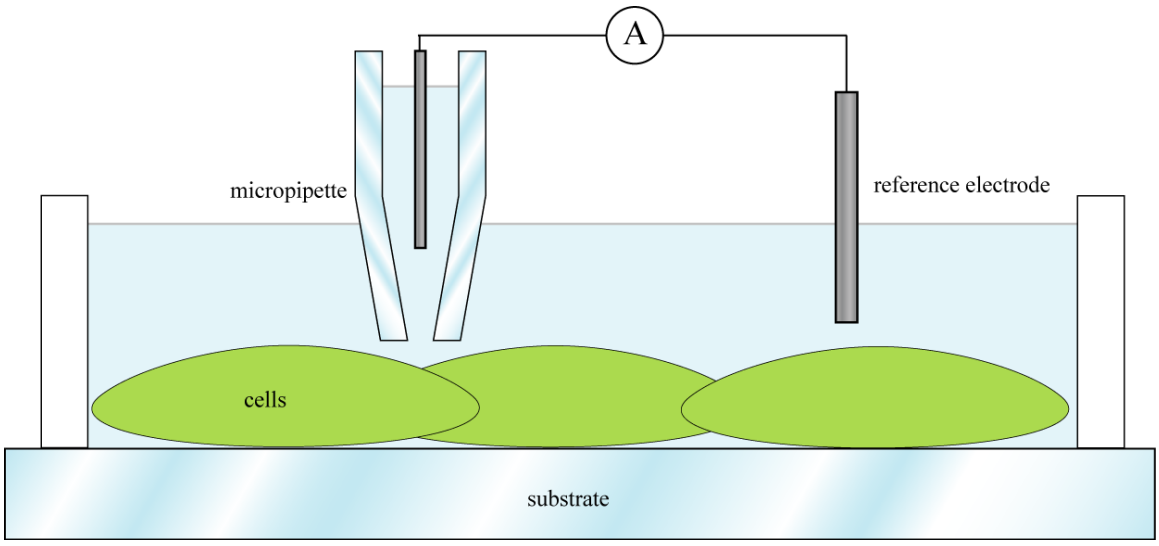

Figure 1.3 Schematic showing the operation of SICM. A micropipette is scanned across the sample surface whilst the ionic current between an electrode within the pipette and a reference electrode outside of the pipette is recorded.

SICM has been used to study biological samples as, like SECM, it is non-invasive and non-destructive, and has high spatial resolution. Unlike SECM, SICM does not require the use of potentially cytotoxic redox mediators and the media in which SICM operates is not too important provided there are plenty of ions. Examples include the study of the endocytotic pathway,[54] and the study of cardiomyocyte morphology with changing Ca^{+} concentrations.[55] Both SECM and SICM can be used for the controlled localised delivery of materials. However, with SICM delivery is not restricted to substances that undergo electron transfer with the electrode, permitting a greater variety of substances to be studied. SICM combined with confocal laser scanning microscopy has been used to monitor diffusion within the plane of the membrane.[56] Controlled delivery is also important in the fabrication of miniaturised arrays for protein or DNA assays.[57] In addition to being combined with confocal laser scanning microscopy, SICM

has been combined with scanning nearfield optical microscopy for the imaging of live cells.[58] SICM can also be used to study the mechanical properties of membranes in a non-contact manner.[59]

1.2.2 Quartz Crystal Microbalance

The quartz crystal microbalance (QCM) technique uses acoustic waves formed at a surface. There are many different variations of the technique which are reviewed in Čavić *et al*.[60] Only one of the most commonly used set-ups is described here for illustrative purposes. A sensor crystal made of quartz is sandwiched between two electrodes which are used to induce shear oscillations in the quartz by applying an alternating voltage. The resonant frequency of the quartz is dependent, amongst other parameters, on the mass of the crystal. Therefore, addition of mass to the crystal due to adsorption of an analyte to the surface, results in a change in the resonant frequency. Provided the adsorbed film is thin and rigid in nature, it is possible to determine the adsorbed mass, Δm, from the change in resonant frequency, Δf, using the Sauerbrey equation:

$$\Delta f \approx \frac{-2 f_0 \Delta m}{A\sqrt{\rho_q \mu_q}} \tag{1.2}$$

where f_0 is the sensor resonant frequency, A is the sensor area, and ρ_q and μ_q are the density (2.648 g cm^{-3}) and shear modulus (2.947×10^{11} dyne cm^{-2}) of AT-cut quartz.[61] Typical mass sensitivities at the quartz-liquid interface for commercial instruments are in the range of 1 ng cm^{-2}. For thick or non-rigid films the Sauerbrey equation tends to incorrectly calculate the mass, therefore it is also necessary to measure the variation of other parameters such as the dissipation, which is achieved by measuring the decay in the

oscillations once the alternating voltage has been shut off. These extra parameters can be used to determine the viscoelastic properties of the film, however more complex models of viscoelastic films then need to be used.[62]

Quartz crystal microbalance with dissipation, QCM-D, has been used to study the kinetics of a multitude of biologically relevant interactions.[60, 63] Investigations include interactions of proteins with a wide variety of surfaces including Au, [64] polymer films[65] and phospholipid layers,[66] and antibody-antigen interactions[67] for the development of immunosensors. Examples include sensors for proteins such as human serum albumin,[67-68] immunoglobulin G,[69] and the antibodies against African swine fever virus attachment protein,[70] and for single-celled organisms such as the foot and mouth disease virus,[71] Chlamydia trachomatis,[72] and Salmonella paratyphi A.[73] QCM has been investigated for use as a transducer in nucleic acid assays for the detection of DNA hybridisation[74] and the detection of single nucleotide mismatches.[75] QCM has also found use in the pharmaceutical industry for drug discovery by monitoring the binding of proteins and molecules to nucleic acids. Examples include the interaction of peptides with HIV RNA for anti HIV drug,[76] and the binding of platinum[77] and ruthenium[78] complexes, and other intercalating molecules[79] with DNA. The adhesion of cells to surfaces has been studied for biosensor applications and for development of biocompatible materials. Examples include the adsorption of osteoplasts, [80] epithelial cells[81] and platelets.[82]

1.2.3 Fluorescence Methods

Fluorescence microscopy offers numerous advantages over other techniques for biological applications, such as the ability to monitor samples in physiological conditions, and the ability to collect data instantaneously. It provides greater contrast and

thus produces improved images over conventional microscopy, and the advancement in optical technologies has improved the spatial resolution down to the nanometre scale, enabling single particle tracking.[83]

A wide variety of fluorescent techniques are applied to biological systems including fluorescence recovery after photobleaching for monitoring diffusion,[84] fluorescence resonance energy transfer for determining intermolecular and intramolecular distances,[85] fluorescence lifetime for studying the environment of molecules,[86] and fluorescence polarisation for determining molecular orientation.[86b] These techniques can be used with a variety of microscopes including those based on wide-field illumination and total internal reflection, but in this section only those that have provided a significant breakthrough in spatial resolution, confocal laser scanning microscopy and scanning near-field optical microscopy, are described because this increase in spatial resolution has led to the advancement of single particle studies. Other high resolution techniques to these two exist such as stimulated emission depletion microscopy (STED),[87] but the following discussion is limited to the most commonly used techniques. Overviews of other fluorescent techniques can be found elsewhere.[83, 88]

1.2.3.1 Confocal Laser Scanning Microscopy

Confocal laser scanning microscopy (CLSM) is a type of optical microscopy in which pinholes are used to improve the spatial resolution of the conventional wide-field fluorescence microscope (Inventor Marvin Minsky - U.S.Patent No. 3013467). The pinholes ensure that only light in the plane of focus is incident on the detector. In this way a three-dimensional image of a sample can be acquired (see Figure 1.4). The pinhole also serves to reject background light thus optimising signal-to-noise. Theoretically,

provided that the pinhole is much smaller than the laser spot size, a 1.4 fold improvement in spatial resolution is possible.[83, 89] Resolution down to 200 nm has been reported.[90]

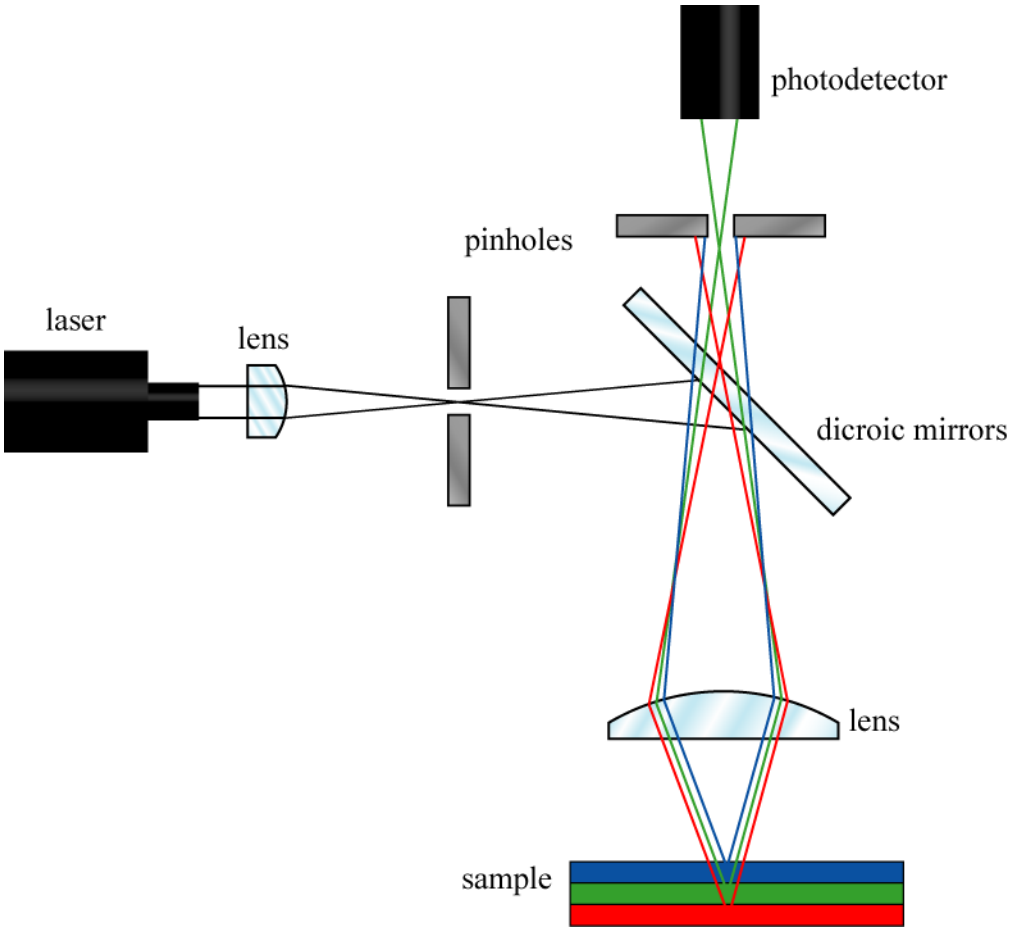

Figure 1.4 Schematic of the experimental set-up for CLSM. The pinholes ensure that only light in the plane of focus (in this case from the green layer of the sample) is incident on the detector reducing background noise and allowing 3D images of the sample to be constructed.

CLSM has been applied to the study of enzyme conformation dynamics and interactions with molecules,[91] as well as to RNA folding[88b] and catalysis by surface-immobilised ribozyme.[92] In practical applications, CLSM has proved useful in the pharmaceutical industry[93] for the study of drug release from water/oil/water emulsions,[94] pellets,[95] and from microspheres,[96] protein adsorption at oil-water interfaces,[97] on

microspheres,[98] and in chromatographic matrices[99] and for imaging the effect of drugs *in vivo*.[100]

1.2.3.2 Scanning Near Field Optical Microscopy

Although CLSM improves on the spatial resolution achievable by wide-field optical microscopy due to the Rayleigh criterion, the invention of Scanning Nearfield Optical Microscopy (SNOM) provided further improvement on the spatial resolution to in the region of 50 nm. In addition, SNOM can provide topographical information in addition to information from the optical signal. A review of the concepts of SNOM can be found in the review by Dunn[101] and those are only briefly described here.

In SNOM an apertured or apertureless probe is employed to obtain the spatial resolution. The former is more commonly used for reasons to be described later. In apertured SNOM, light is coupled into an optical fibre which is pulled at one end to form a small aperture probe (see Figure 1.5). The probe is often coated in aluminium to reduce light leakage and is scanned over a surface at a height of approximately 5-10 nm. The spatial resolution is determined by the size of the aperture which is typically 20-120 nm in size. The resolution is such that single-molecule detection experiments have been reported.[102] The transmitted or reflected light is then collected in the far field using a lens. There are a number of variations on this set-up depending on whether the probe is used as the light source or detector or both. A review of the concepts of apertured SNOM can be found in Hecht *et al.*[103] The distance of the probe to the sample is controlled using an indirect feedback mechanism based on shear-force damping and therefore topography can be mapped in addition to the collection of chemical information from the optical signal. In apertureless SNOM, more commonly referred to as photon scanning tunneling

microscopy, a strongly confined optical field is created at a sharp tip by an external light source and the tip is scanned over the substrate.[104] This is less popular than apertured SNOM as the near-field signal has to be extracted from the background of far-field scattering and the theory is much less well-understood.

The majority of applications of SNOM in the life sciences has been to obtain high resolution images[101, 105] of cells (e.g. fibroblasts,[106] human breast adenocarcinoma,[107] neurons,[108] bacteria[109]), viruses,[110] membranes (e.g. to capture domains,[111] imaging plant cell walls for biofuel cells,[8] localisation of photosynthetic proteins[112] and receptors in neurons[113]), human chromosomes[114], and DNA.[115] However, SNOM could prove important to the study of membrane dynamics and has successfully been applied to the study of the distribution and fluorescence lifetime of light harvesting complexes in thylakoid membranes,[116] distribution and clustering of proteins in membranes (with the possibility to study in response to stimuli), dynamics of cell surface receptors,[117] single molecule diffusion,[118] and protein transport kinetics at a single nuclear pore.[119] The ability to study rotational and diffusion dynamics of dyes in films could have potential for biomolecules.[115b]

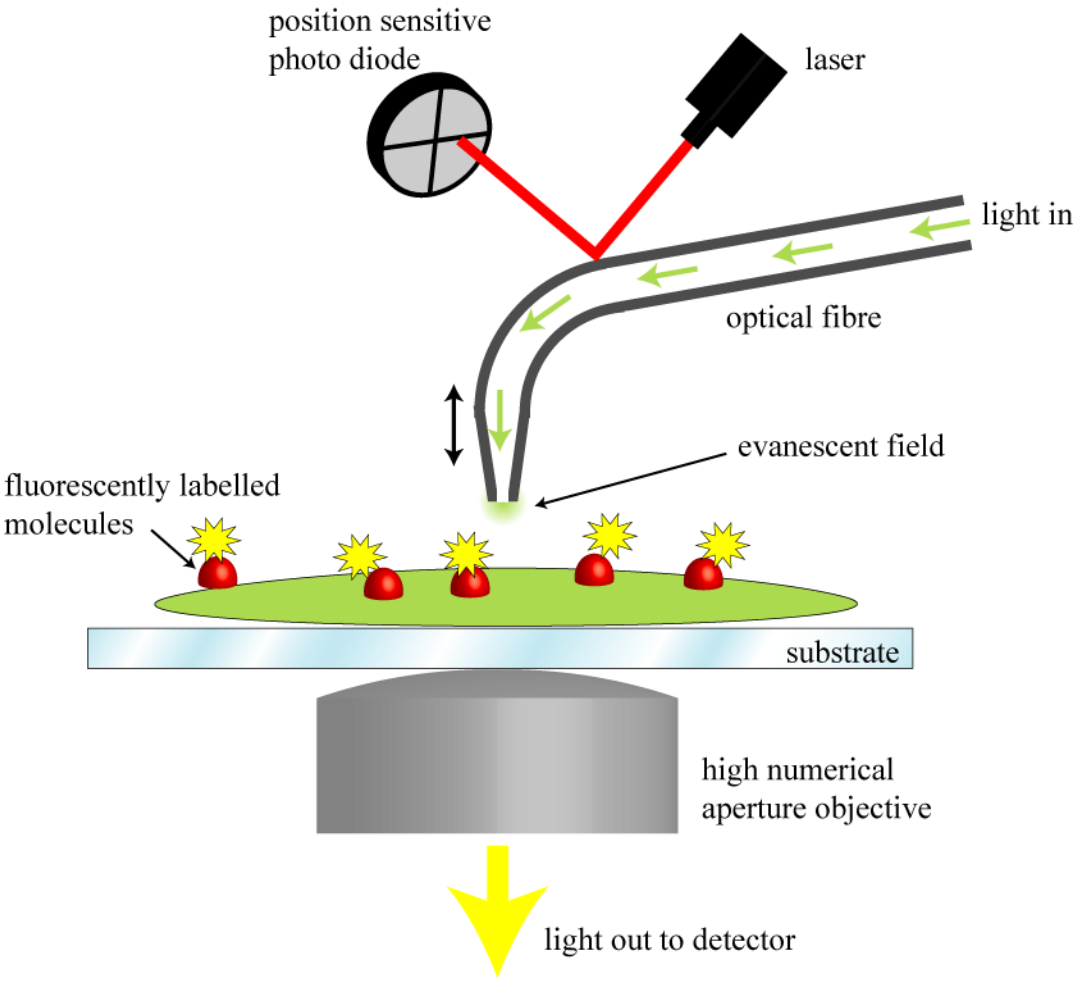

Figure 1.5 Schematic of the SNOM apparatus using an apertured probe (in this case a tapered optical fibre covered in Al) and collecting light in the transmission mode. The probe is held tens of nanometres from the sample surface so that the evanescent field formed at the end of the probe can excite fluorescent molecules in the sample. The resulting fluorescence is collected by the objective as the probe is scanned over the sample to produce an image. The probe-sample distance is kept constant by monitoring the changes in the amplitude of oscillations induced at the tip in a similar manner to atomic force microscopy by detecting the position of light reflected from the back of the probe using a position sensitive photodiode.

1.2.4 Spectroscopic Techniques Based on Total Internal Reflection

Light incident on the interface between media of different refractive indices is refracted when the angle of incidence is less than a critical angle given by $\theta_c = \sin^{-1}(n_1 / n_2)$ where n_1 and n_2 are the refractive indices of the media. Beyond this angle, the light is totally internally reflected and an evanescent wave is formed. Total internal reflection spectroscopy exploits this evanescent wave as a spectroscopic probe. In the same way as conventional spectroscopy, light absorbed from the evanescent field results in a decrease in the intensity of the totally reflected light and thus the absorbance in the evanescent field can be calculated using the Beer-Lambert Law. Since the penetration depth of the evanescent field is of the order of the wavelength of the light used, only species in the immediate vicinity of the interface are detected making it ideal for studying surface processes.

The sensitivity of the total internal reflection technique can be improved by the formation of multiple total-internal reflection points (i.e. multiple evanescent fields) along a waveguide, as in attenuated total internal reflection spectroscopy,[120] using fluorescence,[121] or by using surface plasmons as described below.

1.2.4.1 Surface Plasmon Resonance

Surface plasmon resonance (SPR), is a type of total internal reflection spectroscopy which uses the excitation of surface plasmons to enhance the sensitivity. A thin layer of a noble metal (or a monolayer of metal nanoparticles) is deposited at the total internal reflection interface. The percentage of light transmitted is dependent on the angle of incidence when this angle is greater than the critical angle. At a certain angle, known as the SPR angle, the reflected light intensity is at a minimum due to the

resonance between the wavevector of the light and that of the surface plasmons in the metal film. The SPR angle is highly dependent on the refractive index of the immediate environment of the thin metal film and thus is sensitive to the adsorption of materials at the interface. In the SPR technique, this change in angle is measured and is reported in response units (RU) which are typically equivalent to a shift in the SPR angle by 10^{-4} degrees. The change in SPR angle has been shown to be satisfactorily linear with the surface concentration of adsorbed material on the metal film and thus can be used to provide a quantitative measure of the amount of adsorbed material. For more information on the concepts of SPR, the reader is referred to a number of reviews.[122]

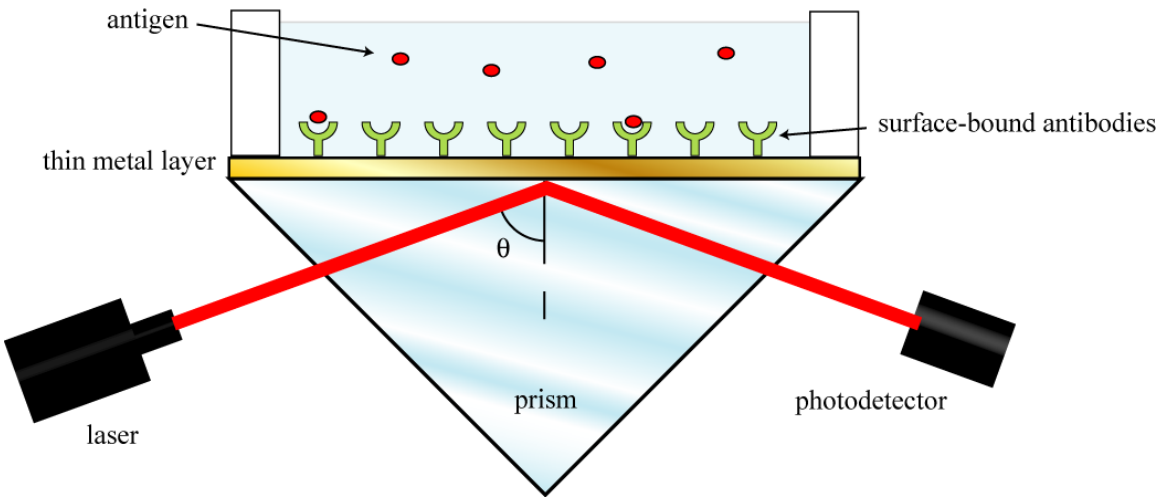

Figure 1.6 Schematic of the principles behind SPR. It is possible for light incident at the prism-solution interface to excite surface plasmons in the metal layer. The degree of excitation is dependent on the wavelength of light, the angle of incidence and the refractive index of the solution in the immediate vicinity of the total internal reflection event. For a given wavelength, the angle at which maximum resonance is achieved, the SPR angle, is a measure of the refractive index at the surface, which in turn is a measure of the concentration of species asdorbed at the surface. In this illustration, the binding of antigen to surface-immobilised antibody changes the refractive index and thus the SPR angle. Monitoring the amount of antigen bound with time allows the determination of the kinetics of association.

SPR can be used to determine the kinetics of association and dissociation at the total internal reflection interface. Systems that have been studied include DNA hybridisation,[123] DNA-protein interactions,[124] protein-protein interactions,[125] and the binding of proteins to phospholipid vesicles.[126] More recently, the SPR technique has been expanded for use in microarray technologies, including as the detection method[127] and for characterisation of the arrays.[128] SPR is also increasingly being used as the transducer in many biosensors,[122, 129] and has been applied to the detection of a range of size of analytes in a variety of disciplines. Small analytes relevant to the environmental sciences such as the herbicides atrazine[130] and simazine,[131] have been detected in water samples, biosensors for morphine[132] and methamphetamine[133] have been developed for the medical sciences and detectors for food contaminants such as fumonisin[134] and streptomycin in milk[135] have been developed for the food science industry. SPR has also been applied successfully to the detection of large analytes such as the foodborne pathogens *Escherichia coli*,[136] *Salmonella enteritidis*[137] and *Listeria monocytogenes*.[137]

1.3 Cavity Ring-Down Spectroscopy

1.3.1 Overview

Originally intended as a method to determine the reflectivity of highly reflective mirrors,[138] for applications in the aerospace industry,[139] and for the construction of low gain laser systems[140], the cavity ring-down technique was first applied to make spectroscopic measurements by O' Keefe and Deacon in 1988.[141] The technique has been exceptionally successful in ultrasensitive gas-phase absorption measurements in a variety

of situations including atmospheric modelling studies, pollution monitoring, and combustion studies.[142] Using CRDS, sub-ppb absorbances can be measured without the need for long path lengths, on the order of kilometers, as used in techniques such as differential optical absorption spectroscopy.[143]

In the following sections, the cavity ring-down technique is described, and the extension of the technique to sensitive condensed phase spectroscopic measurements is briefly reviewed. More detailed accounts on the history of the technique can be found in Chapters 5 and 6 of Busch and Busch,[142] and in several review articles.[144] There are also a number of reviews on experimental set-ups, principles and applications of CRDS.[145]

1.3.2 How The Technique Works

The cavity ring-down technique, in its simplest form, is shown schematically in Figure 1.7. In this set-up, the output of a light source (this could be a laser or a broadband source) is coupled into a stable (for a friendly discussion on the stability of optical resonators see Chapter 3 of Busch and Busch[142]) optical cavity consisting of two plano-concave high reflectivity mirrors. If the range of wavelengths of the light source overlaps modes within the cavity, the light will resonate within the cavity causing the intensity to build up (essentially, a mode of a cavity is a field which reproduces itself upon one round trip of the cavity and arises due to constructive interference of the beam with itself. We do not discuss this concept here, as in our experimental set-up, the existence of modes was not a problem, but if it is of interest, the reader is referred to Chapter 4 of Busch and Busch[142] or Kogelnik[146]). Once the intensity has reached a plateau, the source is turned off (or blocked), after which the intracavity light intensity decays exponentially with time due to transmission of light through the cavity mirrors. The intensity of light in the cavity

is typically monitored by measuring the transmission through one of the mirrors using a photo-sensitive detector, such as a photomultiplier tube or a photodiode, as shown in Figure 1.7. The exponential decay of light intensity is characterised by the cavity background ring-down time, denoted τ_0, which is defined as the time taken for the light to decrease by a factor of e^{-1}. τ_0 relates to the mirror reflectivity, R, and the cavity length, L, in the following way

$$\tau_0 = \frac{L}{c(1-R)} \tag{1.3}$$

where c is the speed of light. An absorbing species present in the cavity will contribute further to losses, causing the light to decay faster and resulting in a new ring-down time, τ. The optical absorbance per pass of light through the cavity, A, can be shown to satisfy[142]

$$A = \log_{10}(e)\frac{L}{c}\left(\frac{1}{\tau} - \frac{1}{\tau_0}\right), \tag{1.4}$$

where the term $\log_{10}(e)$ appears to convert to the conventional log scale used to define the absorbance.

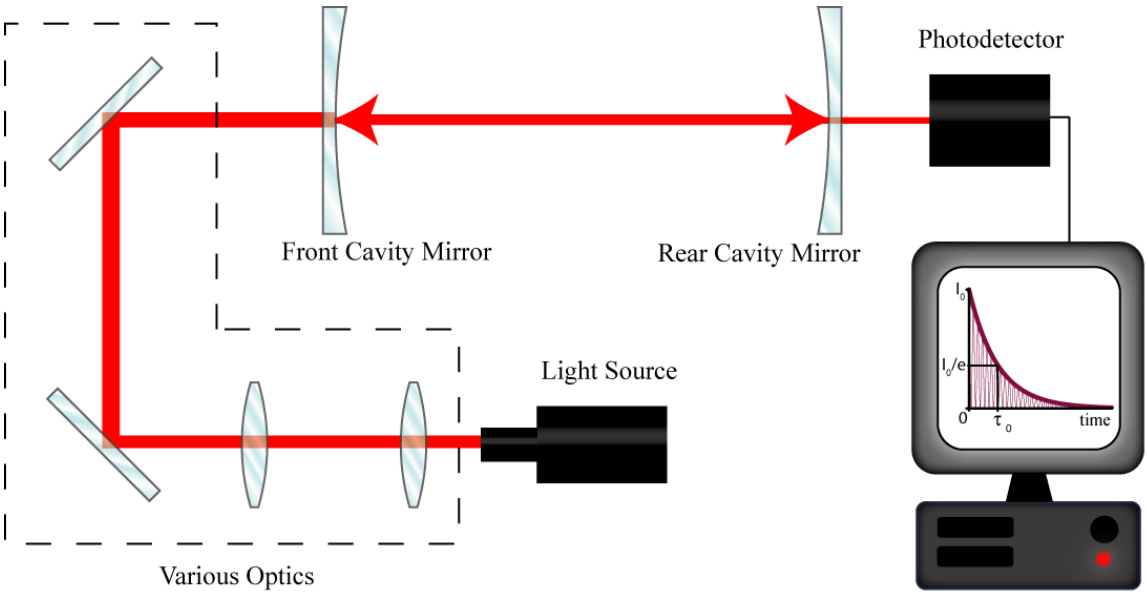

Figure 1.7 Schematic of the experimental set-up of a cavity ring-down spectrophotometer.

1.3.3 Condensed Phase CRDS

Although initially intended as a gas phase technique,[144b, 145a, 145d, 147] there have been a number of adaptations of CRDS to the condensed phase. Probably the most straightforward approach to liquid phase CRDS involves placing the solution inside the cavity allowing the direct contact of the solution with the mirrors.[148] The problems with this approach are the high scattering coefficients of the solution, limiting the minimal detectable absorbance, and potential damage to the expensive high-reflectivity mirrors, although the former can be overcome by careful choice of solvent.[148a] Other attempts have included coating the mirrors with the species of interest as seen in the study of iodine monolayers by Kleine *et al.*,[149] and inserting a measurement cell into the cavity at the Brewster angle in order to minimise losses due to reflection and scattering by the cell.[150]

By far the most popular approach to condensed phase CRDS is to exploit the phenomenon of total internal reflection using Evanescent Wave Cavity Ring-Down

Spectroscopy (EW-CRDS). The first attempt of this kind was the study of submonolayer chemisorbed I_2 by Pipino *et al.*[151] A fused silica Pellin-Broca prism was incorporated into the cavity arrangement and used as the total internal reflection element. The adsorption of I_2 to silica was probed by the evanescent field formed at the point of total internal reflection. The same group has also devised a number of novel cavity arrangements involving monolithic resonators.[152] In this set-up, the evanescent fields formed at the points of total internal reflection were used to probe the absorbance of the species of interest. Several other cavity geometries based on the same principles have been devised and applied to the study of adsorbed iodine,[153] monitoring the growth of amorphous semiconductor films,[154] determining the structure of a H_2O monolayer on SiO_2,[155] determining the absolute surface coverage of organochlorides adsorbed on SiO_2,[156] and studying the OH stretching overtones of adsorbed HNO_3.[157]

Arguably the simplest forms of EW-CRDS are the folded cavity and the ring-cavity, both of which were used in the experiments described herein. In both set-ups, the cavity consists of two high reflectivity mirrors and a total internal reflection element, normally a prism. They are both shown schematically in Figure 1.8. In the ring-cavity, the light enters through the front mirror, is reflected from the back mirror into the prism where it is totally internally reflected back onto the front mirror. The light path is triangular which permits only one pass through the sample per trip around the cavity. In general, the light does not enter the prism perpendicular to the interface, making it necessary to coat the entrance and exit faces with anti-reflective coatings to minimise reflection losses from these faces. These two drawbacks can be overcome by using the folded cavity arrangement. Here, the light traces an L-shape, passing through the sample

twice for each full trip around the cavity as shown in Figure 1.8. The light enters and exits the prism faces at 90º to the surface, negating the need for antireflective coatings, the advantages of which are the ability to couple broadband sources into the cavity, the ability to perform polarisation-dependent measurements, and the extension of the type of modifications that can be made to the probe surface. This set-up also has its disadvantages. Firstly, the calculation of the ring-down time from transients is complicated because three optical cavities are effectively set-up: one within the prism, and one cavity either side of the prism, resulting in a multi-exponential decay. Secondly, the prisms for the folded cavity have to be custom-made, so are less readily available and cost effective than the commercially available prisms for the ring-cavity.

The ring-cavity and folded-cavity EW-CRDS techniques have been used extensively to study various phenomena at the prism-solution interface. Shaw *et al.* studied the pH dependence of adsorption of Crystal Violet at the silica-aqueous interface in a folded cavity arrangement.[158] The adsorption of Crystal Violet was also used to characterise the silanol groups on the silica surface by Fan *et al.*[159] A pH-dependent fluorophore tethered to the silica surface was used to probe the interfacial pH as a function of bulk solution pH,[160] while polarisation-dependent measurements were used to determine the orientation of hemoglobin at the silica-water interface by Everest *et al.*,[161] and a similar set-up was used to detect hemoglobin in urine samples[162]. Adsorption at the silica-CH_3CN interface was considered by Fan *et al.*[163] The orientation of methylene blue at the air-silica interface was studied by Li and Zare.[164] EW-CRDS was used by Hannon *et al*. to determine diffusion coefficients of water and other solvents in poly(dimethylsiloxane) films.[165] The detection of fibronectin using EW-CRDS was

described by Wang *et al.*[166] The application of EW-CRDS to the analytical sciences[167] and in particular as a detector for HPLC [168] has also been described.

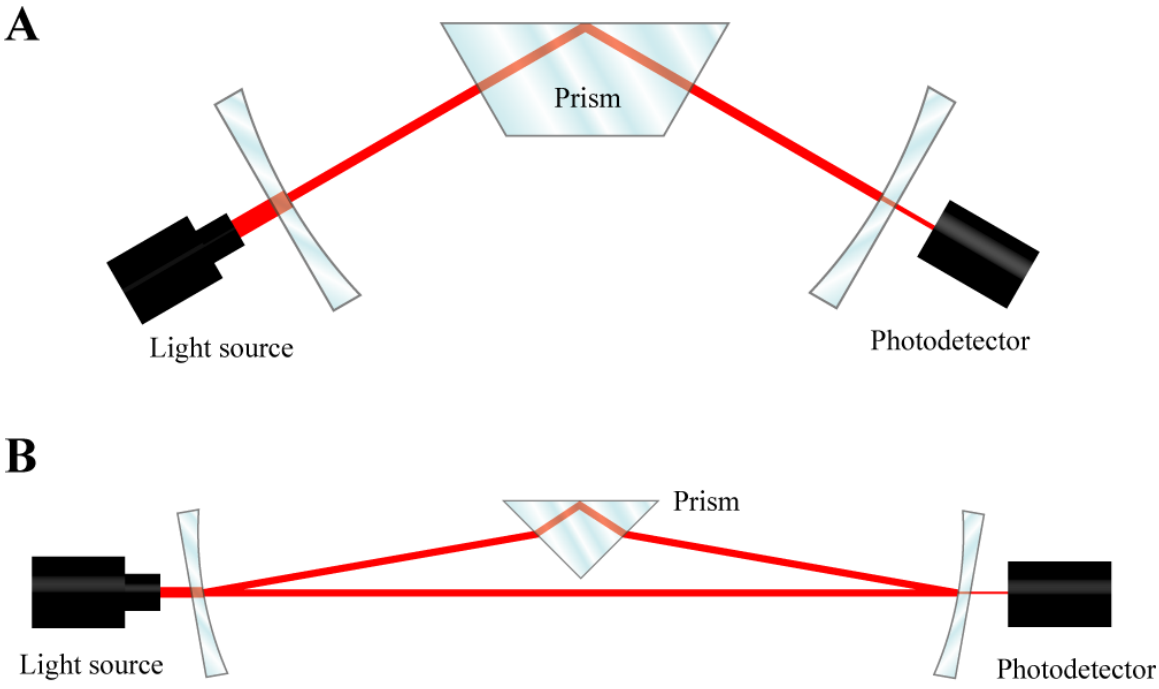

Figure 1.8 Schematic of the most typical cavity geometries employed in the EW-CRDS set-up. A) Folded cavity. B) Ring cavity.

A final variant of the EW-CRDS worth mentioning involves the use of optical fibres as the cavity.[169] In such set-ups, light travels around a ring of optical fibre and two couplers, one for input and one for output, take the place of the mirrors. The ring-down time in the optical fibre cavity will depend on the split ratio of the couplers. A taper is spliced into a region of the fibre to form the sensing area. This technique and a slight variant, phase-shift fibre-loop ring-down spectroscopy,[170] have been used as detectors for capillary electrophoresis of biomolecules,[171] and for single cell detection.[172] The attraction of this form of cavity ring-down lies in the relatively low cost as many of the parts are available cheaply from the telecommunications industry, and due to the good

detection limits which are possible from very small volumes of analyte (down to 700 picolitres of solution).[170b]

1.4 Mass Transport in Interfacial Dynamics

When studying the kinetics of reactions at interfaces, it is necessary to develop an understanding of the mass transport involved. Figure 1.9 shows a schematic of the processes occurring during a surface reaction (R converted to P) that all need to be considered when determining rate constants since any one of these steps can be rate limiting. The observed rate constant extracted from experiment will be a convolution of the rate constants of all of these processes. The mass transport step shown in Figure 1.9 can occur by diffusion, convection and migration. Although effects due to convection and migration can often be limited through experimental design, diffusion is always present. Diffusion arises due to reactant being consumed (and product being produced) at the surface due to the surface reaction which creates a gradient in the concentrations of both reactant and product within the interfacial region. The concentration of reactant (and product) in solution obey Fick's Laws of diffusion. Fick's first Law relates the diffusive flux of species *i*, J_i, to the concentration gradient, ∇c_i, by the equation[173]

$$J_i = -D_i \nabla c_i \qquad (1.5)$$

where D_i is the diffusion coefficient of species i. Fick's second law describes how the concentration develops with time[173]

$$\frac{\partial c_i}{\partial t} = D_i \Delta c_i \,. \qquad (1.6)$$

In situations involving only diffusion, if the reaction on the surface proceeds more slowly than diffusion to the surface, the reaction is said to be kinetically controlled. In this case, the rate limiting process is the reactive step meaning that by solving the diffusion equation coupled to appropriate boundary conditions, the actual surface reaction rate constant can be obtained. In some situations, the surface reaction may proceed in a diffusion-limited manner where the reaction is so fast that as soon as reactants are incident on the surface they are converted to product. In this case it is not possible to determine the rate constant from the data. However, it is possible to increase mass transport by adding convection (movement induced by mechanical force e.g. stirring), causing the reaction to become kinetically controlled. Calculating the rate constant in this case requires solving the convection-diffusion equation

$$\frac{\partial c_i}{\partial t} = D_i \Delta c_i - \underline{v} \cdot \nabla c_i \tag{1.7}$$

where the vector $\underline{v}$ describes the solution velocity. Convection can be induced by stirring or by flowing of solution as employed in the experiments in Chapters 5 and 6. The velocity vector, $\underline{v}$, can be calculated by solving the appropriate fluid dynamics equations. In general, this will be the steady-state incompressible Navier-Stokes equations for momentum balance and continuity[173]

$$\rho \underline{v} \cdot \nabla \underline{v} = -\nabla p + \eta \Delta \underline{v} \tag{1.8}$$

$$\nabla \cdot \underline{v} = 0 \tag{1.9}$$

where ρ is the density, p is the pressure and η is the dynamic viscosity. Clearly, to solve equations (1.8) and (1.9), the flow must be well-defined and not turbulent.

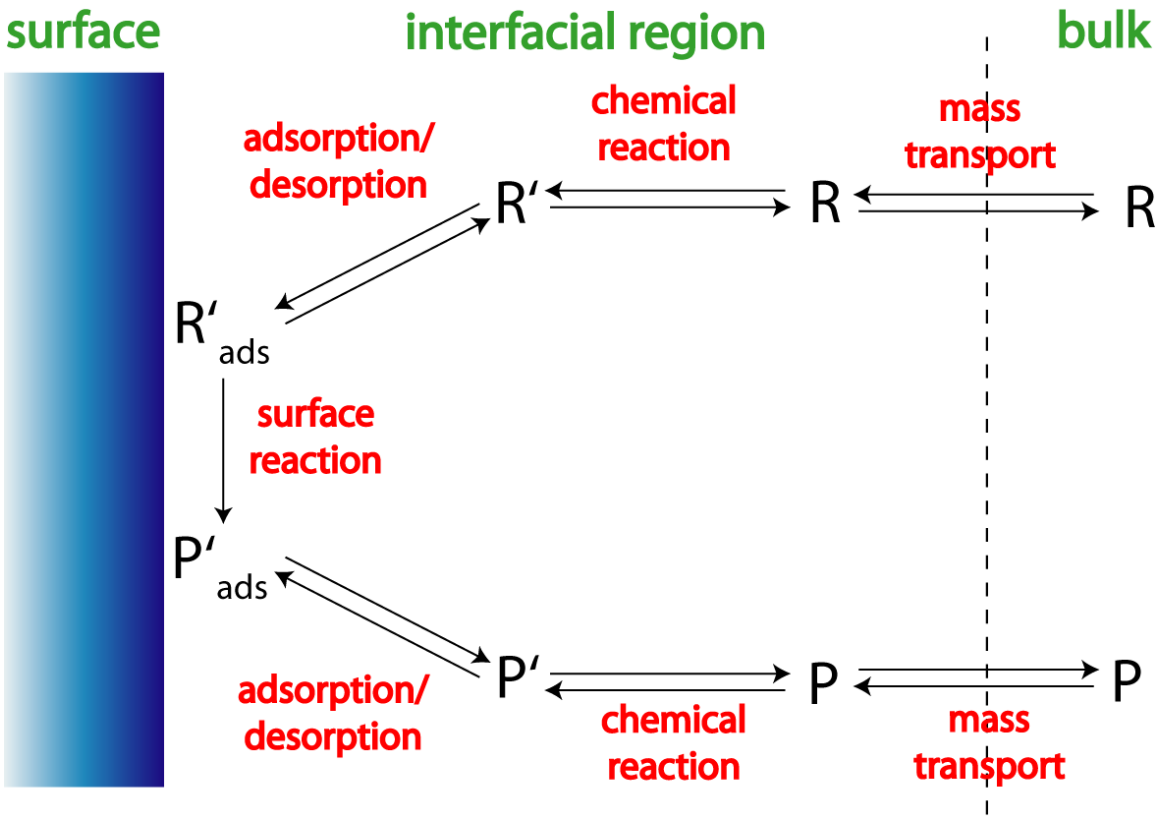

Figure 1.9 Schematic showing the processes that occur during a surface reaction. The chemical reaction refers to some reaction occuring in the interfacial region, for example it could represent the protonation/deprotonation of molecules in the interfacial region due to the pH in the vicinity of the surface differing from that in bulk.

Migration is the movement of ions in an electric field. The effects of migration are much more difficult to quantify than diffusion and convection, so where appropriate it is necessary to reduce these effects as much as possible. An example is during electrochemical experiments, since the change in potential at the electrode will cause ions in solution to move towards/away from it (or to be repelled from the charged interface). This results in the flow of current which will be recorded along with the electrochemical signal of the species of interest. To reduce the effects of migration of reactive species, an excess of inert supporting electrolyte is added to the solution.[39]

All of the above concepts need to be considered when formulating mathematical models of the underlying physics to determine rate constants, such as those described in Chapters 4, 5 and 6.

1.5 Aims of this Thesis

The following chapters describe the first steps towards the application of EW-CRDS combined with electrochemical and microfluidic methods to the study of biologically-relevant surface processes. The aim is to demonstrate the ability to use the CRDS technique, largely considered a gas-phase method, to understand dynamic processes occuring at interfaces in biology. It is hoped that, although the experiments described herein are simple in nature, the reader will gain an appreciation of the potential insight that EW-CRDS coupled with electrochemical and fluidic methods could provide to the life sciences.

1.6 References

1. (a) Gennis, R. B., *Biomembranes : molecular structure and function*. Springer-Verlag: New York, 1989; (b) Alberts, B., *Molecular biology of the cell*. 4th edition; Garland Science: New York, 2002.

2. Nicu, L.; Leichle, T., Biosensors and tools for surface functionalization from the macro-to the nanoscale: The way forward. *Journal of Applied Physics* **2008,** *104* (11), 111101-111101-16.

3. (a) Fan, X. D.; White, I. M.; Shopoua, S. I.; Zhu, H. Y.; Suter, J. D.; Sun, Y. Z., Sensitive optical biosensors for unlabeled targets: A review. *Analytica Chimica Acta* **2008,** *620* (1-2), 8-26; (b) Cooper, M. A., Label-free screening of bio-molecular interactions. *Anal. Bioanal. Chem.* **2003,** *377* (5), 834-842.

4. Ghindilis, A. L.; Atanasov, P.; Wilkins, M.; Wilkins, E., Immunosensors: electrochemical sensing and other engineering approaches. *Biosensors and Bioelectronics* **1998,** *13* (1), 113-131.

5. Sethi, R. S., Transducer aspects of biosensors. *Biosensors and Bioelectronics* **1994,** *9* (3), 243-264.

6. Barton, S. C.; Gallaway, J.; Atanassov, P., Enzymatic biofuel cells for Implantable and microscale devices. *Chemical Reviews* **2004,** *104* (10), 4867-4886.

7. Cracknell, J. A.; Vincent, K. A.; Armstrong, F. A., Enzymes as working or inspirational electrocatalysts for fuel cells and electrolysis. *Chemical Reviews* **2008,** *108* (7), 2439-2461.

8. Yarbrough, J. M.; Himmel, M. E.; Ding, S. Y., Plant cell wall characterization using scanning probe microscopy techniques. *Biotechnology for Biofuels* **2009,** *2*, 17.

9. (a) Heller, A., Potentially implantable miniature batteries. *Anal. Bioanal. Chem.* **2006,** *385* (3), 469-473; (b) Heller, A., Miniature biofuel cells. *Physical Chemistry Chemical Physics* **2004,** *6* (2), 209-216.

10. Ramanavicius, A.; Ramanaviciene, A., Hemoproteins in Design of Biofuel Cells. *Fuel Cells* **2009,** *9* (1), 25-36.

11. Armstrong, F. A.; Belsey, N. A.; Cracknell, J. A.; Goldet, G.; Parkin, A.; Reisner, E.; Vincent, K. A.; Wait, A. F., Dynamic electrochemical investigations of hydrogen

oxidation and production by enzymes and implications for future technology. *Chemical Society Reviews* **2009,** *38* (1), 36-51.

12. Chen, H.; Yuan, L.; Song, W.; Wu, Z.; Li, D., Biocompatible polymer materials: Role of protein-surface interactions. *Progress in Polymer Science* **2008,** *33* (11), 1059-1087.

13. Sakiyama-Elbert, S.; Hubbell, J., Functional Biomaterials: Design of Novel Biomaterials. *Annual Review of Materials Research* **2001,** *31* (1), 183-201.

14. Schaferling, M.; Nagl, S., Optical technologies for the read out and quality control of DNA and protein microarrays. *Anal. Bioanal. Chem.* **2006,** *385* (3), 500-517.

15. Roy, I.; Mondal, K.; Gupta, M. N., Leveraging protein purification strategies in proteomics. *Journal of Chromatography B* **2007,** *849* (1-2), 32-42.

16. Roque, A. C. A.; Silva, C. S. O.; Taipa, M. Â., Affinity-based methodologies and ligands for antibody purification: Advances and perspectives. *Journal of Chromatography A* **2007,** *1160* (1-2), 44-55.

17. Rabinowitz, J. D.; Vacchino, J. F.; Beeson, C.; McConnell, H. M., Potentiometric measurement of intracellular redox activity. *Journal of the American Chemical Society* **1998,** *120* (10), 2464-2473.

18. Léger, C.; Bertrand, P., Direct Electrochemistry of Redox Enzymes as a Tool for Mechanistic Studies. *Chemical Reviews* **2008,** *108* (7), 2379-2438.

19. Gorton, L.; Lindgren, A.; Larsson, T.; Munteanu, F. D.; Ruzgas, T.; Gazaryan, I., Direct electron transfer between heme-containing enzymes and electrodes as basis for third generation biosensors. *Analytica Chimica Acta* **1999,** *400*, 91-108.

20. (a) Heering, H. A.; Wiertz, F. G. M.; Dekker, C.; de Vries, S., Direct Immobilization of Native Yeast Iso-1 Cytochrome *c* on Bare Gold: Fast Electron Relay to Redox Enzymes and Zeptomole Protein-Film Voltammetry. *Journal of the American Chemical Society* **2004,** *126* (35), 11103-11112; (b) Marken, F.; Paddon, C. A.; Asogan, D., Direct cytochrome *c* electrochemistry at boron-doped diamond electrodes. *Electrochemistry Communications* **2002,** *4* (1), 62-66.

21. Fedurco, M., Redox reactions of heme-containing metalloproteins: dynamic effects of self-assembled monolayers on thermodynamics and kinetics of cytochrome *c* electron-transfer reactions. *Coordination Chemistry Reviews* **2000,** *209*, 263-331.

22. Salamon, Z.; Tollin, G., Reduction of cytochrome *c* at a lipid bilayer modified electrode. *Bioelectrochemistry and Bioenergetics* **1991,** *25* (3), 447-454.

23. Jiang, K.; Zhang, H. X.; Shannon, C.; Zhan, W., Preparation and characterization of polyoxometalate/protein ultrathin films grown on electrode surfaces using layer-by-layer assembly. *Langmuir* **2008,** *24* (7), 3584-3589.

24. (a) Duan, L. S.; Xu, Q.; Xie, F.; Wang, S. F., Hydrogen peroxide biosensor based on the bioelectrocatalysis of myoglobin incorporated in multi-walled carbon nanotubes/chitosan composite film. *International Journal of Electrochemical Science* **2008,** *3* (2), 118-124; (b) Zhang, Y.; Zheng, J. B., Direct electrochemistry and electrocatalysis of cytochrome *c* based on chitosan-room temperature ionic liquid-carbon nanotubes composite. *Electrochimica Acta* **2008,** *54* (2), 749-754.

25. (a) Lin, L.; Qiu, P. H.; Cao, X. N.; Jin, L. T., Colloidal silver nanoparticles modified electrode and its application to the electroanalysis of cytochrome *c*. *Electrochimica Acta* **2008,** *53* (16), 5368-5372; (b) Mu, C.; Zhao, Q.; Xu, D. S.; Zhuang,

Q. K.; Shao, Y. H., Silicon nanotube array/gold electrode for direct electrochemistry of cytochrome *c*. *Journal of Physical Chemistry B* **2007,** *111* (6), 1491-1495.

26. Baymann, F.; Barlow, N. L.; Aubert, C.; Schoepp-Cothenet, B.; Leroy, G.; Armstrong, F. A., Voltammetry of a `protein on a rope'. *FEBS Letters* **2003,** *539* (1-3), 91-94.

27. Armstrong, F. A., Recent developments in dynamic electrochemical studies of adsorbed enzymes and their active sites. *Current Opinion in Chemical Biology* **2005,** *9* (2), 110-117.

28. Jeuken, L. J. C.; Jones, A. K.; Chapman, S. K.; Cecchini, G.; Armstrong, F. A., Electron-Transfer Mechanisms through Biological Redox Chains in Multicenter Enzymes. *Journal of the American Chemical Society* **2002,** *124* (20), 5702-5713.

29. (a) Armstrong, F. A., Insights from protein film voltammetry into mechanisms of complex biological electron-transfer reactions. *Journal of the Chemical Society-Dalton Transactions* **2002,** (5), 661-671; (b) Armstrong, F. A.; Camba, R.; Heering, H. A.; Hirst, J.; Jeuken, L. J. C.; Jones, A. K.; Leger, C.; McEvoy, J. P., Fast voltammetric studies of the kinetics and energetics of coupled electron-transfer reactions in proteins. *Faraday Discussions* **2000,** *116* (116), 191-203.

30. Lee, T. M. H., Over-the-counter biosensors: Past, present, and future. *Sensors* **2008,** *8* (9), 5535-5559.

31. Chen, H.; Jiang, C.; Yu, C.; Zhang, S.; Liu, B.; Kong, J., Protein chips and nanomaterials for application in tumor marker immunoassays. *Biosensors and Bioelectronics* **2009,** *24* (12), 3399-3411.

32. Drummond, T. G.; Hill, M. G.; Barton, J. K., Electrochemical DNA sensors. *Nature Biotechnology* **2003,** *21* (10), 1192-1199.

33. Diculescu, V. C.; Barbosa, R. M.; Brett, A. M. O., In Situ Sensing of DNA Damage by a Nitric Oxide-Releasing Compound. *Analytical Letters* **2005,** *38* (15), 2525.

34. (a) Rivas, G. A.; Pedano, M. L.; Ferreyra, N. F., Electrochemical Biosensors for Sequence-Specific DNA Detection. *Analytical Letters* **2005,** *38* (15), 2653; (b) He, P.; Xu, Y.; Fang, Y., A Review: Electrochemical DNA Biosensors for Sequence Recognition. *Analytical Letters* **2005,** *38* (15), 2597.

35. Giallo, M. L. D.; Ariksoysal, D. O.; Marrazza, G.; Mascini, M.; Ozsoz, M., Disposable Electrochemical Enzyme-Amplified Genosensor for *Salmonella* Bacteria Detection. *Analytical Letters* **2005,** *38* (15), 2509.

36. (a) Ianniello, R. M.; Lindsay, T. J.; Yacynych, A. M., Immobilized xanthine oxidase chemically modified electrode as a dual analytical sensor. *Analytical Chemistry* **2002,** *54* (12), 1980-1984; (b) Ghindilis, A. L.; Kurochkin, I. N., Glucose potentiometric electrodes based on mediatorless bioelectrocatalysis. A new approach. *Biosensors and Bioelectronics* **1994,** *9* (4-5), 353-357.

37. Katz, E.; Heleg-Shabtai, V.; Willner, B.; Willner, I.; Bückmann, A. F., Electrical contact of redox enzymes with electrodes: novel approaches for amperometric biosensors. *Bioelectrochemistry and Bioenergetics* **1997,** *42* (1), 95-104.

38. (a) Thévenot, D. R.; Toth, K.; Durst, R. A.; Wilson, G. S., Electrochemical biosensors: recommended definitions and classification. *Biosensors and Bioelectronics* **2001,** *16* (1-2), 121-131; (b) Bakker, E., Electrochemical Sensors. *Analytical Chemistry* **2004,** *76* (12), 3285-3298; (c) Lisdat, F.; Schafer, D., The use of electrochemical

impedance spectroscopy for biosensing. *Anal. Bioanal. Chem.* **2008,** *391* (5), 1555-1567; (d) Katz, E.; Willner, I., Probing Biomolecular Interactions at Conductive and Semiconductive Surfaces by Impedance Spectroscopy: Routes to Impedimetric Immunosensors, DNA-Sensors, and Enzyme Biosensors. *Electroanalysis* **2003,** *15* (11), 913-947; (e) Guan, J.-G.; Miao, Y.-Q.; Zhang, Q.-J., Impedimetric biosensors. *Journal of Bioscience and Bioengineering* **2004,** *97* (4), 219-226; (f) Daniels, Jonathan S.; Pourmand, N., Label-Free Impedance Biosensors: Opportunities and Challenges. *Electroanalysis* **2007,** *19* (12), 1239-1257.

39. Bard, A. J.; Faulkner, L. R., *Electrochemical Methods: Fundamentals and Applications*. 2nd ed.; John Wiley & Sons Inc.: 2001.

40. (a) Amemiya, S.; Bard, A. J.; Fan, F. R. F.; Mirkin, M. V.; Unwin, P. R., Scanning Electrochemical Microscopy. *Annual Review of Analytical Chemistry* **2008,** *1*, 95-131; (b) Edwards, M. A.; Martin, S.; Whitworth, A. L.; Macpherson, J. V.; Unwin, P. R., Scanning electrochemical microscopy: principles and applications to biophysical systems. *Physiological Measurement* **2006,** *27* (12), R63-R108.

41. Zhao, C.; Wittstock, G., Scanning Electrochemical Microscopy of Quinoprotein Glucose Dehydrogenase. *Analytical Chemistry* **2004,** *76* (11), 3145-3154.

42. Wittstock, G.; Burchardt, M.; Pust, S. E.; Shen, Y.; Zhao, C., Scanning electrochemical microscopy for direct imaging of reaction rates. *Angewandte Chemie-International Edition* **2007,** *46* (10), 1584-1617.

43. (a) Roberts, W. S.; Lonsdale, D. J.; Griffiths, J.; Higson, S. P. J., Advances in the application of scanning electrochemical microscopy to bioanalytical systems. *Biosensors and Bioelectronics* **2007,** *23* (3), 301-318; (b) Gyurcsanyi, R. E.; Jagerszki, G.; Kiss, G.;

Toth, K. In *Chemical imaging of biological systems with the scanning electrochemical microscope*, 17th Symposium on Bioelectrochemistry and Bioenergetics, Florence, Italy, Jun 19-24; Florence, Italy, 2003; pp 207-215; (c) Amemiya, S.; Guo, J. D.; Xiong, H.; Gross, D. A., Biological applications of scanning electrochemical microscopy: chemical imaging of single living cells and beyond. *Analytical and Bioanalytical Chemistry* **2006,** *386* (3), 458-471; (d) Sun, P.; Laforge, F. O.; Mirkin, M. V., Scanning electrochemical microscopy in the 21st century. *Physical Chemistry Chemical Physics* **2007,** *9* (7), 802-823; (e) Wittstock, G., Modification and characterization of artificially patterned enzymatically active surfaces by scanning electrochemical microscopy. *Fresenius Journal of Analytical Chemistry* **2001,** *370* (4), 303-315.

44. Lee, C. M.; Kwak, J. Y.; Bard, A. J., Application of Scanning Electrocehmical Micrscopy to Biological Samples. *Proceedings of the National Academy of Sciences of the United States of America* **1990,** *87* (5), 1740-1743.

45. Yasukawa, T.; Kondo, Y.; Uchida, I.; Matsue, T., Imaging of cellular activity of single cultured cells by scanning electrochemical microscopy. *Chemistry Letters* **1998,** (8), 767-768.

46. (a) Amatore, C.; Bouret, Y.; Midrier, L., Time-Resolved Dynamics of the Vesicle Membrane During Individual Exocytotic Secretion Events, as Extracted from Amperometric Monitoring of Adrenaline Exocytosis from Chromaffin Cells. *Chemistry - A European Journal* **1999,** *5* (7), 2151-2162; (b) Amatore, C.; Bouret, Y.; Travis, E. R.; Wightman, R. M., Adrenaline Release by Chromaffin Cells: Constrained Swelling of the Vesicle Matrix Leads to Full Fusion13. *Angewandte Chemie International Edition* **2000,** *39* (11), 1952-1955.

47. Holt, K. B., Using scanning electrochemical microscopy (SECM) to measure the electron-transfer kinetics of cytochrome *c* immobilized on a COOH-terminated alkanethiol monolayer on a gold electrode. *Langmuir* **2006,** *22* (9), 4298-4304.

48. (a) Pierce, D. T.; Unwin, P. R.; Bard, A. J., Scanning Electrochemical Microscopy .17. Studies of enzyme mediator kinetics for membrane-immobilized and surface-immobilized glucose-oxidase. *Analytical Chemistry* **1992,** *64* (17), 1795-1804; (b) Pierce, D. T.; Bard, A. J., Scanning Electrochemical Microscopy .23. Reaction localization of artificially patterned and tissue-bound enzymes. *Analytical Chemistry* **1993,** *65* (24), 3598-3604.

49. Zhou, J. F.; Campbell, C.; Heller, A.; Bard, A. J., Scanning electrochemical microscopy. 44. Imaging of horseradish peroxidase immobilized on insulating substrates. *Analytical Chemistry* **2002,** *74* (16), 4007-4010.

50. (a) Kranz, C.; Kueng, A.; Lugstein, A.; Bertagnolli, E.; Mizaikoff, B., Mapping of enzyme activity by detection of enzymatic products during AFM imaging with integrated SECM-AFM probes. *Ultramicroscopy* **2004,** *100* (3-4), 127-134; (b) Wilhelm, T.; Wittstock, G., Generation of periodic enzyme patterns by soft lithography and activity imaging by scanning electrochemical microscopy. *Langmuir* **2002,** *18* (24), 9485-9493; (c) Turcu, F.; Hartwich, G.; Schafer, D.; Schuhmann, W., Ink-jet microdispensing for the formation of gradients of immobilised enzyme activity. *Macromolecular Rapid Communications* **2005,** *26* (4), 325-330; (d) Lin, S.; Liu, C. C.; Chou, T. C., Amperometric acetylcholine sensor catalyzed by nickel anode electrode. *Biosensors & Bioelectronics* **2004,** *20* (1), 9-14.

51. Zhang, X. L.; Peng, X. W.; Jin, W. R., Scanning electrochemical microscopy with enzyme immunoassay of the cancer-related antigen CA15-3. *Analytica Chimica Acta* **2006,** *558* (1-2), 110-114.

52. Hansma, P. K.; Drake, B.; Marti, O.; Gould, S. A. C.; Prater, C. B., The Scanning Ion-Conductance Microscope. *Science* **1989,** *243* (4891), 641-643.

53. Ying, L. M.; Bruckbauer, A.; Zhou, D. J.; Gorelik, J.; Shevehuk, A.; Lab, M.; Korchev, Y.; Klenerman, D., The scanned nanopipette: A new tool for high resolution bioimaging and controlled deposition of biomolecules. *Physical Chemistry Chemical Physics* **2005,** *7* (15), 2859-2866.

54. Shevchuk, A. I.; Hobson, P.; Lab, M. J.; Klenerman, D.; Krauzewicz, N.; Korchev, Y. E., Endocytic pathways: combined scanning ion conductance and surface confocal microscopy study. *Pflugers Archiv-European Journal of Physiology* **2008,** *456* (1), 227-235.

55. Shevchuk, A. I.; Gorelik, J.; Harding, S. E.; Lab, M. J.; Klenerman, D.; Korchev, Y. E., Simultaneous measurement of Ca2+ and cellular dynamics: Combined scanning ion conductance and optical microscopy to study contracting cardiac myocytes. *Biophysical Journal* **2001,** *81* (3), 1759-1764.

56. Bruckbauer, A.; James, P.; Zhou, D. J.; Yoon, J. W.; Excell, D.; Korchev, Y.; Jones, R.; Klenerman, D., Nanopipette delivery of individual molecules to cellular compartments for single-molecule fluorescence tracking. *Biophysical Journal* **2007,** *93*, 3120-3131.

57. (a) Bruckbauer, A.; Zhou, D. J.; Ying, L. M.; Korchev, Y. E.; Abell, C.; Klenerman, D., Multicomponent submicron features of biomolecules created by voltage

controlled deposition from a nanopipet. *Journal of the American Chemical Society* **2003,** *125* (32), 9834-9839; (b) Bruckbauer, A.; Zhou, D. J.; Kang, D. J.; Korchev, Y. E.; Abell, C.; Klenerman, D., An addressable antibody nanoarray produced on a nanostructured surface. *Journal of the American Chemical Society* **2004,** *126* (21), 6508-6509.

58. Rothery, A. M.; Gorelik, J.; Bruckbauer, A.; Yu, W.; Korchev, Y. E.; Klenerman, D., A novel light source for SICM-SNOM of living cells. *Journal of Microscopy-Oxford* **2003,** *209*, 94-101.

59. Sanchez, D.; Johnson, N.; Li, C.; Novak, P.; Rheinlaender, J.; Zhang, Y. J.; Anand, U.; Anand, P.; Gorelik, J.; Frolenkov, G. I.; Benham, C.; Lab, M.; Ostanin, V. P.; Schaffer, T. E.; Klenerman, D.; Korchev, Y. E., Noncontact measurement of the local mechanical properties of living cells using pressure applied via a pipette. *Biophysical Journal* **2008,** *95* (6), 3017-3027.

60. Cavic, B. A.; Hayward, G. L.; Thompson, M., Acoustic waves and the study of biochemical macromolecules and cells at the sensor-liquid interface. *Analyst* **1999,** *124* (10), 1405-1420.

61. Sauerbrey, G., The use of quartz oscillators for weighing thin layers and for microweighing. *Z. Phys.* **1959,** *155*, 206-22.

62. (a) Bandey, H. L.; Hillman, A. R.; Brown, M. J.; Martin, S. J., Viscoelastic characterization of electroactive polymer films at the electrode/solution interface. *Faraday Discussions* **1997,** *107*, 105-121; (b) Ramirez, S.; Hillman, A. R., Electrochemical Quartz Crystal Microbalance Studies of Poly(ortho-toluidine) Films Exposed to Aqueous Perchloric Acid Solutions. *Journal of the Electrochemical Society* **1998,** *145* (8), 2640-6247; (c) Martin, S. J.; Bandey, H. L.; Cernosek, R. W.; Hillman, A.

R.; Brown, M. J., Equivalent-circuit model for the thickness-shear mode resonator with a viscoelastic film near film resonance. *Analytical Chemistry* **2000,** *72* (1), 141-149.

63. Marx, K. A., Quartz crystal microbalance: A useful tool for studying thin polymer films and complex biomolecular systems at the solution-surface interface. *Biomacromolecules* **2003,** *4* (5), 1099-1120.

64. (a) Yang, M. S.; Chung, F. L.; Thompson, M., Acoustic Network Analysis as a Novel Technique for Studying Protein Adsorption and Denaturation at Surfaces. *Analytical Chemistry* **1993,** *65* (24), 3713-3716; (b) Rodahl, M.; Hook, F.; Fredriksson, C.; Keller, C. A.; Krozer, A.; Brzezinski, P.; Voinova, M.; Kasemo, B., Simultaneous frequency and dissipation factor QCM measurements of biomolecular adsorption and cell adhesion. *Faraday Discussions* **1997,** *107*, 229-246.

65. (a) Lvov, Y.; Ariga, K.; Ichinose, I.; Kunitake, T., Assembly of multicomponent protein films by means of electrostatic layer-by-layer adsorption. *Journal of the American Chemical Society* **1995,** *117* (22), 6117-6123; (b) Cavic, B. A.; Thompson, M., Protein adsorption to organosiloxane surfaces studied by acoustic wave sensor. *Analyst* **1998,** *123* (10), 2191-2196.

66. (a) Ebara, Y.; Okahata, Y., Insitu surface-detecting technique by using a quartz-crystal microbalance - interaction behaviors of proteins onto a phospholipid monolayer at the air-water-interface. *Langmuir* **1993,** *9* (2), 574-576; (b) Janshoff, A.; Steinem, C.; Sieber, M.; Galla, H. J., Specific binding of peanut agglutinin to G(M1)-doped solid supported lipid bilayers investigated by shear wave resonator measurements. *European Biophysics Journal with Biophysics Letters* **1996,** *25* (2), 105-113; (c) Janshoff, A.; Steinem, C.; Sieber, M.; elBaya, A.; Schmidt, M. A.; Galla, H. J., Quartz crystal

microbalance investigation of the interaction of bacterial toxins with ganglioside containing solid supported membranes. *European Biophysics Journal with Biophysics Letters* **1997,** *26* (3), 261-270.

67. Sakai, G.; Saiki, T.; Uda, T.; Miura, N.; Yamazoe, N., Evaluation of binding of human serum albumin (HSA) to monoclonal and polyclonal antibody by means of piezoelectric immunosensing technique. *Sensors and Actuators B-Chemical* **1997,** *42* (2), 89-94.

68. Muratsugu, M.; Ohta, F.; Miya, Y.; Hosokawa, T.; Kurosawa, S.; Kamo, N.; Ikeda, H., Quartz-crystal microbalance for the detection of microgram quantities of human serum-albumin - relationship between the frequency change and the mass of protein adsorbed. *Analytical Chemistry* **1993,** *65* (20), 2933-2937.

69. Caruso, F.; Niikura, K.; Furlong, D. N.; Okahata, Y., Assembly of alternating polyelectrolyte and protein multilayer films for immunosensing .2. *Langmuir* **1997,** *13* (13), 3427-3433.

70. Abad, J. M.; Pariente, F.; Hernandez, L.; Lorenzo, E., A quartz crystal microbalance assay for detection of antibodies against the recombinant African swine fever virus attachment protein p12 in swine serum. *Analytica Chimica Acta* **1998,** *368* (3), 183-189.

71. Rickert, J.; Weiss, T.; Kraas, W.; Jung, G.; Gopel, W., A new affinity biosensor: Self-assembled thiols as selective monolayer coatings of quartz crystal microbalances. *Biosensors & Bioelectronics* **1996,** *11* (6-7), 591-598.

72. BenDov, I.; Willner, I.; Zisman, E., Piezoelectric immunosensors for urine specimens of *Chlamydia trachomatis* employing quartz crystal microbalance microgravimetric analyses. *Analytical Chemistry* **1997,** *69* (17), 3506-3512.

73. Si, S. H.; Ren, F. L.; Cheng, W.; Yao, S. Z., Preparation of a piezoelectric immunosensor for the detection of *Salmonella paratyphi* A by immobilization of antibodies on electropolymerized films. *Fresenius Journal of Analytical Chemistry* **1997,** *357* (8), 1101-1105.

74. (a) Ebersole, R. C.; Miller, J. A.; Moran, J. R.; Ward, M. D., Spontaneously formed functionally active avidin monolayers on metal-surfaces - a strategy for immobilizing biological reagents and design of piezoelectric biosensors. *Journal of the American Chemical Society* **1990,** *112* (8), 3239-3241; (b) Caruso, F.; Rodda, E.; Furlong, D. F.; Niikura, K.; Okahata, Y., Quartz crystal microbalance study of DNA immobilization and hybridization for nucleic acid sensor development. *Analytical Chemistry* **1997,** *69* (11), 2043-2049; (c) Okahata, Y.; Kawase, M.; Niikura, K.; Ohtake, F.; Furusawa, H.; Ebara, Y., Kinetic measurements of DNA hybridisation an an oligonucleotide-immobilized 27-MHz quartz crystal microbalance. *Analytical Chemistry* **1998,** *70* (7), 1288-1296.

75. (a) Furtado, L. M.; Thompson, M., Hybridization of complementary strand and single base mutated oligonucleotides detected with an on-line acoustic wave sensor. *Analyst* **1998,** *123* (10), 1937-1945; (b) Wang, J.; Nielsen, P. E.; Jiang, M.; Cai, X. H.; Fernandes, J. R.; Grant, D. H.; Ozsoz, M.; Beglieter, A.; Mowat, M., Mismatch sensitive hybridization detection by peptide nucleic acids immobilized on a quartz crystal microbalance. *Analytical Chemistry* **1997,** *69* (24), 5200-5202.

76. Furtado, L. M.; Su, H. B.; Thompson, M.; Mack, D. P.; Hayward, G. L., Interactions of HIV-1 TAR RNA with Tat-derived peptides discriminated by on-line acoustic wave detector. *Analytical Chemistry* **1999,** *71* (6), 1167-1175.

77. Su, H. B.; Williams, P.; Thompson, M., Platinum anticancer drug-binding to dna detected by thickness-shear-mode acoustic-wave sensor. *Analytical Chemistry* **1995,** *67* (5), 1010-1013.

78. Aslanoglu, M.; Houlton, A.; Horrocks, B. R., Functionalised monolayer for nucleic acid immobilisation on gold surfaces and metal complex binding studies. *Analyst* **1998,** *123* (4), 753-757.

79. Yang, M. S.; Yau, H. C. M.; Chan, H. L., Adsorption kinetics and ligand-binding properties of thiol-modified double-stranded DNA on a gold surface. *Langmuir* **1998,** *14* (21), 6121-6129.

80. Redepenning, J.; Schlesinger, T. K.; Mechalke, E. J.; Puleo, D. A.; Bizios, R., Osteoblast attachment monitored with a quartz-crystal microbalance. *Analytical Chemistry* **1993,** *65* (23), 3378-3381.

81. (a) Gryte, D. M.; Ward, M. D.; Hu, W. S., Real-time measurement of anchorage-dependent cell-adhesion using a quartz crystal microbalance. *Biotechnology Progress* **1993,** *9* (1), 105-108; (b) Fredriksson, C.; Kihlman, S.; Rodahl, M.; Kasemo, B., The piezoelectric quartz crystal mass and dissipation sensor: A means of studying cell adhesion. *Langmuir* **1998,** *14* (2), 248-251.

82. Muratsugu, M.; Romaschin, A. D.; Thompson, M., Adhesion of human platelets to collagen detected by Cr-51 labelling and acoustic wave sensor. *Analytica Chimica Acta* **1997,** *342* (1), 23-29.

83. Petty, H. R., Fluorescence microscopy: Established and emerging methods, experimental strategies, and applications in immunology. *Microscopy Research and Technique* **2007,** *70*, 687-709.

84. Chen, Y.; Lagerholm, B. C.; Yang, B.; Jacobson, K., Methods to measure the lateral diffusion of membrane lipids and proteins. *Methods* **2006,** *39* (2), 147-153.

85. Ciruela, F., Fluorescence-based methods in the study of protein-protein interactions in living cells. *Current Opinion in Biotechnology* **2008,** *19* (4), 338-343.

86. (a) Petrasek, Z.; Eckert, H. J.; Kemnitz, K., Wide-field photon counting fluorescence lifetime imaging microscopy: application to photosynthesizing systems. *Photosynthesis Research* **2009,** *102* (2-3), 157-168; (b) Levitt, J. A.; Matthews, D. R.; Ameer-Beg, S. M.; Suhling, K., Fluorescence lifetime and polarization-resolved imaging in cell biology. *Current Opinion in Biotechnology* **2009,** *20* (1), 28-36.

87. Simpson, G. J., Biological imaging - The diffraction barrier broken. *Nature* **2006,** *440* (7086), 879-880.

88. (a) White, N. S.; Errington, R. J., Fluorescence techniques for drug delivery research: theory and practice. *Advanced Drug Delivery Reviews* **2005,** *57* (1), 17-42; (b) Kim, H. D.; Nienhaus, G. U.; Ha, T.; Orr, J. W.; Williamson, J. R.; Chu, S., Mg2+-dependent conformational change of RNA studied by fluorescence correlation and FRET on immobilized single molecules. *Proceedings of the National Academy of Sciences of the United States of America* **2002,** *99* (7), 4284-4289; (c) Jaiswal, J. K.; Simon, S. M., Imaging single events at the cell membrane. *Nature Chemical Biology* **2007,** *3* (2), 92-98; (d) Halbhuber, K. J.; Konig, K., Modern laser scanning microscopy in biology,

biotechnology and medicine. *Annals of Anatomy-Anatomischer Anzeiger* **2003,** *185* (1), 1-20.

89. Wilson, T., Trends in confocal microscopy. *Trends in Neurosciences* **1989,** *12* (12), 486-493.

90. White, J. G.; Amos, W. B.; Fordham, M., An evaluation of confocal versus conventional imaging of biological structures by fluorescence light-microscopy. *Journal of Cell Biology* **1987,** *105* (1), 41-48.

91. Ha, T. J.; Ting, A. Y.; Liang, J.; Caldwell, W. B.; Deniz, A. A.; Chemla, D. S.; Schultz, P. G.; Weiss, S., Single-molecule fluorescence spectroscopy of enzyme conformational dynamics and cleavage mechanism. *Proceedings of the National Academy of Sciences of the United States of America* **1999,** *96* (3), 893-898.

92. Zhuang, X. W.; Bartley, L. E.; Babcock, H. P.; Russell, R.; Ha, T. J.; Herschlag, D.; Chu, S., A single-molecule study of RNA catalysis and folding. *Science* **2000,** *288* (5473), 2048-+.

93. Pygall, S. R.; Whetstone, J.; Timmins, P.; Melia, C. D., Pharmaceutical applications of confocal laser scanning microscopy: The physical characterisation of pharmaceutical systems. *Advanced Drug Delivery Reviews* **2007,** *59* (14), 1434-1452.

94. Tokgoz, N. S.; Grossiord, J. L.; Fructus, A.; Seiller, M.; Prognon, P., Evaluation of two fluorescent probes for the characterization of W/O/W emulsions. *International Journal of Pharmaceutics* **1996,** *141* (1-2), 27-37.

95. Cutts, L. S.; Hibberd, S.; Adler, J.; Davies, M. C.; Melia, C. D., Characterising drug release processes within controlled release dosage forms using the confocal laser scanning microscope. *Journal of Controlled Release* **1996,** *42* (2), 115-124.

96. (a) Berkland, C.; Kipper, M. J.; Narasimhan, B.; Kim, K. K.; Pack, D. W., Microsphere size, precipitation kinetics and drug distribution control drug release from biodegradable polyanhydride microspheres. *Journal of Controlled Release* **2004,** *94* (1), 129-141; (b) Wang, J.; Wang, B. A.; Schwendeman, S. P., Characterization of the initial burst release of a model peptide from poly(D,L-lactide-co-glycolide) microspheres. *Journal of Controlled Release* **2002,** *82* (2-3), 289-307.

97. Heertje, I.; Van Aalst, H.; Blonk, J. C. G.; Don, A.; Nederlof, J.; Lucassen-Reynders, E. H., Observations on emulsifiers at the interface between oil and water by confocal scanning light microscopy. *Lebensmittel-Wissenschaft and Technologie* **1996,** *29* (3), 217-226.

98. Lacasse, F. X.; Filion, M. C.; Phillips, N. C.; Escher, E.; McMullen, J. N.; Hildgen, P., Influence of surface properties at biodegradable microsphere surfaces: Effects on plasma protein adsorption and phagocytosis. *Pharmaceutical Research* **1998,** *15* (2), 312-317.

99. (a) Ljunglof, A.; Thommes, J., Visualising intraparticle protein transport in porous adsorbents by confocal microscopy. *Journal of Chromatography A* **1998,** *813* (2), 387-395; (b) Ljunglof, A.; Hjorth, R., Confocal microscopy as a tool for studying protein adsorption to chromatographic matrices. *Journal of Chromatography A* **1996,** *743* (1), 75-83; (c) Hubbuch, J.; Kula, M. R., Confocal laser scanning microscopy as an analytical tool in chromatographic research. *Bioprocess and Biosystems Engineering* **2008,** *31* (3), 241-259.

100. Rojanasakul, Y.; Liaw, J.; Robinson, J. R., Mechanisms of action of some penetration enhancers in the cornea: Laser scanning confocal microscopic and

electrophysiology studies. *International Journal of Pharmaceutics* **1990,** *66* (1-3), 131-142.

101. Dunn, R. C., Near-field scanning optical microscopy. *Chemical Reviews* **1999,** *99* (10), 2891-+.

102. de Lange, F.; Cambi, A.; Huijbens, R.; de Bakker, B.; Rensen, W.; Garcia-Parajo, M.; van Hulst, N.; Figdor, C. G., Cell biology beyond the diffraction limit: near-field scanning optical microscopy. *Journal of Cell Science* **2001,** *114* (23), 4153-4160.

103. Hecht, B.; Sick, B.; Wild, U. P.; Deckert, V.; Zenobi, R.; Martin, O. J. F.; Pohl, D. W., Scanning near-field optical microscopy with aperture probes: Fundamentals and applications. *Journal of Chemical Physics* **2000,** *112* (18), 7761-7774.

104. Paesler, M. A.; Moyer, P. J.; Jahncke, C. J.; Johnson, C. E.; Reddick, R. C.; Warmack, R. J.; Ferrell, T. L., Analytical photon scanning tunneling microscopy. *Physical Review B* **1990,** *42*, 6750.

105. van Hulst, N. F.; Moers, M. H. P., Biological applications of near-field optical microscopy. *Engineering in Medicine and Biology Magazine, IEEE* **1996,** *15* (1), 51-58.

106. Kirsch, A. K.; Subramaniam, V.; Striker, G.; Schnetter, C.; Arndt-Jovin, D. J.; Jovin, T. M., Continuous wave two-photon scanning near-field optical microscopy. *Biophysical Journal* **1998,** *75* (3), 1513-1521.

107. Jenei, A.; Kirsch, A. K.; Subramaniam, V.; Arndt-Jovin, D. J.; Jovin, T. M., Picosecond multiphoton scanning near-field optical microscopy. *Biophysical Journal* **1999,** *76* (2), 1092-1100.

108. Talley, C. E.; Cooksey, G. A.; Dunn, R. C., High resolution fluorescence imaging with cantilevered near-field fiber optic probes. *Applied Physics Letters* **1996,** *69* (25), 3809-3811.

109. Ben-Ami, N.; Radko, A.; Ben-Ami, U.; Lieberman, K.; Rothman, Z.; Rabin, Z.; Lewis, A., Near-field optical imaging of unstained bacteria: Comparison with normal atomic force and far-field optical microscopy in air and aqueous media. *Ultramicroscopy* **1998,** *71* (1-4), 321-325.

110. Keller, T. H.; Rayment, T.; Klenerman, D., Optical chemical imaging of tobacco mosaic virus in solution at 60-nm resolution. *Biophysical Journal* **1998,** *74* (4), 2076-2079.

111. (a) Duggan, J.; Jamal, G.; Tilley, M.; Davis, B.; McKenzie, G.; Vere, K.; Somekh, M. G.; O'Shea, P.; Harris, H., Functional imaging of microdomains in cell membranes. *European Biophysics Journal with Biophysics Letters* **2008,** *37* (8), 1279-1289; (b) Hwang, J.; Gheber, L. A.; Margolis, L.; Edidin, M., Domains in cell plasma membranes investigated by near-field scanning optical microscopy. *Biophysical Journal* **1998,** *74* (5), 2184-2190.

112. Dunn, R. C.; Allen, E. V.; Joyce, S. A.; Anderson, G. A.; Xie, X. S., Near-field fluorescent imaging of single proteins. *Ultramicroscopy* **1995,** *57* (2-3), 113-117.

113. Generosi, J.; Margaritondo, G.; Kropf, M.; Hirling, H.; Catsicas, S.; Johnsson, K.; Tolk, N. H.; Piston, D. W.; Cricenti, A., Photobleaching-free infrared near-field microscopy localizes molecules in neurons. *Journal of Applied Physics* **2008,** *104* (10).

114. (a) Iwabuchi, S.; Muramatsu, H.; Chiba, N.; Kinjo, Y.; Murakami, Y.; Sakaguchi, T.; Yokoyama, K.; Tamiya, E., Simultaneous detection of near-field topographic and

fluorescence images of human chromosomes via scanning near-field optical/atomic-force microscopy (SNOAM). *Nucleic Acids Research* **1997,** *25* (8), 1662-1663; (b) van Hulst, N.; Garcia-Parajo, M.; Moers, M.; Veerman, J.; Ruiter, A., Near-field fluorescence imaging of genetic material: toward the molecular limit. *J Struct Biol* **1997,** *119* (2), 222-31; (c) Wiegrabe, W.; Monajembashi, S.; Dittmar, H.; Greulich, K. O.; Hafner, S.; Hildebrandt, M.; Kittler, M.; Lochner, B.; Unger, E., Scanning near-field optical microscope: A method for investigating chromosomes. *Surface and Interface Analysis* **1997,** *25* (7-8), 510-&.

115. (a) Kirsch, A. K.; Meyer, C. K.; Jovin, T. M., Shear force imaging of DNA in a near-field scanning optical microscope (NSOM). *Journal of Microscopy-Oxford* **1997,** *185*, 396-401; (b) Garcia-Parajo, M. F.; Veerman, J. A.; Ruiter, A. G. T.; van Hulst, N. F., Near-field optical and shear-force microscopy of single fluorophores and DNA molecules. *Ultramicroscopy* **1998,** *71* (1-4), 311-319.

116. Dunn, R. C.; Holtom, G. R.; Mets, L.; Xie, X. S., Near-field fluorescence imaging and fluorescence lifetime measurement of light-harvesting complexes in intact photosynthetic membranes. *Journal of Physical Chemistry* **1994,** *98* (12), 3094-3098.

117. Nagy, P.; Matyus, L.; Jenei, A.; Panyi, G.; Varga, S.; Matko, J.; Szollosi, J.; Gaspar, R.; Jovin, T. M.; Damjanovich, S., Cell fusion experiments reveal distinctly different association characteristics of cell-surface receptors. *Journal of Cell Science* **2001,** *114* (22), 4063-4071.

118. Brown, F. L. H.; Leitner, D. M.; McCammon, J. A.; Wilson, K. R., Lateral diffusion of membrane proteins in the presence of static and dynamic corrals: Suggestions for appropriate observables. *Biophysical Journal* **2000,** *78* (5), 2257-2269.

119. Herrmann, M.; Neuberth, N.; Wissler, J.; Perez, J.; Gradl, D.; Naber, A., Near-Field Optical Study of Protein Transport Kinetics at a Single Nuclear Pore. *Nano Letters* **2009,** *9* (9), 3330-3336.

120. Voue, M.; Goormaghtigh, E.; Homble, F.; Marchand-Brynaert, J.; Conti, J.; Devouge, S.; De Coninck, J., Biochemical interaction analysis on ATR devices: A wet chemistry approach for surface functionalization. *Langmuir* **2007,** *23* (2), 949-955.

121. Axelrod, D., Total internal reflection fluorescence microscopy in cell biology. *Traffic* **2001,** *2* (11), 764-774.

122. Homola, J.; Yee, S. S.; Gauglitz, G., Surface plasmon resonance sensors: review. *Sensors and Actuators B: Chemical* **1999,** *54* (1-2), 3-15.

123. (a) Jordan, C. E.; Frutos, A. G.; Thiel, A. J.; Corn, R. M., Surface Plasmon Resonance Imaging Measurements of DNA Hybridization Adsorption and Streptavidin/DNA Multilayer Formation at Chemically Modified Gold Surfaces. *Analytical Chemistry* **1997,** *69* (24), 4939-4947; (b) He, L.; Musick, M. D.; Nicewarner, S. R.; Salinas, F. G.; Benkovic, S. J.; Natan, M. J.; Keating, C. D., Colloidal Au-Enhanced Surface Plasmon Resonance for Ultrasensitive Detection of DNA Hybridization. *Journal of the American Chemical Society* **2000,** *122* (38), 9071-9077.

124. (a) Lin, S.; Long, S.; Ramirez, S. M.; Cotter, R. J.; Woods, A. S., Characterization of the "Helix Clamp" Motif of HIV-1 Reverse Transcriptase Using MALDI-TOF MS and Surface Plasmon Resonance. *Analytical Chemistry* **2000,** *72* (11), 2635-2640; (b) Bondeson, K.; Frostellkarlsson, A.; Fagerstam, L.; Magnusson, G., Lactose Repressor-Operator DNA Interactions: Kinetic Analysis by a Surface Plasmon Resonance Biosensor. *Analytical Biochemistry* **1993,** *214* (1), 245-251.

125. (a) Khilko, S. N.; Corr, M.; Boyd, L. F.; Lees, A.; Inman, J. K.; Margulies, D. H., Direct detection of major histocompatibility complex class I binding to antigenic peptides using surface plasmon resonance. Peptide immobilization and characterization of binding specificity. *Journal of Biological Chemistry* **1993,** *268* (21), 15425-15434; (b) Löfås, S.; Malmqvist, M.; Rönnberg, I.; Stenberg, E.; Liedberg, B.; Lundström, I., Bioanalysis with surface plasmon resonance. *Sensors and Actuators B: Chemical* **1991,** *5* (1-4), 79-84.

126. Jung, L. S.; Shumaker-Parry, J. S.; Campbell, C. T.; Yee, S. S.; Gelb, M. H., Quantification of Tight Binding to Surface-Immobilized Phospholipid Vesicles Using Surface Plasmon Resonance: Binding Constant of Phospholipase A2. *Journal of the American Chemical Society* **2000,** *122* (17), 4177-4184.

127. (a) Nelson, B. P.; Grimsrud, T. E.; Liles, M. R.; Goodman, R. M.; Corn, R. M., Surface Plasmon Resonance Imaging Measurements of DNA and RNA Hybridization Adsorption onto DNA Microarrays. *Analytical Chemistry* **2000,** *73* (1), 1-7; (b) Brockman, J. M.; Frutos, A. G.; Corn, R. M., A Multistep Chemical Modification Procedure To Create DNA Arrays on Gold Surfaces for the Study of Protein−DNA Interactions with Surface Plasmon Resonance Imaging. *Journal of the American Chemical Society* **1999,** *121* (35), 8044-8051.

128. Frutos, A. G.; Brockman, J. M.; Corn, R. M., Reversible Protection and Reactive Patterning of Amine- and Hydroxyl-Terminated Self-Assembled Monolayers on Gold Surfaces for the Fabrication of Biopolymer Arrays. *Langmuir* **1999,** *16* (5), 2192-2197.

129. (a) Qavi, A. J.; Washburn, A. L.; Byeon, J. Y.; Bailey, R. C., Label-free technologies for quantitative multiparameter biological analysis. *Anal. Bioanal. Chem.*

2009, *394* (1), 121-135; (b) Homola, J., Present and future of surface plasmon resonance biosensors. *Anal. Bioanal. Chem.* **2003,** *377* (3), 528-539.

130. Minunni, M.; Mascini, M., Detection of Pesticide in Drinking Water Using Real-Time Biospecific Interaction Analysis (BIA). *Analytical Letters* **1993,** *26* (7), 1441 - 1460.

131. (a) Mouvet, C.; Harris, R. D.; Maciag, C.; Luff, B. J.; Wilkinson, J. S.; Piehler, J.; Brecht, A.; Gauglitz, G.; Abuknesha, R.; Ismail, G., Determination of simazine in water samples by waveguide surface plasmon resonance. *Analytica Chimica Acta* **1997,** *338* (1-2), 109-117; (b) Harris, R. D.; Luff, B. J.; Wilkinson, J. S.; Piehler, J.; Brecht, A.; Gauglitz, G.; Abuknesha, R. A., Integrated optical surface plasmon resonance immunoprobe for simazine detection. *Biosensors and Bioelectronics* **1999,** *14* (4), 377-386.

132. Miura, N.; Ogata, K.; Sakai, G.; Uda, T.; Yamazoe, N., Detection of Morphine in ppb Range by Using SPR (Surface- Plasmon-Resonance) Immunosensor. *Chemistry Letters* **1997,** *26* (8), 713-714.

133. Sakai, G.; Nakata, S.; Uda, T.; Miura, N.; Yamazoe, N., Highly selective and sensitive SPR immunosensor for detection of methamphetamine. *Electrochimica Acta* **1999,** *44* (21-22), 3849-3854.

134. Mullett, W.; Lai, E. P. C.; Yeung, J. M., Immunoassay of Fumonisins by a Surface Plasmon Resonance Biosensor. *Analytical Biochemistry* **1998,** *258* (2), 161-167.

135. Baxter, G. A.; Ferguson, J. P.; O'Conno, M. C.; Elliott, C. T., Detection of Streptomycin Residues in Whole Milk Using an Optical Immunobiosensor. *Journal of Agricultural and Food Chemistry* **2001,** *49* (7), 3204-3207.

136. Fratamico, P. M.; Strobaugh, T. P.; Medina, M. B.; Gehring, A. G., Detection of Escherichia coli 0157:H7 using a surface plasmon resonance biosensor. *Biotechnology Techniques* **1998,** *12* (7), 571-576.

137. Koubová, V.; Brynda, E.; Karasová, L.; Skvor, J.; Homola, J.; Dostálek, J.; Tobiska, P.; Rosický, J., Detection of foodborne pathogens using surface plasmon resonance biosensors. *Sensors and Actuators B: Chemical* **2001,** *74* (1-3), 100-105.

138. Anderson, D. Z.; Frisch, J. C.; Masser, C. S., Mirror reflectometer based on optical cavity decay time. *Applied Optics* **1984,** *23* (8), 1238-1245.

139. Herbelin, J. M.; McKay, J. A., Development of laser mirrors of very high reflectivity using the cavity-attenuated phase-shift method. *Applied Optics* **1981,** *20* (19), 3341-3344.

140. Herbelin, J. M.; McKay, J. A.; Kwok, M. A.; Ueunten, R. H.; Urevig, D. S.; Spencer, D. J.; Benard, D. J., Sensitive measurement of photon lifetime and true reflectances in an optical cavity by a phase-shift method. *Applied Optics* **1980,** *19* (1), 144-147.

141. Okeefe, A.; Deacon, D. A. G., Cavity ring-down optical spectrometer for absorption-measurements using pulsed laser sources. *Review of Scientific Instruments* **1988,** *59* (12), 2544-2551.

142. Busch, K. W.; Busch, M. A., *Cavity-ringdown spectroscopy : an ultratrace-absorption measurement technique*. American Chemical Society: Washington, DC, 1999.

143. Platt, U.; Perner, D., Direct measurements of atmospheric CH_2O,HNO_2,O_3,NO_2, and SO_2 by differential optical-absorption in the near Uv. *Journal of Geophysical Research-Oceans and Atmospheres* **1980,** *85* (NC12), 7453-7458.

144. (a) Paldus, B. A.; Kachanov, A. A., An historical overview of cavity-enhanced methods. *Canadian Journal of Physics* **2005,** *83* (10), 975-999; (b) Scherer, J. J.; Paul, J. B.; Okeefe, A.; Saykally, R. J., Cavity ringdown laser absorption spectroscopy: History, development, and application to pulsed molecular beams. *Chemical Reviews* **1997,** *97* (1), 25-51.

145. (a) Berden, G.; Peeters, R.; Meijer, G., Cavity ring-down spectroscopy: Experimental schemes and applications. *International Reviews in Physical Chemistry* **2000,** *19* (4), 565-607; (b) Peeters, R.; Berden, G.; Meijer, G., Sensitive absorption techniques for spectroscopy. *American Laboratory* **2001,** *33* (3), 60-+; (c) Wheeler, M. D.; Newman, S. M.; Orr-Ewing, A. J.; Ashfold, M. N. R., Cavity ring-down spectroscopy. *Journal of the Chemical Society-Faraday Transactions* **1998,** *94* (3), 337-351; (d) Vallance, C., Innovations in cavity ringdown spectroscopy. *New Journal of Chemistry* **2005,** *29* (7), 867-874.

146. Kogelnik; Li, Laser beams and resonators. *Applied Optics* **1966**.

147. Ball, S. M.; Jones, R. L., Broad-band cavity ring-down spectroscopy. *Chemical Reviews* **2003,** *103* (12), 5239-5262.

148. (a) Hallock, A. J.; Berman, E. S. F.; Zare, R. N., Direct monitoring of absorption in solution by cavity ring-down spectroscopy. *Analytical Chemistry* **2002,** *74* (7), 1741-1743; (b) Hallock, A. J.; Berman, E. S. F.; Zare, R. N., Direct monitoring of absorption in solution by cavity ring-down spectroscopy (vol 74, pg 1741, 2002). *Analytical Chemistry* **2007,** *79* (6), 2596-2596.

149. Kleine, D.; Lauterbach, J.; Kleinermanns, K.; Hering, P., Cavity ring-down spectroscopy of molecularly thin iodine layers. *Applied Physics B-Lasers and Optics* **2001,** *72* (2), 249-252.

150. (a) Muir, R. N.; Alexander, A. J., Structure of monolayer dye films studied by Brewster angle cavity ringdown spectroscopy. *Physical Chemistry Chemical Physics* **2003,** *5* (6), 1279-1283; (b) Alexander, A. J., Reaction kinetics of nitrate radicals with terpenes in solution studied by cavity ring-down spectroscopy. *Chemical Physics Letters* **2004,** *393* (1-3), 138-142; (c) Snyder, K. L.; Zare, R. N., Cavity ring-down spectroscopy as a detector for liquid chromatography. *Analytical Chemistry* **2003,** *75* (13), 3086-3091; (d) Xu, S. C.; Sha, G. H.; Xie, J. C., Cavity ring-down spectroscopy in the liquid phase. *Review of Scientific Instruments* **2002,** *73* (2), 255-258.

151. Pipino, A. C. R.; Hudgens, J. W.; Huie, R. E., Evanescent wave cavity ring-down spectroscopy for probing surface processes. *Chem. Phys. Lett.* **1997,** *280* (1-2), 104-112.

152. Pipino, A. C. R.; Hudgens, J. W.; Huie, R. E., Evanescent wave cavity ring-down spectroscopy with a total-internal-reflection minicavity. *Review of Scientific Instruments* **1997,** *68* (8), 2978-2989.

153. (a) Pipino, A. C. R., Ultrasensitive surface spectroscopy with a miniature optical resonator. *Physical Review Letters* **1999,** *83* (15), 3093-3096; (b) Pipino, A. C. R., Monolithic folded resonator for evanescent wave cavity ringdown spectroscopy. *Applied Optics* **2000,** *39* (9), 1449-1453.

154. Aarts, I. M. P.; Pipino, A. C. R.; de Sanden, M.; Kessels, W. M. M., Absolute in situ measurement of surface dangling bonds during a-Si : H growth. *Applied Physics Letters* **2007,** *90* (16).

155. Aarts, I. M. P.; Pipino, A. C. R.; Hoefnagels, J. P. M.; Kessels, W. M. M.; van de Sanden, M. C. M., Quasi-ice monolayer on atomically smooth amorphous SiO_2 at room temperature observed with a high-finesse optical resonator. *Physical Review Letters* **2005,** *95* (16).

156. Pipino, A. C. R.; Hoefnagels, J. P. M.; Watanabe, N., Absolute surface coverage measurement using a vibrational overtone. *Journal of Chemical Physics* **2004,** *120* (6), 2879-2888.

157. Pipino, A. C. R.; Michalski, M., Climbing the vibrational ladder to probe the OH stretch of HNO_3 on silica. *Journal of Physical Chemistry C* **2007,** *111* (26), 9442-9447.

158. (a) Shaw, A. M.; Hannon, T. E.; Li, F. P.; Zare, R. N., Adsorption of crystal violet to the silica-water interface monitored by evanescent wave cavity ring-down spectroscopy. *Journal of Physical Chemistry B* **2003,** *107* (29), 7070-7075; (b) Fisk, J. D.; Batten, R.; Jones, G.; O'Reilly, J. P.; Shaw, A. M., pH dependence of the crystal violet adsorption isotherm at the silica-water interface. *Journal of Physical Chemistry B* **2005,** *109* (30), 14475-14480.

159. Fan, H. F.; Li, F.; Zare, R. N.; Lin, K. C., Characterization of Two Types of Silanol Groups on Fused-Silica Surfaces Using Evanescent-Wave Cavity Ring-Down Spectroscopy. *Anal. Chem.* **2007,** *79* (10), 3654-3661.

160. O'Reilly, J. P.; Butts, C. P.; I'Anson, I. A.; Shaw, A. M., Interfacial pH at an isolated silica-water surface. *Journal of the American Chemical Society* **2005,** *127* (6), 1632-1633.

161. Everest, M. A.; Black, V. M.; Haehlen, A. S.; Haveman, G. A.; Kliewer, C. J.; Neill, H. A., Hemoglobin adsorption to silica monitored with polarization-dependent

evanescent-wave cavity ring-down Spectroscopy. *Journal of Physical Chemistry B* **2006,** *110* (39), 19461-19468.

162. Martin, W. B.; Mirov, S.; Martyshkin, D.; Venugopalan, R.; Shaw, A. M., Hemoglobin adsorption isotherm at the silica-water interface with evanescent wave cavity ring-down spectroscopy. *Journal of Biomedical Optics* **2005,** *10* (2).

163. Fan, H. F.; Hung, C. Y.; Lin, K. C., Molecular adsorption at silica/CH_3CN interface probed by using evanescent wave cavity ring-down absorption spectroscopy: Determination of thermodynamic properties. *Analytical Chemistry* **2006,** *78* (11), 3583-3590.

164. Li, F. P.; Zare, R. N., Molecular orientation study of methylene blue at an air/fused-silica interface using evanescent-wave cavity ring-down spectroscopy. *Journal of Physical Chemistry B* **2005,** *109* (8), 3330-3333.

165. Hannon, T. E.; Chah, S. W.; Zare, R. N., Evanescent-wave cavity ring-down investigation of polymer/solvent interactions. *Journal of Physical Chemistry B* **2005,** *109* (15), 7435-7442.

166. Wang, X. F.; Hinz, M.; Vogelsang, M.; Welsch, T.; Kaufmann, D.; Jones, H., A new approach to detecting biologically active substances with evanescent-wave cavity ring-down spectroscopy. *Chemical Physics Letters* **2008,** *467* (1-3), 9-13.

167. van der Sneppen, L.; Ariese, F.; Gooijer, C.; Ubachs, W., Liquid-Phase and Evanescent-Wave Cavity Ring-Down Spectroscopy in Analytical Chemistry. *Annual Review of Analytical Chemistry* **2009,** *2*, 13-35.

168. van der Sneppen, L.; Buijs, J. B.; Gooijer, C.; Ubachs, W.; Ariese, F., Evanescent-wave cavity ring-down spectroscopy for enhanced detection of surface

binding under flow injection analysis conditions. *Applied Spectroscopy* **2008,** *62* (6), 649-654.

169. Tarsa, P. B.; Rabinowitz, P.; Lehmann, K. K., Evanescent field absorption in a passive optical fiber resonator using continuous-wave cavity ring-down spectroscopy. *Chemical Physics Letters* **2004,** *383* (3-4), 297-303.

170. (a) Tong, Z. G.; Wright, A.; McCormick, T.; Li, R. K.; Oleschuk, R. D.; Loock, H. P., Phase-shift fiber-loop ring-down spectroscopy. *Analytical Chemistry* **2004,** *76* (22), 6594-6599; (b) Tong, Z. G.; Jakubinek, M.; Wright, A.; Gillies, A.; Loock, H. P., Fiber-loop ring-down spectroscopy: A sensitive absorption technique for small liquid samples. *Review of Scientific Instruments* **2003,** *74* (11), 4818-4826.

171. Li, R. K.; Loock, H. P.; Oleschuk, R. D., Capillary electrophoresis absorption detection using fiber-loop ring-down spectroscopy. *Analytical Chemistry* **2006,** *78* (16), 5685-5692.

172. Tarsa, P. B.; Wist, A. D.; Rabinowitz, P.; Lehmann, K. K., Single-cell detection by cavity ring-down spectroscopy. *Applied Physics Letters* **2004,** *85* (19), 4523-4525.

173. Truskey, G. A.; Yuan, F. P. D.; Katz, D. F., *Transport phenomena in biological systems*. Pearson/Prentice Hall: Upper Saddle River, N.J., 2004.

Chapter 2. Experimental Set-up

This chapter describes the EW-CRDS experimental set-up, and the electrochemical and flow-cell apparatus used in the experiments described in Chapters 3, 4, 5 and 6. Additionally, since the mathematical models developed in this thesis were solved numerically using the finite element method, a discussion of the finite element method is included.

2.1 Ring-Cavity Apparatus

The EW-CRDS set-up used for the majority of the experiments described in this thesis is shown in Figure 2.1. The cavity used in this set-up was a triangular ring-cavity consisting of two high-reflectivity concave mirrors with reflectivity, R = 99.997% at 405 nm, and radii of curvature of 1 m (Los Gatos Research), and a 90° fused bending prism from CVI (made from UV-grade fused silica) or Laser Components (made from suprasil). The mirrors were mounted on adjustable gimbal mounts to a commercially available breadboard for aligning purposes. The prism had a custom-built mount which was also attached to the breadboard. The design of the prism mount was such that there was complete control over the height of the prism relative to the mirrors, and so that necessary adjustments in the tilt of the prism in the plane of the breadboard could be made.

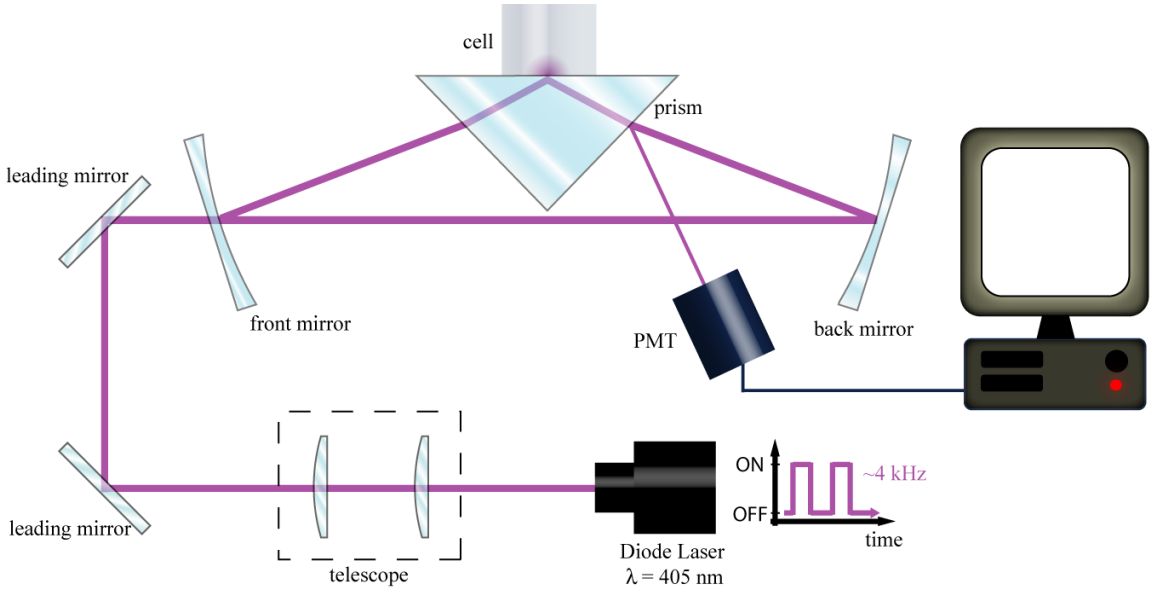

Figure 2.1 The EW-CRDS set-up used for the majority of the experiments described in the following chapters. The output of a diode laser passes through various optics (see text) before being coupled into a tringular optical cavity consisting of two high reflectivity mirrors and a 90º bending prism.

The light source was the output of a pulsed diode laser operating at 405 nm (Power Technology Inc., 50 mW maximum output) with a bandwidth of ~ 1 nm. The relative "broadband" nature of this laser in comparison with other cw-lasers employed in cavity ring-down spectroscopy meant that the laser output excited thousands of cavity modes negating the need for mode-locking. The laser was modulated at 5 kHz using a TTi pulse generator (TGP110). The pulses were typically 5 μs long with a 2 ns rise and fall time which was sufficiently long for the intracavity light intensity to reach a steady value. The light was passed through a telescope (consisting of two lenses with focal lengths 75 mm and 35 mm) to ensure the beam was collimated and to decrease the footprint of the laser beam before being introduced into the cavity through the front mirror. The beam was aligned along the optical axis of the mirrors by means of the two leading mirrors (coated with a MgF dielectric layer - Newport). The light was reflected from the back mirror into

the prism where it hit the entrance face at 36º to the normal. As the incidence was not perpendicular, the entrance and exit faces were anti-reflective coated so that R < 0.5% in the wavelength range 350-532 nm at 34-38º incidence to the normal. The intracavity light intensity was monitored at all times by measuring the reflected light from the entrance face of the prism using a photomultiplier tube (PMT, Electron Tubes, 9781B). This is in contrast to most set-ups where the light transmitted through the back mirror is measured. The advantage to measuring the light reflected from the prism surface was the higher intensity here (0.5% reflected from the prism surface compared to 0.003% transmitted through the mirrors) increasing the signal-to-noise ratio. The PMT signal was digitised on a 12-bit 400 MS/s oscilloscope card (Gage CS12400) and the ring-down time from each transient was calculated with the fast Fourier transform method[1] using custom-written LabVIEW software. Typical ring-down times were between 50 ns and 800 ns. A typical ring-down trace together with a fit to a single exponential function are shown in Figure 2.2.

Prior to each experiment the prisms were cleaned in oxygen plasma in an Emitech K1050X plasma asher for between 3 and 5 minutes to remove organic materials. The prisms were placed in a custom built Teflon holder designed to expose only the total internal reflection face and to protect the antireflective coatings.

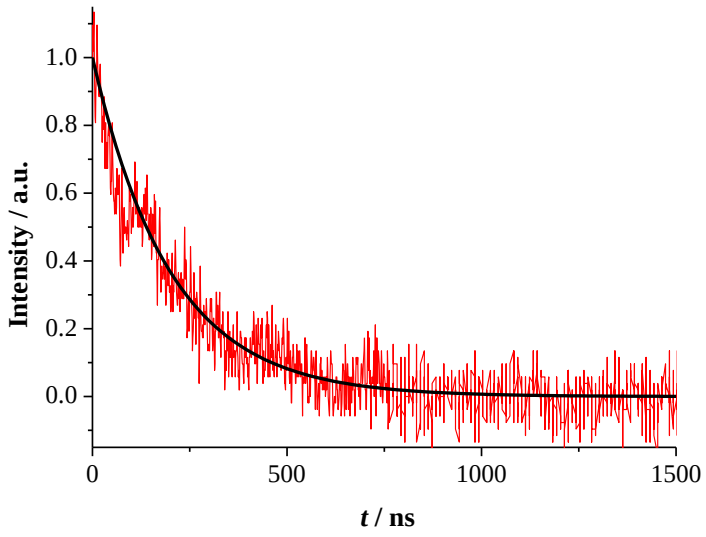

Figure 2.2 The data from a typical ring-down event. The black line is an exponential decay fit to the data.

The interface of interest was probed by absorption/scattering within the evanescent field established within solution during the total internal reflection of light at the hypotenuse facet of the prism. The area probed was estimated to be 8 mm^2. The total length of the cavity was 56.4 cm. From the geometry of the cavity, the penetration depth of the evanescent field (namely the distance from the interface at which the field intensity has decreased by a factor of e^{-1}), d_p, can be calculated using the following formula:[2]

$$d_p = \frac{\lambda}{2\pi\sqrt{n_1^2 \sin^2\theta - n_2^2}} \qquad (2.1)$$

where λ is the wavelength of light, θ is the angle of incidence at the total internal reflection interface, and n_1 and n_2 are the refractive indices of the fused silica prism ($n_{\text{fused silica}}$ = 1.47 or n_{suprasil} = 1.52) and the solution (n_{water} = 1.34), respectively. The angle of incidence was found to be 68.4° from geometry which is just larger than the critical

angle of 66.1º required for total internal reflection at the fused silica-water interface. The penetration depth calculated using equation (2.1) was 242 nm. In order to contain the solution of interest on top of the prism surface, the two different cells that were used are shown in Figure 2.3. For static experiments where only the equilibrium of a surface process was of interest, typically a Teflon cuboidic flow cell was used. When it was necessary to use small sample volumes and for electrochemistry and flow experiments, a simple cylinder of Plexiglass (inner diameter 1.5 cm) was used. Both were secured to the prism surface with the use of contact pressure and an o-ring machined into the bottom of the Plexiglass/Teflon cell wall.

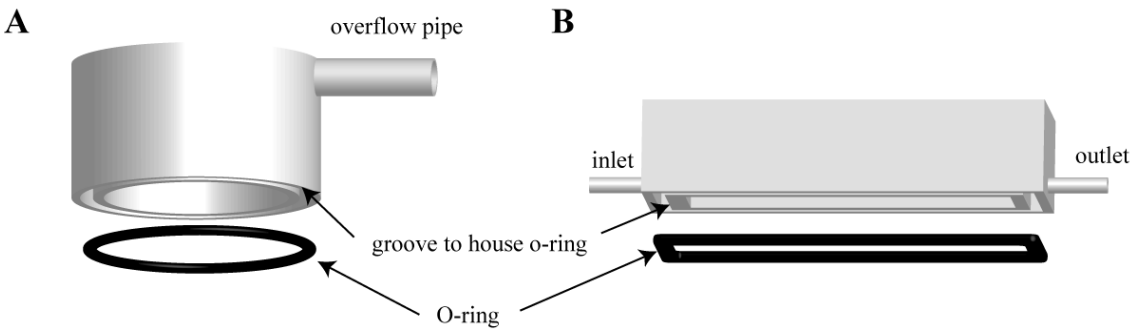

Figure 2.3 Schematics of the cells used in EW-CRDS experiments to contain solution on top of the prism (not to scale). A) The cylindrical cell used for electrochemical and flow experiments. B) The Teflon cuboidic flow cell used for equilibrium measurements to permit the quick exchange of solutions in between measurements.

It is also possible to estimate the effective path length, d_{eff}, from geometry in the case of low optical absorption. The effective path length in the directions parallel and perpendicular to the interfacial plane can be calculated using

$$d_{\text{eff}\perp} = \frac{n_{21}\lambda\cos\theta}{\pi\left(1-n_{21}^{\ 2}\right)\left(\sin^2\theta - n_{21}^{\ 2}\right)^{1/2}} \qquad (2.2)$$

$$d_{\text{eff}\parallel} = \frac{n_{21}\lambda\cos\theta\left(2\sin^2\theta - {n_{21}}^2\right)}{\pi\left(1-{n_{21}}^2\right)\left[\left(1+{n_{21}}^2\right)\sin^2\theta - {n_{21}}^2\right]\left(\sin^2\theta - {n_{21}}^2\right)^{1/2}} \qquad (2.3)$$

where $n_{21} = n_2 / n_1$.[3] Provided the instrument efficiency is identical for *s*- and *p*-polarisations, the d_{eff} can be taken as the average of $d_{\text{eff}\perp}$ and $d_{\text{eff}\parallel}$. For the fused silica-water interface, d_{eff} = 1.5 μm and for the suprasil-water interface d_{eff} = 640 nm. Both the penetration depth and effective path length are extremely sensitive to the refractive indices and the incident angle, therefore these figures are provided only as estimates.

2.2 Combining EW-CRDS with Electrochemical and Fluidic Methods

The use of dynamic electrochemistry or flow to introduce species on a rapid timescale and in a well-defined manner would open up several interesting possibilities in the study of interfacial processes, notably the possibility of accessing fast reaction kinetics or even measuring titrations more rapidly than the static studies that are typically performed using EW-CRDS.

In the experiments described in the following chapters, EW-CRDS was combined with electrochemistry by positioning a working electrode (diameter 2 mm) close to the prism surface (typically between 100 μm and 1 mm away), directly over the region probed by EW-CRDS (see Figure 2.4). The separation between the electrode and the silica surface was controlled in three dimensions using a micropositioner. Previous work has shown that under steady-state conditions at ultramicroelectrodes this is a well-defined process.[4] Additionally, experiments in this set-up in which the concentration of ferricyanide in the evanescent field was measured using EW-CRDS whilst the electrode

was used to change the relative concentrations of ferricyanide and ferrocyanide in the thin layer cell formed between the electrode and prism showed that experimental results agreed well with theory.[5]

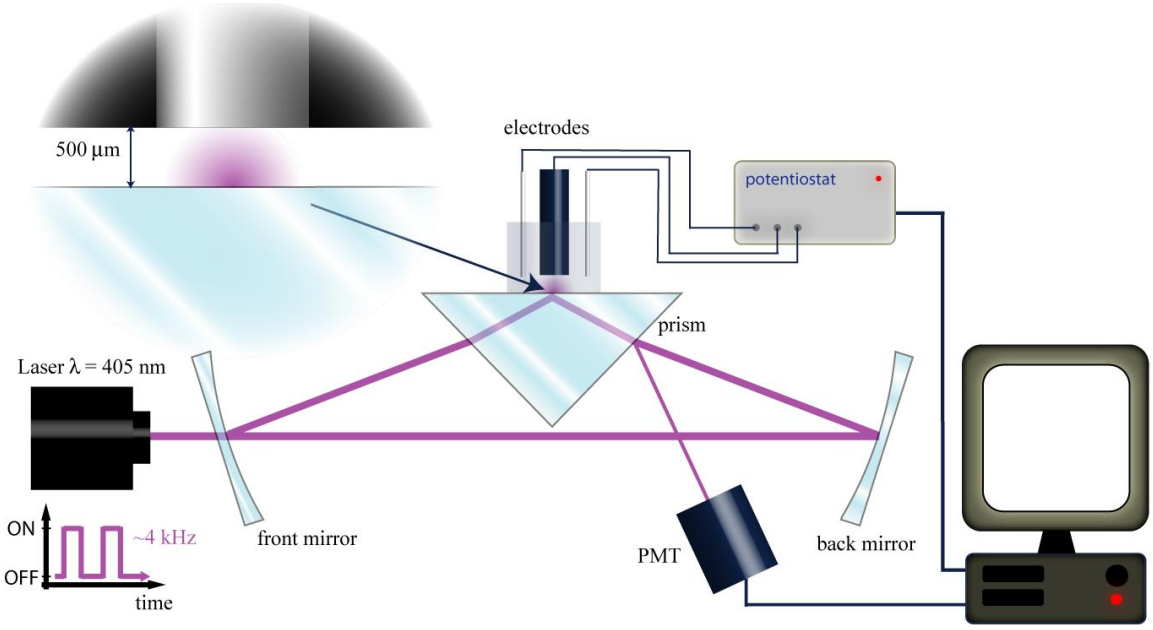

Figure 2.4 Schematic showing the combination of EW-CRDS with electrochemical methods. The working electrode was positioned directly over the point of total internal reflection, a few hundred micrometres from the surface, using a micropositioner and was used to induce a reaction in the region of the evanescent field. The effect of the reaction on the concentrations of species within the evanescent field can be monitored using EW-CRDS.

For the flow set-up, a Teflon nozzle (inner diameter: 2 mm, outer diameter: 8 mm) was positioned directly over the prism surface over the evanescent field. Controlled flow conditions were achieved with a syringe pump (KD Scientific) connected to the Teflon nozzle by plastic tubing. As with the electrochemical experiments, the separation between the end of the nozzle and the silica surface was controlled in three dimensions using a micropositioner, and was typically a few hundred micrometres. Depending on the syringe used for flow, flow rates of up to 10.6 mL min^{-1} were accessible. A hole

drilled into the top of the cell connected to a pipe (diameter 5 mm) acted as a drainage point to ensure the solution did not overflow onto the prism. The drain was considered sufficiently far away from the region of interest so as not to affect the flow in the gap between the prism and nozzle, which was therefore assumed to be axisymmetric. Previous work in which the flow of a microjet impinging on a solid surface was monitored using confocal laser scanning microscopy and the results compared to those generated by a computer simulation of the flow, has shown that flow under similar conditions is well-defined.[6]

2.3 Calculating Absorbance Values and Surface Coverage

Optical absorbance in the evanescent field was calculated using equation (1.4). As previously explained, the d_p of the evanescent field was calculated to be approximately 242 nm which means that the area probed by EW-CRDS extends slightly beyond the interface. Consequently, the optical absorbance, A, measured using EW-CRDS will be the sum of the absorbance due to surface-bound species, A_s, and the absorbance due to species in the bulk solution, A_b. Therefore, in all experiments it was necessary to determine the contribution to the absorbance from the bulk in order to calculate the absorbance due to surface-bound species (and hence the surface coverage). The optical absorbance can be corrected for the bulk absorbance using

$$A_s = A - A_b \tag{2.4}$$

and then the Beer-Lambert Law can be used to determine the surface coverage from A_s.

2.4 Modelling Using COMSOL Multiphysics

Modelling of the experimental data was carried out using the commercially available software package COMSOL Multiphysics. Essentially, COMSOL Multiphysics provides approximate solutions to differential equations using the finite element method. As with most numerical methods for solving partial differential equations, the finite element method approximates the solution by turning the differential equations into a set of linear algebraic simultaneous equations which are comparatively easy to solve. Finite difference methods achieve this by applying a grid to the domain on which the equations are to be solved and then the approximate solution at the grid points is calculated by turning the differential equations into algebraic equations by approximating the derivatives using finite differences (hence the name). In contrast, the finite element method obtains the solution to differential equations by approximating the solution with a function from a finite dimensional function space. The domain of interest is partitioned into elements which can be of any shape including triangular, rectangular, hexagonal in 2D, and tetrahedral and hexahedral in 3D (see Figure 2.5). This process is called meshing and the resulting set of elements is called the mesh. Upon each element, a basis function ϕ_i is defined and the idea is that the solution to the equations can be approximated by a sum over all of the basis functions:

$$u(\underline{x},t) \approx \sum_{i=1}^{N} u_i \phi_i(\underline{x},t) \qquad (2.5)$$

where N is the number of elements in the domain. Substituting the expression in equation (2.5) into the differential equations and performing appropriate integration (the ϕ_i are generally chosen to be of a form that is simple to integrate, for example

polynomials) yields a set of simultaneous equations for the u_i, which can easily be solved. As N increases and consequently the size of the elements decreases, the accurary of the approximate solution increases. The advantage of the finite element method over finite difference methods is the greater flexibility over the mesh which allows the partitioning of potentially awkward domains (for example with curved surfaces) and the ability to partition the domain more finely in areas where the solution is expected to change more rapidly to obtain a more accurate solution without the computational overhead of creating a fine grid across the entire domain.

COMSOL Multiphysics is a commercially available software package which provides a powerful graphical user interface in which to draw a domain, create a mesh and define multiple equations on multiple variables, which may or may not be interdependent. The package provides numerous solver algorithms for stationary, time-dependent and eigenvalue problems depending on the physics to be solved for. Once solved, post-processing functions are provided to visualise the solution, extract the solution, calculate fluxes and perform integrals across domains, subdomains and boundaries. In this chapters that follow, all mathematical models were solved numerically using the finite element method in COMSOL Multiphysics.

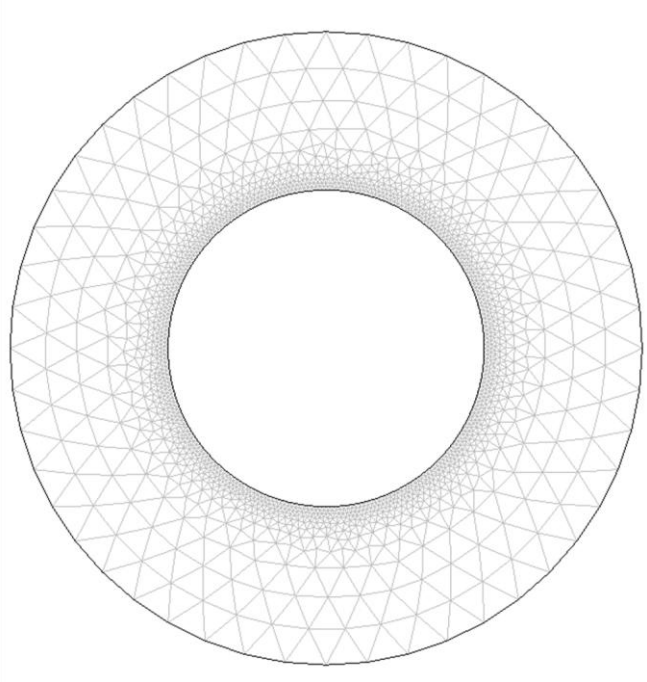

Figure 2.5 An irregular domain which has been meshed with triangular elements. Clearly the domain is much better represented by this triangular mesh than it would be with a grid, highlighting the advantage of using the finite element method over finite difference methods for such domains. Also note how the mesh can be chosen to be finer over certain areas of the domain, for example, where fluxes are expected to be large, to increase the accuracy of the solution.

2.5 References

1. Mazurenka, M.; Wada, R.; Shillings, A. J. L.; Butler, T. J. A.; Beames, J. M.; Orr-Ewing, A. J., Fast Fourier transform analysis in cavity ring-down spectroscopy: application to an optical detector for atmospheric NO_2. *Applied Physics B-Lasers and Optics* **2005,** *81* (1), 135-141; Everest, M. A.; Atkinson, D. B., Discrete sums for the rapid determination of exponential decay constants. *Review of Scientific Instruments* **2008,** *79* (2).

2. Fornel, F. d., *Evanescent waves from Newtonian optics to atomic optics*. Springer: Berlin ; London, 2001.

3. Harrick, N. J.; Carlson, A. I., Internal reflection spectroscopy - validity of effective thickness equations. *Applied Optics* **1971,** *10* (1), 19-&.

4. Rudd, N. C.; Cannan, S.; Bitziou, E.; Ciani, L.; Whitworth, A. L.; Unwin, P. R., Fluorescence confocal laser scanning microscopy as a probe of pH gradients in electrode reactions and surface activity. *Analytical Chemistry* **2005,** *77* (19), 6205-6217.

5. Mazurenka, M.; Wilkins, L.; Macpherson, J. V.; Unwin, P. R.; Mackenzie, S. R., Evanescent wave cavity ring-down spectroscopy in a thin-layer electrochemical cell. *Analytical Chemistry* **2006,** *78* (19), 6833-6839.

6. Bitziou, E.; Rudd, N. C.; Edwards, M. A.; Unwin, P. R., Visualization and Modeling of the hydrodynamics of an impinging microjet. *Analytical Chemistry* **2006,** *78* (5), 1435-1443.

Chapter 3. Probing the Interaction of Tris(2,2'-bipyridine)ruthenium(II) with Silica Surfaces and Polyelectrolyte Films

This chapter describes the application of EW-CRDS to study the interaction of the tris(2,2′-bipyridine)ruthenium(II) complex, $[Ru(bpy)_3]^{2+}$, at both native silica surfaces and surfaces modified with polyelectrolyte films. Both poly-L-lysine (PLL) and PLL/poly-L-glutamic acid (PGA) bilayer functionalised interfaces have been studied. Concentration isotherms exhibit Langmuir-type adsorption behavior on both silica and PGA-terminated surfaces from which equilibrium constants have been derived. The pH-dependence of the $[Ru(bpy)_3]^{2+}$ adsorption to silica and the PLL/PGA film has also been investigated. For the latter substrate, the effective surface pK_a of the acid groups was found to be 5.5. The effect of supporting electrolyte was also investigated and was shown to have a significant effect on the extent of $[Ru(bpy)_3]^{2+}$ adsorption. The thin-layer electrochemical cell arrangement described in Section 2.2, was used to change the solution pH in a controlled way via the potential-pulsed chronoamperometric oxidation of water. By measuring the optical absorption using EW-CRDS during such experiments, the desorption of $[Ru(bpy)_3]^{2+}$ from the surface has been monitored in real time. Experiments were carried out at different cell thicknesses and at various pulse durations. By combining data from the EW-CRDS experiments with CLSM to determine the pH at the substrate surface, the pK_a of the PLL/PGA film could be ascertained and was found to agree with the static pH isotherm measurements. These studies provided a platform for

the further use of electrochemistry combined with EW-CRDS to investigate dynamic processes at modified-silica surfaces such as reported in Chapter 6.

3.1 Introduction

Tris(2,2'-bipyridine)ruthenium(II) ($[Ru(bpy)_3]^{2+}$ - see Figure 3.1) is a widely used reagent in electrochemiluminescence (ECL) analysis.[1] Many efforts have been made to transfer $[Ru(bpy)_3]^{2+}$ directly to sensing electrodes in order to obtain reusable and simple detection devices. For example, $[Ru(bpy)_3]^{2+}$ has been immobilised into sol-gel systems such as titania,[2] ultrathin polymer films such as Nafion[3] or on metal nanoparticles,[4] carbon nanotubes composites[5, 6] and nanotube electrodes.[6] Immobilised ruthenium complexes are also used extensively in dye sensitised solar cells[7]. Clearly, knowledge of the adsorption properties of $[Ru(bpy)_3]^{2+}$ is important for optimizing these many and varied applications.

The silica surface can easily be modified by multilayer assemblies of polyelectrolytes such as poly-L-lysine (PLL) and poly-L-glutamic acid (PGA) thereby changing the electrostatic properties of the surface and facilitating the study of different electrostatic interactions. The resulting surface charge is positive in the case of PLL or negative in the case of a PLL/PGA bilayer. As well as finding applications in the aforementioned technologies, polypeptide multilayer films have found a wealth of applications in medicine for example as polypeptide microcapsules for drug delivery[8] or for anti-microbial protection[9].

3.2 Experimental

3.2.1 Materials and Methods

Tris(2,2′-bipyridine) dichlororuthenium(II), poly-L-lysine hydrobromide, poly-L-glutamic acid sodium salt, tetrabutylammonium chloride, (TBACl), NaCl and fluorescein were purchased from Sigma-Aldrich. $[Ru(bpy)_3]^{2+}$ was stored in the dark. Solutions of different $[Ru(bpy)_3]^{2+}$ concentrations and pH values were freshly prepared prior to experiments. The pH was adjusted using HCl (Fisher Scientific) or $HClO_4$ (Acros) and NaOH (Fisher Scientific).

For studies of modified surfaces, the basal surface of the prism was coated with PLL using the drop coating method. The film was deposited from 1 mg mL^{-1} solutions for adsorption times of 20 min. After adsorption of the polymer, the prisms were rinsed with ultra pure Milli-Q water and dried in an air flow. This yielded an intrinsically positively charged surface. The same procedure was used to deposit a PGA film onto a previously deposited PLL film in order to achieve a negatively charged surface onto which $[Ru(bpy)_3]^{2+}$ would be strongly adsorbed (along with the supporting electrolyte cation).

The extinction coefficient of $[Ru(bpy)_3]^{2+}$ in pure water at 405 nm at various pHs was determined using a Lambda 25 UV-vis spectrometer (Perkin-Elmer Instruments) using a 1 cm quartz cuvette.

3.2.2 Adsorption Experiments

The EW-CRDS set-up was as described in Section 2.1. The surfaces investigated were either bare fused silica or polymer-modified fused silica. For experiments on fused silica, adsorption isotherms at two different pH values (2.7 and 6.7) were recorded over a

wide range of concentrations and were recorded in random order. Additionally, the pH-dependence of the adsorption was investigated at a fixed concentration of 1 mM $[Ru(bpy)_3]^{2+}$, with and without supporting electrolyte (0.1 M NaCl, Aldrich). Between each measurement the cell was rinsed with ultra pure Milli-Q water until the background ring-down signal was recovered, indicating that the prism surface was clean.

Isotherms and pH-dependence experiments for the adsorption of $[Ru(bpy)_3]^{2+}$ onto polyelectrolyte-functionalised surfaces were performed with and without TBACl. This supporting electrolyte was selected as the tetrabutylammonium cation (TBA^+) is likely to bind less competitively than a cation of higher charge density, such as the sodium ion.[10]

After every experiment, the prisms were cleaned in oxygen plasma for 20 min at 100 W (Emitech, K1050X) with the anti-reflection coatings covered and wiped with methanol (Aldrich, spectroscopy grade).

3.2.3 Electrochemically-Induced Desorption

Chronoamperometric experiments were performed using a homebuilt potentiostat with a Pt working electrode (Ø = 2 mm), a Pt wire counter electrode and a Ag wire coated in AgCl which acted as a Ag/AgCl (saturated AgCl) reference electrode.[11] The potential of the working electrode was stepped from 0.2 V, where no processes occurred, to 1.2 V for a defined period in order to generate protons via water oxidation, thereby decreasing the pH within the thin layer cell from a bulk value, $7 < pH < 8$, in a well-defined manner. At the end of the step the potential was stepped back to 0.2 V. The effects of the duration of the potential step and the prism/electrode separation were examined.

3.2.4 Fluorescence Confocal Laser Scanning Microscopy

CLSM measurements of the pH in the thin layer cell were carried out in an arrangement which mimicked the EW-CRDS measurements, using a cuboidic cell in which a glass substrate was positioned opposite the Pt working electrode described in the previous section. The cell was positioned on the stage of a Zeiss LSM 510, Axioplan 2, confocal microscope. An Argon laser (λ = 488 nm) was used for the excitation of 10 μM fluorescein whose fluorescence was measured in conjunction with a long pass filter (λ = 505 nm). Line scans between the electrode and substrate along the central axis of symmetry of the electrode were obtained every 5 ms, while the potential was stepped in the same manner as for the electrochemically-induced desorption experiments. The supporting electrolyte was 50 mM TBACl and the initial pH of the fluorescein solution was adjusted to 8 using NaOH and $HClO_4$. This ensured that the CLSM measurements matched the EW-CRDS measurements and also allowed the pH to be determined with optimal precision.[12] The same electrode-substrate separations and potential step times as for the electrochemical-induced desorption experiments were investigated. By measuring the spatially-resolved fluorescence profiles as a function of time it was possible to obtain detailed information on the evolution of pH[12, 13] in the thin layer cell.

3.3 Results and Discussion

3.3.1 pH-Dependence of UV-Visible Spectra of $[Ru(bpy)_3]^{2+}$

The following sections describe the spectroscopic study of the extent of adsorption of $[Ru(bpy)_3]^{2+}$ to silica as a function of pH. Therefore it was clearly

important to understand the effect of pH on the extinction coefficient of $[Ru(bpy)_3]^{2+}$ at 405 nm. Figure 3.2 A shows the dependence of the absorbance of $[Ru(bpy)_3]^{2+}$ on the pH of the solution. In the region between pH 2 and pH 10, the absorbance changes by less than 2%.

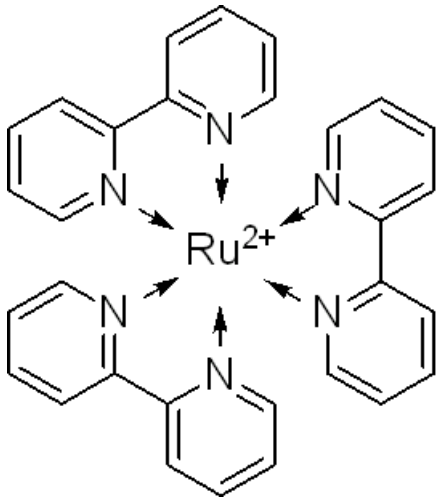

Figure 3.1 Chemical structure of $[Ru(bpy)_3]^{2+}$.

Similarly, the adsorption process was studied with and without TBACl and so UV-visible spectra were obtained for $[Ru(bpy)_3]^{2+}$ with and without TBACl as shown in Figure 3.2 B. The extinction coefficients were found to be $\varepsilon_{405} = 6270$ dm^3 mol^{-1} cm^{-1} for $[Ru(bpy)_3]^{2+}$ in pure water, and $\varepsilon_{405} = 6630$ dm^3 mol^{-1} cm^{-1} for $[Ru(bpy)_3]^{2+}$ in 50 mM TBACl.

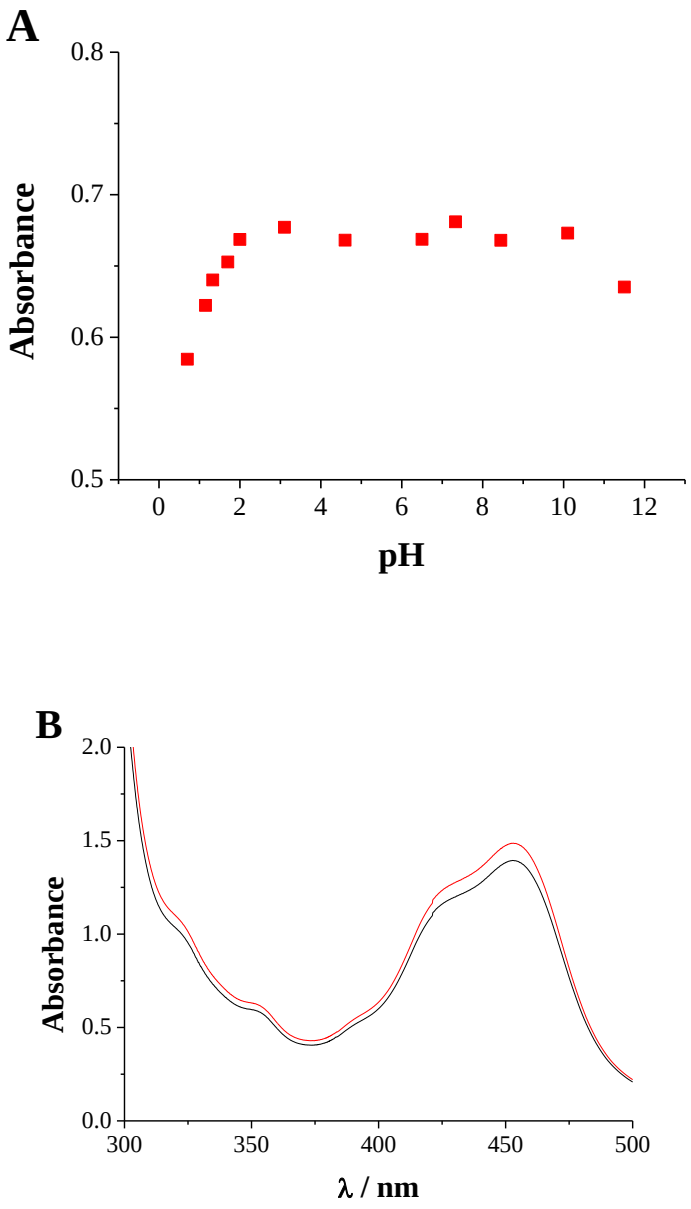

Figure 3.2 A) Dependence on pH of the absorbance at 405 nm of a 100 μM $[Ru(bpy)_3]^{2+}$ solution in pure water. B) UV-visible spectra of 100 μM $[Ru(bpy)_3]^{2+}$ in pure water (black) and in 50 mM TBACl (red).

3.3.2 Bulk Absorbance

The bulk optical absorbance was obtained for $[Ru(bpy)_3]^{2+}$ in solution with a PLL-modified prism surface, on which there was no detectable $[Ru(bpy)_3]^{2+}$ adsorption, so that the optical absorbance, A, with concentration followed the Beer-Lambert law (Figure 3.3). The experimental data were fitted to a straight line which intercepted the origin, with a slope B corresponding to $\varepsilon d_{\text{eff}}$ where ε is the molar absorption coefficient at the wavelength of 405 nm and d_{eff} the effective path length.

$$A = Bc_{\text{Ru}} = \varepsilon d_{\text{eff}} c_{\text{Ru}} \tag{3.1}$$

The gradient of the line was (0.677 ± 0.012) M^{-1} for $[Ru(bpy)_3]^{2+}$ in pure water and (0.727 ± 0.009) M^{-1} for $[Ru(bpy)_3]^{2+}$ in 50 mM TBACl. The difference in the two gradients can be attributed to the slight variation in extinction coefficients at 405 nm for $[Ru(bpy)_3]^{2+}$ in pure water (ε_{405} = 6270 dm^3 mol^{-1} cm^{-1}) and for $[Ru(bpy)_3]^{2+}$ in 50 mM TBACl (ε_{405} = 6630 dm^3 mol^{-1} cm^{-1}). From the slope of the fitting function displayed in Figure 3.3, it was possible to derive an effective optical path length of 1.08 μm which is in fairly good agreement with the effective path length calculated from theory using a low absorption approximation.[14] There was apparently no strong dependence of the effective path length on the electrolyte concentration. The values reported for the slopes were used to correct for the bulk absorbance in the other experiments in this chapter.

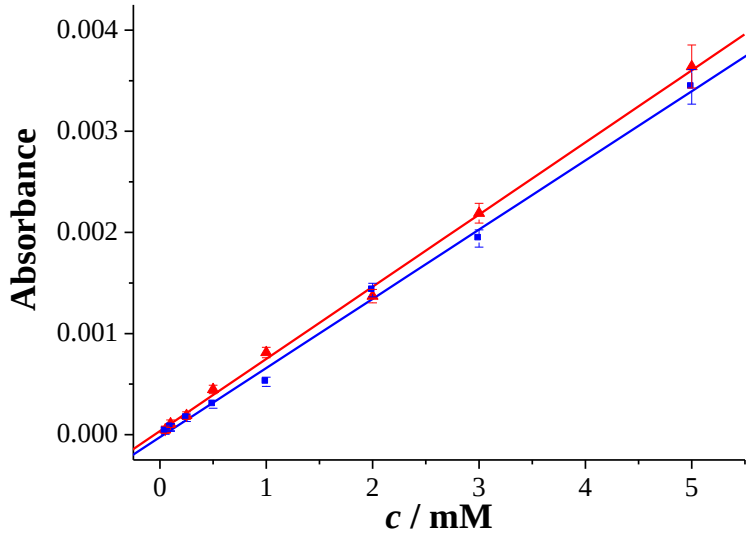

Figure 3.3 Concentration dependence of $[Ru(bpy)_3]^{2+}$ optical absorbance above a PLL-modified silica surface in pure water (blue squares) and 50 mM TBACl (red triangles). The positively charged surface prevents the adsorption of $[Ru(bpy)_3]^{2+}$ and the absorbance measured corresponds to bulk solution absorbance with an effective thickness of 1.08 μm.

3.3.3 Equilibrium Adsorption on Silica

The adsorption of $[Ru(bpy)_3]^{2+}$ on negatively charged surfaces could be promoted on electrostatic grounds, although to the best of our knowledge there have been no previous reports of the adsorption of $[Ru(bpy)_3]^{2+}$ on glass or silica surfaces. The equilibrium adsorption was measured as a function of the bulk concentration of $[Ru(bpy)_3]^{2+}$. Figure 3.4 shows the optical absorbance with time in the evanescent field after the injection (at t = 0) of $[Ru(bpy)_3]^{2+}$ solutions at pH 2.7 (0.5 mM and 1 mM) and 6.7 (1 mM) into the sample cell with an unmodified silica prism. In each case, there is a rapid rise in absorbance due to $[Ru(bpy)_3]^{2+}$ in solution and, in principle, adsorbed on the silica surface. The long time absorbance values for various $[Ru(bpy)_3]^{2+}$ concentrations

and solution pH were obtained by averaging the steady-state values from the long-time plateaus of data such as that in Figure 3.4. By comparing the data in Figure 3.4 for 1 mM at pH 2.7 and 6.7 it is evident that higher pH (more negatively charged silica surface) leads to higher optical absorbance, which can be attributed to the more significant adsorption of $[Ru(bpy)_3]^{2+}$ on the more highly charged surface. Additionally, the morphology of these curves is indicative of the surface process occuring. At pH 2.7, the data plateaus immediately since the absorbance arises only from $[Ru(bpy)_3]^{2+}$ in bulk. In contrast, at pH 6.7, there is an immediate rise in absorbance, followed by a slower increase to the steady-state absorbance value. This slower increase is due to the adsorption of the $[Ru(bpy)_3]^{2+}$ to the silica surface. The concentration dependence of the optical absorption is also evident from the data for 0.5 mM and 1.0 mM $[Ru(bpy)_3]^{2+}$ at pH 2.7.

Figure 3.5 shows the concentration dependence of the optical absorbance of $[Ru(bpy)_3]^{2+}$ at pH 2.7 and pH 6.7 for concentrations up to 3 mM. For both pH values, the absorbance increases with concentration, as would be expected, due to bulk absorbance; but the morphology of the absorbance-concentration curves are clearly strongly pH-dependent. Given the independence of the $[Ru(bpy)_3]^{2+}$ absorbance on pH, the higher interfacial absorbance values at pH 6.7 suggest the enhanced accumulation of $[Ru(bpy)_3]^{2+}$ on the surface at this pH. It is possible to fit the pH 2.7 data to a linear function, because the degree of dissociation of silanol groups is very small at this pH and practically all the optical absorbance originates from $[Ru(bpy)_3]^{2+}$ in bulk solution. The slope of the fitted linear function is $(0.670 \pm 0.096)\ M^{-1}$, which agrees very well with the previously obtained values for the bulk absorbance of $[Ru(bpy)_3]^{2+}$ measured with a PLL-

modified silica surface. For negatively charged surfaces (at higher pH), the absorbance measured by EW-CRDS has two components: i) interfacial, due to surface-adsorbed $[Ru(bpy)_3]^{2+}$ and ii) bulk due to the penetration of the evanescent field into solution as discussed above.

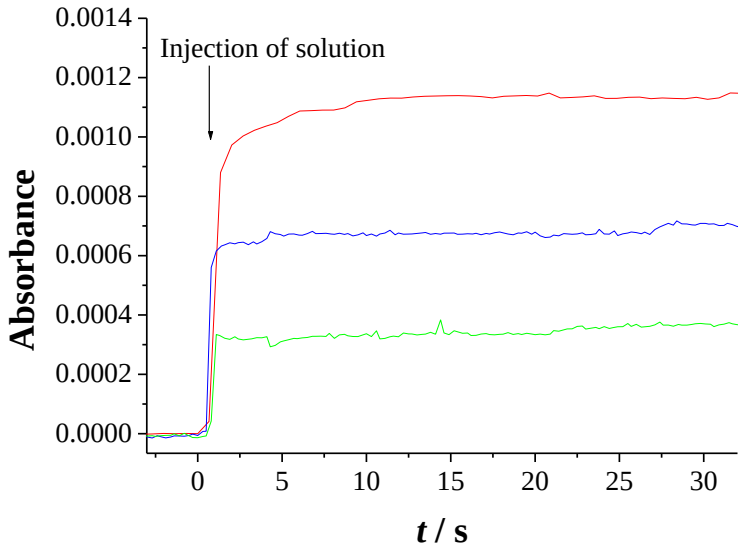

Figure 3.4 Typical optical absorbance transients for $[Ru(bpy)_3]^{2+}$ with a silica substrate as the base of the cell. The concentrations and pH were 0.5 mM, pH 2.7 (green), 1 mM, pH 2.7 (blue), and 1 mM, pH 6.7 (red).

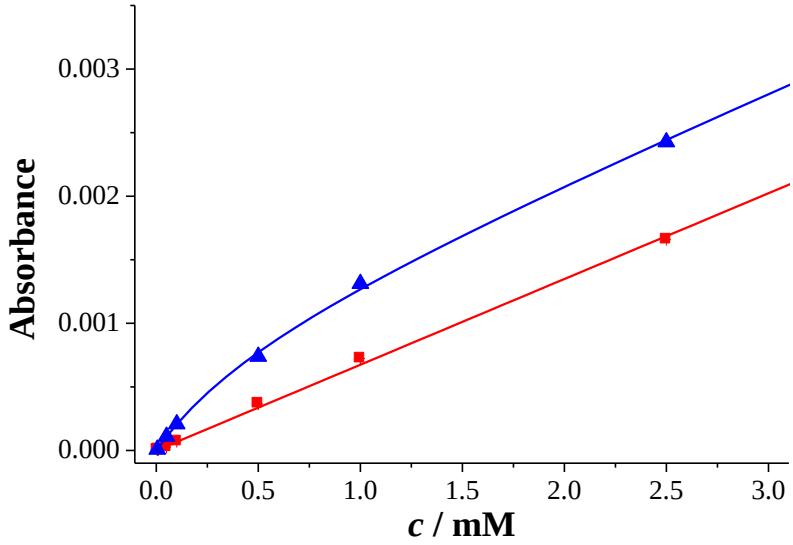

Figure 3.5 Concentration dependence of $[Ru(bpy)_3]^{2+}$ optical absorbance on bare silica as the base of the cell at pH 2.7 (red squares) and pH 6.7 (blue triangles).

In the discussion of the above results one must take account of the surface pK_a of silica functional groups, which are broadly of two types:[15, 16] 19% with a pK_a value of ca. 8.5 and 81% with a pK_a value of ca. 4.5. At pH 6.7, $[Ru(bpy)_3]^{2+}$ will adsorb overwhelmingly on those silanol groups with pK_a 4.5, with negligible adsorption on the sites characterised by the higher pK_a. The experimental pH 6.7 data were therefore fitted to a single Langmuir function, using A_{max} (the maximum optical absorbance at pH 6.7 arising from adsorbed $[Ru(bpy)_3]^{2+}$ when all the adsorption sites are occupied) and the equilibrium constant, K, as fitting parameters. The function naturally included the bulk absorbance, using the gradient, B, obtained from measurements on PLL (or silica at pH 2.7):

$$A = A_{max}\frac{Kc_{Ru}}{1+Kc_{Ru}} + Bc_{Ru} \qquad (3.2)$$

From the fit, the absorbance due to adsorbed $[Ru(bpy)_3]^{2+}$ on silica at pH 6.7 was found to be $A_{max} = (9.50 \pm 0.06) \times 10^{-4}$ and the equilibrium constant $K = (1.72 \pm 0.30) \times 10^3\ M^{-1}$. For the range of bulk $[Ru(bpy)_3]^{2+}$ concentrations investigated, the surface coverage varied from 7.94×10^{-13} mol cm^{-2} to 1.20×10^{-10} mol cm^{-2}. These submonolayer coverages highlight the extreme surface sensitivity of the EW-CRDS method, especially given that the wavelength of the laser used (405 nm) is some way removed from λ_{max} of $[Ru(bpy)_3]^{2+}$ (453 nm).

With the assumptions outlined, the total density of silanol groups, Γ, on the prism surface can be obtained from[15]

$$A_{max} = \Gamma \varepsilon r \alpha \qquad (3.3)$$

where r is the fraction of sites that have pK_a 4.5 and α is the degree of dissociation of these sites at pH 6.7 (99 %). According to Fisk et al.[15] the fraction of these sites is 0.272 which gives Γ = 5.53×10^{-10} mol cm^{-2} or 3.3 groups nm^{-2}, which is in good agreement with previous results.[15, 17]

In order to investigate the pH-dependence of $[Ru(bpy)_3]^{2+}$ adsorption on bare fused silica more fully, the surface concentration of $[Ru(bpy)_3]^{2+}$ was measured as a function of pH from a solution containing 1 mM $[Ru(bpy)_3]^{2+}$ in both pure water and with 0.1 M NaCl. The results in Figure 3.6, which show only adsorbed $[Ru(bpy)_3]^{2+}$ (after subtraction of optical absorption due to solution), show that in the pH range 1-7, the surface concentration of $[Ru(bpy)_3]^{2+}$ increases with increasing pH due to the increasing deprotonation of silanol groups and the consequent increase in the number of possible adsorption sites. At higher pH, the surface concentration actually falls again (at around pH 11 for $[Ru(bpy)_3]^{2+}$ in water and pH 8 for the high ionic strength solution) which can

be attributed to an increase in the ionic strength due to the addition of NaOH used to increase the pH. Na^+ ions appear to compete effectively with the $[Ru(bpy)_3]^{2+}$ to bind to available silanol groups and thus at higher pH (higher $[Na^+]$) fewer SiO^- sites are free to bind $[Ru(bpy)_3]^{2+}$. The same effect is seen for $[Ru(bpy)_3]^{2+}$ in 0.1 M NaCl; the drop in $[Ru(bpy)_3]^{2+}$ surface concentration occurs at around pH 8 due to the fact that NaCl is already present as a supporting electrolyte.

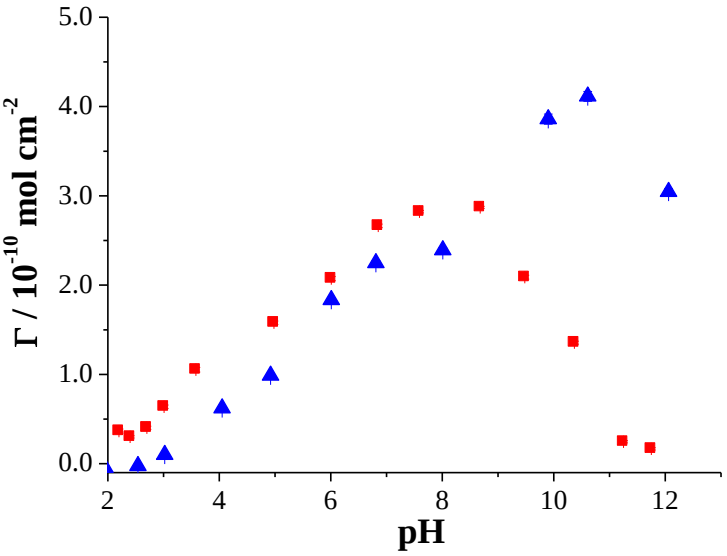

Figure 3.6 pH-dependence (recorded in direction of increasing pH) of $[Ru(bpy)_3]^{2+}$ adsorption on bare silica in pure water (blue triangles) and 0.1 M NaCl (red squares). The bulk $[Ru(bpy)_3]^{2+}$ concentration was 1 mM.

3.3.4 Adsorption on PLL/PGA Bilayers

Isotherms for $[Ru(bpy)_3]^{2+}$ adsorption on a PLL/PGA bilayer, with and without supporting electrolyte (50 mM TBACl) at pH 8, are shown in Figure 3.7 and Figure 3.8 respectively. Both isotherms were obtained from optical absorbance measurements of the type already described, which were corrected for the bulk absorbance and then divided by

ε to reveal the amount of $[Ru(bpy)_3]^{2+}$ on the surface. Compared to the isotherms for silica at pH 6.7, the association of $[Ru(bpy)_3]^{2+}$ with the surface is much stronger at equivalent $[Ru(bpy)_3]^{2+}$ concentrations, particularly when supporting electrolyte is absent. This can be attributed to the increase in the density of adsorption sites on the negatively charged polymer. Furthermore, the surface concentration of $[Ru(bpy)_3]^{2+}$ on PLL/PGA approaches monolayer coverage at much lower bulk concentration compared to similar experiments on silica, again notably with supporting electrolyte absent.

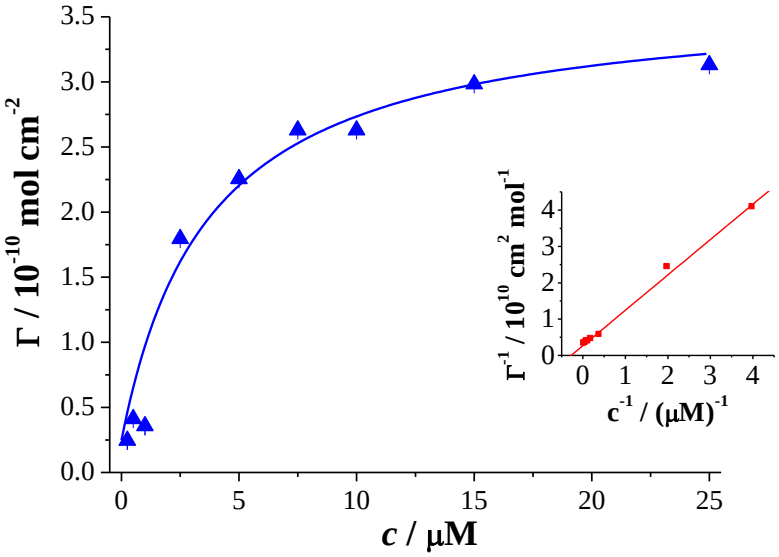

Figure 3.7 Surface concentration of $[Ru(bpy)_3]^{2+}$ achieved on PLL-PGA-modified silica as a function of bulk concentration in pure water at pH 8. The inset shows the data plotted in double recipricol format indicating that the Langmuir isotherm was an appropriate fit to the data.

Comparing Figure 3.7 and Figure 3.8, it can be seen that the addition of supporting electrolyte has a significant impact in decreasing the $[Ru(bpy)_3]^{2+}$ surface concentration, so that monolayer coverage requires a much higher bulk concentration of

$[Ru(bpy)_3]^{2+}$ (note the difference in the concentration ranges of the plots in Figure 3.7 and Figure 3.8). With supporting electrolyte present, the charge of some of the deprotonated acid groups of PGA will be partially screened by the large excess of TBA^+ ions, and a higher concentration of $[Ru(bpy)_3]^{2+}$ is needed in bulk to promote surface adsorption.

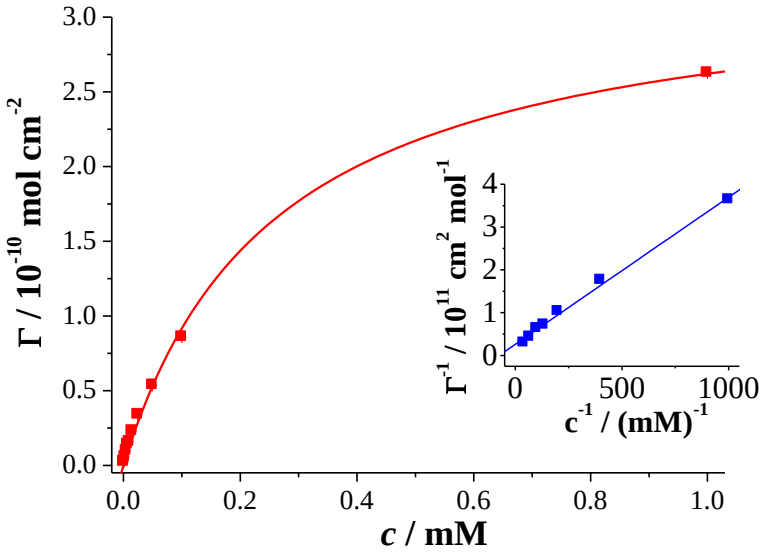

Figure 3.8 Surface concentration of $[Ru(bpy)_3]^{2+}$ achieved on PLL/PGA-modified silica as a function of bulk concentration in 50 mM TBACl at pH 8. The inset shows the data plotted in double recipricol format indicating that the Langmuir isotherm was an appropriate fit to the data.

The experimental data for adsorption of $[Ru(bpy)_3]^{2+}$ to PLL/PGA functionalised silica were fitted to a Langmuir isotherm:

$$A = A_{max} \frac{Kc_{Ru}}{1 + Kc_{Ru}} \qquad (3.4)$$

where A_{max} is the maximum optical absorbance for the adsorbed phase and K again represents the equilibrium adsorption constant. The best fitting parameters were A_{max} = 0.0023 and K = 2.89 × 10^5 M^{-1} with no supporting electrolyte in solution, and A_{max} = 0.0021 and K = 3.85 × 10^3 M^{-1} with 50 mM TBACl.

The pH-dependence of the surface concentration of $[Ru(bpy)_3]^{2+}$ on the PLL/PGA functionalised surface from a solution of 0.1 mM $[Ru(bpy)_3]^{2+}$ without electrolyte is shown in Figure 3.9. The shape of the curve resembles the titration behavior of a weak acid. The curve is fitted to:[18]

$$A = A_{max} \frac{1}{1+10^{pK_a - pH}} + A_{bulk} \qquad (3.5)$$

which gives A_{max} = 4.2 × 10^{-3} and the surface pK_a = 5.5 ± 0.1 which is 1.2 pH units higher than the pK_a of glutamic acid.[19] This increase in pK_a of acid groups upon surface confinement has been seen previously, for example in the work of Bryant and Crooks,[20] and can be attributed to intramonolayer interactions and double layer effects. The data in Figure 3.9 was fit to a model with only one pK_a rather than two, as might seem appropriate from first inspection of the data, as there was only expected to be one type of negatively charged group at the surface.

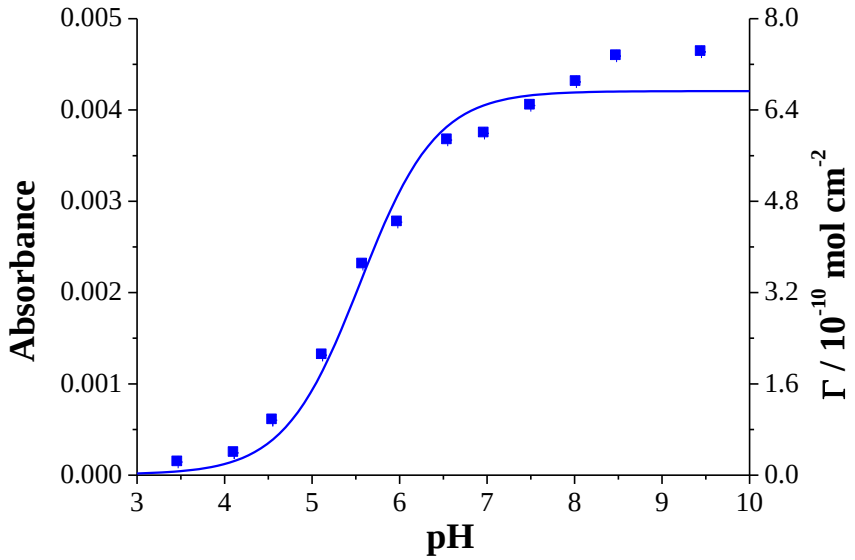

Figure 3.9 pH-dependence of $[Ru(bpy)_3]^{2+}$ surface concentration on PLL/PGA-modified silica from pure water. The bulk $[Ru(bpy)_3]^{2+}$ concentration was 0.1 mM.

3.3.5 Dynamic Adsorption/Desorption Measurements

It is clear from the results above that the extent of the adsorption of $[Ru(bpy)_3]^{2+}$ on various interfaces is strongly pH-dependent. It is possible to use dynamic electrochemistry to change the pH which opens up the possibility of accessing adsorption/desorption kinetics or measuring pH-dependent isotherms more rapidly than in the static studies described above. By positioning a working macroelectrode close to the prism surface the pH can be changed locally by the anodic oxidation of water. We have shown previously for steady-state conditions at ultramicroelectrodes that this is a well-defined process.[12] Here, we characterise time-dependent proton generation at a large electrode.

In order to determine the pH at the prism surface from the anodic oxidation of water, CSLM was used to monitor the fluorescence of fluorescein as a pH indicator.

Fluorescein is a fluorophore whose fluorescence intensity varies sigmoidally from 0 to 100 % within the pH region 4-7.[12] By performing a line scan in the gap between the electrode and a glass substrate (mimicking the prism surface) at the center of the electrode, the fluorescence intensity could be monitored during the production of protons resulting from the chronoamperometric potential step experiment. The intensity could then be used to determine the pH between the electrode and substrate using a calibration curve of fluorescence intensity versus pH similar to that shown previously (Figure 3 in Rudd *et al.* [12]). Typical data from this experiment are shown in Figure 3.10. Figure 3.10 B shows the current response of the electrode due to the applied potential profile shown in Figure 3.10 A. The forward potential step, from 0.2 V to 1.2 V for 2 s, results in an anodic current transient that is accompanied by a change in fluorescence signal at the electrode surface from light to dark, which spreads into the solution as electrogenerated protons diffuse towards the substrate. The reverse potential step is accompanied by a small cathodic current transient. The fluorescence signal in the gap between the electrode and substrate gradually decreases, consistent with some proton generation.

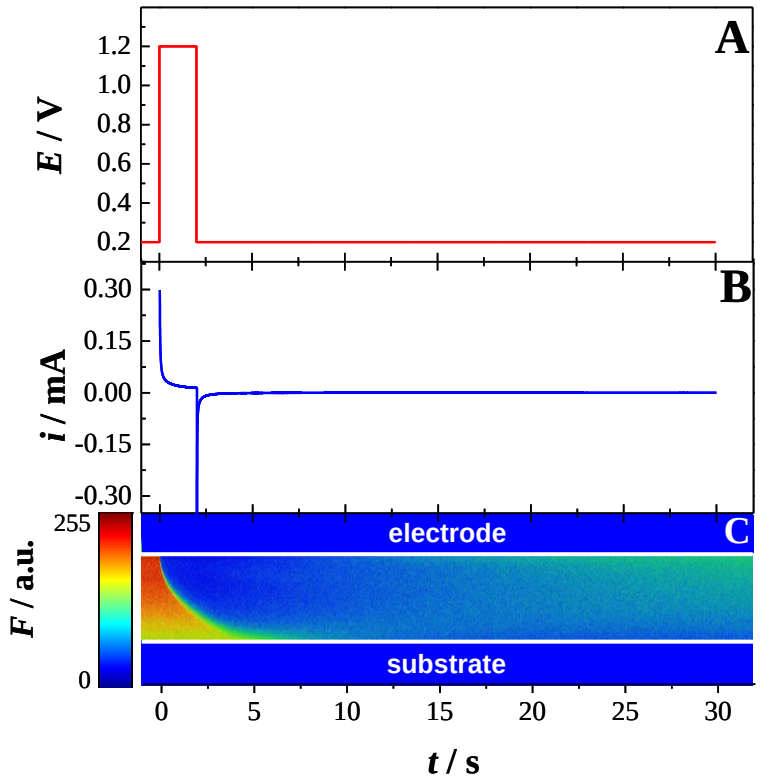

Figure 3.10 Electrochemically-induced $[Ru(bpy)_3]^{2+}$ desorption from a substrate. (A) The potential applied to the working electrode as a function of time and (B) the corresponding current response. (C) The corresponding series of CLSM linescans between the electrode (blue area at the top) and the glass substrate (blue area at the bottom) as a function of time are shown. Relatively high fluorescence corresponds to pH > 7.

Typical examples of the change in pH at the glass substrate, with time, for different electrode-prism separations and potential step times are shown in Figure 3.11 and Figure 3.12, respectively. The measured relative absorbance was converted to pH using a fluorescence intensity-pH plot similar to that reported in Rudd *et al.*.[12] It can be seen that after a lag time which depends on the electrode to glass surface separation, the pH abruptly decreases over a period of 1-2 s and reaches a fairly steady value. The value

attained following the potential perturbation clearly depends on the duration of the pulse and the thickness of the cell: a shorter pulse and thicker cell yield smaller changes in pH.

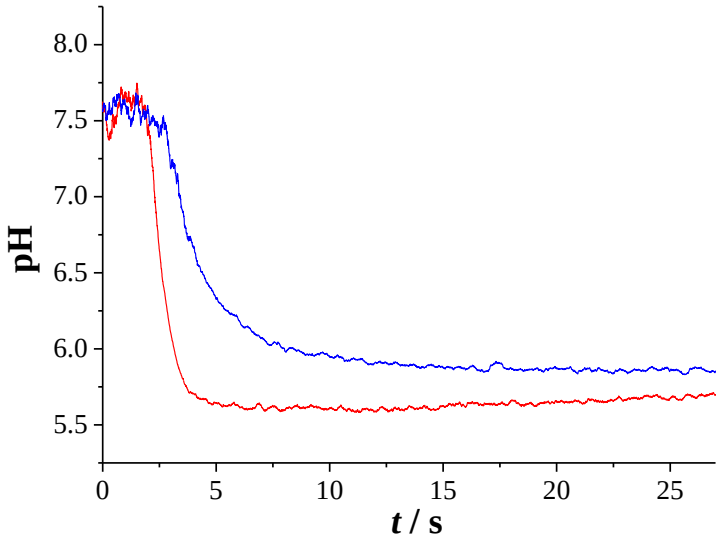

Figure 3.11 Transients showing the pH at the prism surface as determined from CLSM after applying a potential of +1.2 V vs. Ag/AgCl for 2 seconds with prism-electrode separations of 300 μm (red) and 400 μm (blue).

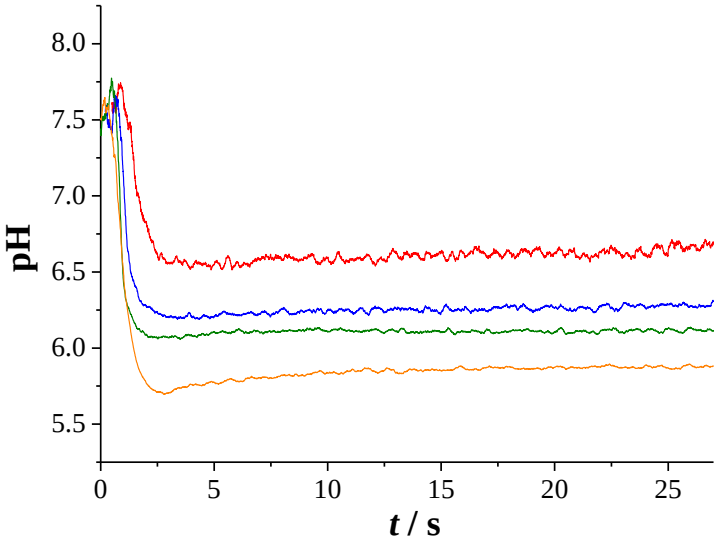

Figure 3.12 Transients showing the pH at the prism surface as determined from CLSM after applying a potential of +1.2 V vs. Ag/AgCl for 100 ms (red), 250 ms (blue), 500 ms (green), 1 s (orange). The electrode-prism separation was 200 μm.

With a detailed knowledge of the pH from these measurements it was possible to carry out similar potential-induced proton generation in the EW-CRDS configuration. Figure 3.13 and Figure 3.14 show typical EW-CRDS absorbance-time plots for a potential step from 0.2 V to 1.2 V and back to 0.2 V vs. Ag/AgCl for different prism/electrode separation distances and pulse generation times. In each case there is a decrease in absorbance following the electrochemical generation of H^+, the morphology of the curves is similar to the CSLM data, showing a strong dependence on pulse width and electrode/prism separation. The larger the separation, the longer the lag time, and the smaller the change in optical absorbance. Likewise, for a given electrode/prism separation, the shorter the pulse width, the smaller the overall pH change and thus the smaller the extent of $[Ru(bpy)_3]^{2+}$ desorption (see Figure 3.14). This is consistent with

proton generation at the electrode causing desorption of $[Ru(bpy)_3]^{2+}$ from the substrate surface.

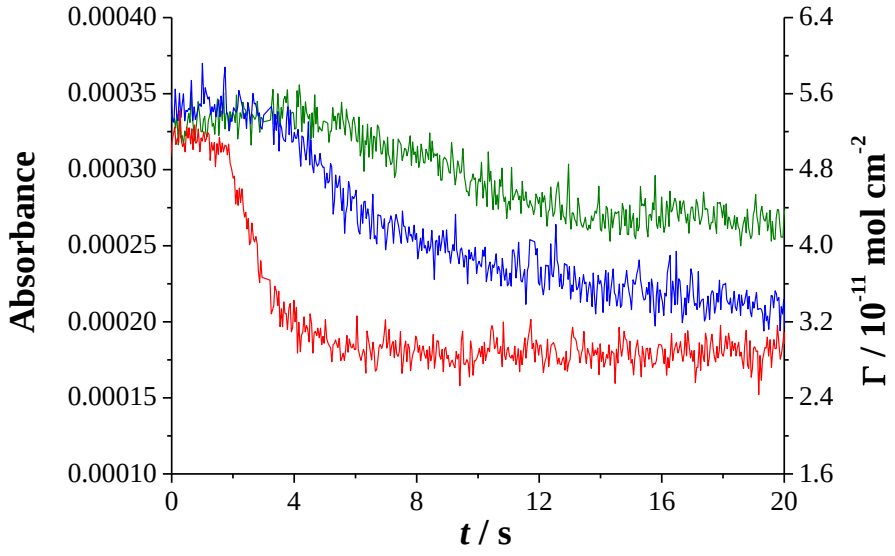

Figure 3.13 Optical absorbance transients of surface-adsorbed $[Ru(bpy)_3]^{2+}$ from a bulk solution of 50 μM $[Ru(bpy)_3]^{2+}$ on PGA after applying a potential of +1.2 V vs. Ag/AgCl for 2 s at different prism-electrode separations: 500 μm (green), 400 μm (blue), 300 μm (red).

The CSLM data yield interfacial pH as a function of time, whilst EW-CRDS yields Γ vs. time. From this we can construct Γ-pH plots, typical examples of which can be seen in Figure 3.15. We may further consider that acid-induced desorption is rather rapid on the timescale of these measurements, so that the amount of $[Ru(bpy)_3]^{2+}$ on the surface is governed by the local pH. The Γ-pH plots can then be analyzed using equation (3.5). The data in Figure 3.15 A and Figure 3.15 B gave best fits to pK_a of 5.5 and 5.9 respectively. The mean pK_a from all data sets was 5.6 ± 0.3 which is in good agreement with the equilibrium pH dependence measurements shown in Figure 3.9.

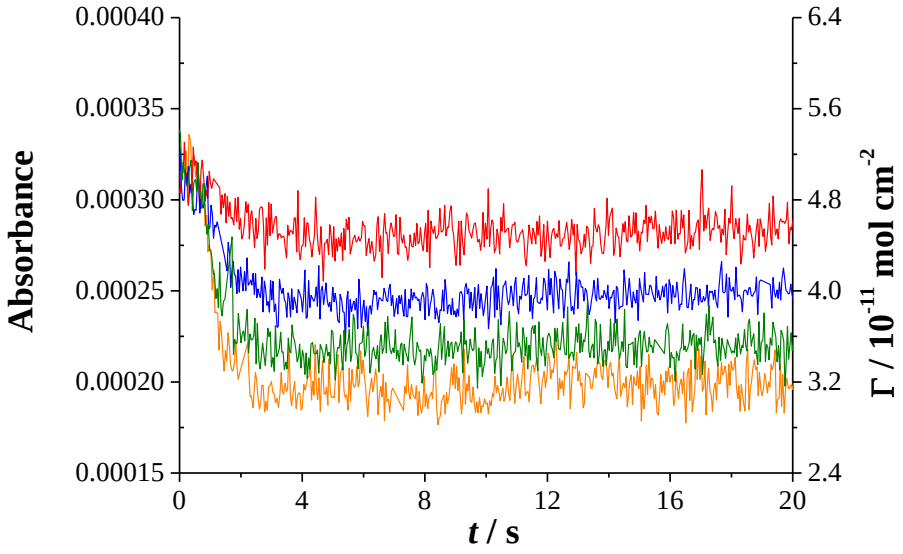

Figure 3.14 Optical absorbance transients of surface-adsorbed $[Ru(bpy)_3]^{2+}$ from a bulk solution of 50 μM $[Ru(bpy)_3]^{2+}$ on PGA after applying a potential of +1.2 V vs. Ag/AgCl for different potential step times: 100 ms (orange), 250 ms (green), 500 ms (blue), 1 s (red). The prism-electrode separation was 200 μm.

3.4 Conclusions

In this chapter it has been shown that EW-CRDS is a valuable technique for probing the pH-dependent adsorption of $[Ru(bpy)_3]^{2+}$ on silica, PLL and a PLL/PGA bilayer. In the case of silica and PLL/PGA, Langmuir-type adsorption isotherms were observed with the adsorption being strongly pH-dependent and influenced by the addition of supporting electrolyte. In contrast, the positively charged PLL surface effectively prevented any adsorption of $[Ru(bpy)_3]^{2+}$.

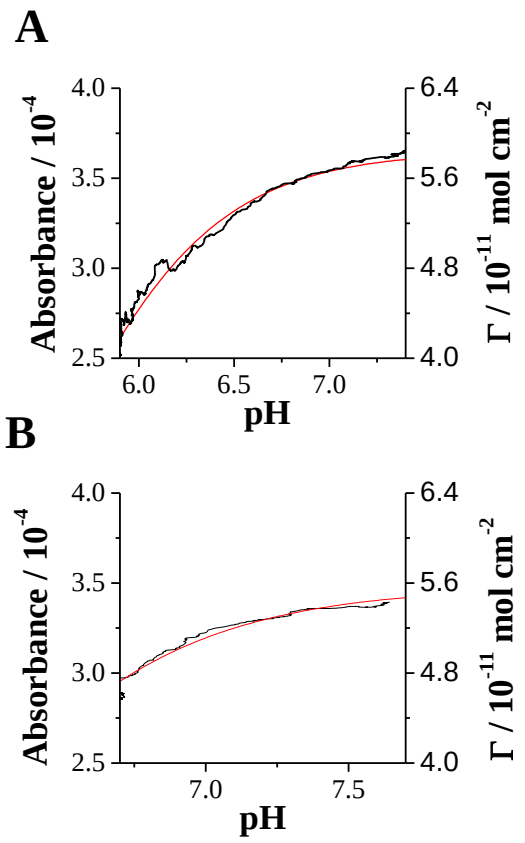

Figure 3.15 Typical plots of optical absorbance for surface-confined $[Ru(bpy)_3]^{2+}$ on PGA versus pH determined from the CLSM measurements. (A) Electrode-prism separation of 400 μm and 2 s potential step time. The red line is the fit to equation (3.5) with pK_a = 5.5. (B) is for and electrode-prism separation of 200 μm and 100 ms potential step time. The red line is the fit to equation (3.5) with pK_a = 5.9.

By combining EW-CRDS with chronoamperometry at an electrode positioned just above the prism surface, the pH could be changed rapidly and quantitatively. By varying the potential step times for proton generation and the electrode/prism separation, it was possible to obtain information on the pH-dependent adsorption of $[Ru(bpy)_3]^{2+}$ on the carboxylic-acid terminated surface. Combined with CSLM to obtain quantitative information on the pH at the prism surface, the adsorption/desorption process was shown

to be governed by the protonation/deprotonation of the PGA film and the surface pK_a of the film was found to be 5.6 consistent with the static pH-titration measurements.

This study was one of the first demonstrations of monitoring adsorption/desorption dynamics at modified-silica surfaces using EW-CRDS, which clearly opens up a wide range of possibilities in biological surface science. This is explored further in Chapter 6.

3.5 References

1. Dennany, L.; O'Reilly, E. J.; Keyes, T. E.; Forster, R. J., Electrochemiluminescent monolayers on metal oxide electrodes: Detection of amino acids. *Electrochemistry Communications* **2006,** *8* (10), 1588-1594; Gerardi, R. D.; Barnett, N. W.; Lewis, S. W., Analytical applications of tris(2,2 '-bipyridyl)ruthenium(III) as a chemiluminescent reagent. *Analytica Chimica Acta* **1999,** *378* (1-3), 1-41.

2. Zhuang, Y. F.; Ju, H. X., Study on electrochemiluminesce of $Ru(bpy_3)^{2+}$ immobilised in a titania sol-gel membrane. *Electroanalysis* **2004,** *16* (17), 1401-1405.

3. Choi, H. N.; Yoon, S. H.; Lyu, Y. K.; Lee, W. Y., Electrogenerated chemiluminese ethanol biosensor based on carbon nanotube-titania-nafion composite film. *Electroanalysis* **2007,** *19* (4), 459-465; Bertoncello, P.; Dennany, L.; Forster, R. J.; Unwin, P. R., Nafion - Tris(2-2'-bipyridyl)ruthenium(II) ultrathin Langmuir - Schaefer films: Redox catalysis and electrochemiluminescent properties. *Analytical Chemistry* **2007,** *79* (19), 7549-7553.

4. Liang, M. M.; Liu, S. L.; Wei, M. Y.; Guo, L. H., Photoelectrochemical oxidation of DNA by ruthenium tris(bipyridine) on a tin oxide nanoparticle electrode. *Analytical*

Chemistry **2006,** *78* (2), 621-623; Kuwahara, Y.; Akiyama, T.; Yamada, S., Construction of gold nanoparticle-ruthenium (II) tris(2,2 '-bipyridine) self-assembled multistructures and their photocurrent responses. *Thin Solid Films* **2001,** *393* (1-2), 273-277.

5. Chaturvedi, H.; Poler, J. C., Binding of rigid dendritic ruthenium complexes to carbon nanotubes. *Journal of Physical Chemistry B* **2006,** *110* (45), 22387-22393; Bottini, M.; Magrini, A.; Di Venere, A.; Bellucci, S.; Dawson, M. I.; Rosato, N.; Bergamaschi, A.; Mustelin, T., Synthesis and characterization of supramolecular nanostructures of carbon nanotubes and ruthenium-complex luminophores. *Journal of Nanoscience and Nanotechnology* **2006,** *6* (5), 1381-1386.

6. Zhuang, Y. F.; Ju, H. X., Determination of reduced nicotinamide adenine dinucleotide based on immobilization of tris(2,2 '-bipyridyl) ruthenium(II) in multiwall carbon nanotubes/Nafion composite membrane. *Analytical Letters* **2005,** *38* (13), 2077-2088.

7. Kuang, D.; Klein, C.; Snaith, H. J.; Humphry-Baker, R.; Zakeeruddin, S. M.; Gratzel, M., A new ion-coordinating ruthenium sensitizer for mesoscopic dye-sensitized solar cells. *Inorganica Chimica Acta* **2008,** *361* (3), 699-706.

8. Leguen, E.; Chassepot, A.; Decher, G.; Schaaf, P.; Voegel, J. C.; Jessel, N., Bioactive coatings based on polyelectrolyte multilayer architectures functionalized by embedded proteins, peptides or drugs. *Biomolecular Engineering* **2007,** *24* (1), 33-41.

9. Boulmedais, F.; Frisch, B.; Etienne, O.; Lavalle, P.; Picart, C.; Ogier, J.; Voegel, J. C.; Schaaf, P.; Egles, C., Polyelectrolyte multilayer films with pegylated polypeptides as a new type of anti-microbial protection for biomaterials. *Biomaterials* **2004,** *25* (11), 2003-2011.

10. Eisenberg, M.; Gresalfi, T.; Riccio, T.; McLaughlin, S., Adsorption of monovalent cations to bilayer membranes containing negative phospholipids. *Biochemistry* **1979,** *18* (23), 5213-5223.

11. Macpherson, J. V.; Beeston, M. A.; Unwin, P. R., Imaging local mass-transfer rates within an impinging jet and studies of fast heterogeneous electron-transfer kinetics using the microjet electrode. *Journal of the Chemical Society-Faraday Transactions* **1995,** *91* (5), 899-904.

12. Rudd, N. C.; Cannan, S.; Bitziou, E.; Ciani, L.; Whitworth, A. L.; Unwin, P. R., Fluorescence confocal laser scanning microscopy as a probe of pH gradients in electrode reactions and surface activity. *Analytical Chemistry* **2005,** *77* (19), 6205-6217.

13. Bitziou, E.; Rudd, N. C.; Edwards, M. A.; Unwin, P. R., Visualization and Modeling of the hydrodynamics of an impinging microjet. *Analytical Chemistry* **2006,** *78* (5), 1435-1443; Cannan, S.; Macklam, I. D.; Unwin, P. R., Three-dimensional imaging of proton gradients at microelectrode surfaces using confocal laser scanning microscopy. *Electrochemistry Communications* **2002,** *4* (11), 886-892.

14. Harrick, N. J.; Carlson, A. I., Internal reflection spectroscopy - validity of effective thickness equations. *Applied Optics* **1971,** *10* (1), 19-&.

15. Fisk, J. D.; Batten, R.; Jones, G.; O'Reilly, J. P.; Shaw, A. M., pH dependence of the crystal violet adsorption isotherm at the silica-water interface. *Journal of Physical Chemistry B* **2005,** *109* (30), 14475-14480.

16. Fan, H. F.; Li, F.; Zare, R. N.; Lin, K. C., Characterization of Two Types of Silanol Groups on Fused-Silica Surfaces Using Evanescent-Wave Cavity Ring-Down Spectroscopy. *Anal. Chem.* **2007,** *79* (10), 3654-3661.

17. Dong, Y.; Pappu, S. V.; Xu, Z., Detection of local density distribution of isolated silanol groups on planar silica surfaces using nonlinear optical molecular probes. *Analytical Chemistry* **1998,** *70* (22), 4730-4735; Cox, G. B., The influence of silica structure on reversed-phase retention. *Journal of Chromatography A* **1993,** *656* (1-2), 353-367.

18. Zhao, X.; Ong, S.; Wang, H.; Eisenthal, K. B., New method for determination of surface pKa using second harmonic generation. *Chemical Physics Letters* **1993,** *214* (2), 203-207.

19. Section 8: Analytical Chemistry. In *CRC Handbook of Chemistry and Physics*, 88th ed.; Lide, D. R., Ed. CRC Press.

20. Bryant, M. A.; Crooks, R. M., Determination of surface pK_a values of surface-confined molecules derivatized with pH-sensitive pendant groups. *Langmuir* **1993,** *9* (2), 385-387.

Chapter 4. Probing Redox Reactions of Immobilised Cytochrome *c*

This chapter reports an investigation of the electron transfer between surface-immobilised cytochrome *c* and the redox couple $FeEDTA^-/FeEDTA^{2-}$ using EW-CRDS and chronoamperometry. The adsorption of cytochrome *c* to the silica prism inherent in the EW-CRDS set-up was monitored using EW-CRDS and the results were in agreement with previous reports. The thin layer cell arrangement described in Section 2.2 was employed to reduce $FeEDTA^-$, the product of which diffused to the prism surface and reduced the cytochrome *c* immobilised on the prism. Using complementary finite element simulations of the diffusion coupled to the surface process, the rate constant of electron transfer was found to be 4.3 (± 0.6) × 10^{-9} cm s^{-1}. This demonstrative study serves as a platform for future studies which could build up the biological complexity of the interface.

4.1 Introduction

Electron transfer (ET) is fundamental to many biological processes. In particular, respiration involves a cascade of ET events between redox proteins.[1] Determining the rates of these ET events, and the mechanisms that drive them is important for understanding metabolic pathways *in vivo*. Furthermore, understanding ET between redox proteins is fundamental to optimising technologies such as biosensors,[2] biofuel cells,[3] heterogeneous catalysts[4] and biomolecular electronic components.[5]

Traditionally, obtaining the kinetics of ET between proteins and redox mediators or other proteins was achieved using stopped flow apparatus and monitoring the change in the redox state of the protein spectroscopically[6], but since the first successful demonstrations of cyclic voltammetry of horse heart cytochrome *c* by Eddowes and Hill [7] and Yeh and Kuwana [8] independently in 1977, the area of the direct and mediated electrochemistry of both ET proteins and complex enzymes has flourished [9].

As mentioned in Chapter 1, Protein Film Voltammetry (PFV) [10] is widely accepted as a powerful tool for understanding ET between proteins and electrodes for the fabrication of devices such as biosensors, in bioelectronics and biofuel cells[6e, f], and as a model for comprehending ET between redox proteins *in vivo* [11]. In PFV, varying the potential at an electrode drives electrons in and out of the active sites of an electroactive protein film immobilised on the electrode, allowing the evaluation of the formal potentials and the rates of electron transfer and other kinetic and thermodynamic parameters [12]. Moreover, PFV has been employed to investigate the mechanisms and rates of ET between the adsorbed proteins and their redox partners [13]. Traditionally, such interactions have been studied in solution mainly using optical techniques, whereas *in vivo*, ET often occurs at interfaces. Although PFV has been very successful in exploring many of these interchanges, it is limited due to the difficulty of orienting the protein in the film in such a way that it can undergo fast electron transfer with the electrode and also dock successfully with its redox partners. Furthermore, since the current response is an indirect measure of ET between proteins, the analysis of the ET kinetics can be challenging. Scanning Electrochemical Microscopy (SECM) has also been applied to study the electrochemistry of a wide range of redox proteins as described in Chapter 1.

4.2 Experimental

4.2.1 Materials

Horse-heart cytochrome *c*, potassium chloride, sodium dithionite and ethylenediaminetetraacetic acid iron(III) sodium salt (Sigma-Aldrich) were used as supplied and stored in the dark. All solutions were prepared in ultrapure Milli-Q water prior to experiments. $FeEDTA^-$ solutions were deoxygenated with N_2 and were subsequently kept under N_2 atmosphere.

4.2.2 UV-Visible Spectroscopy

UV-Visible spectra of the oxidised cytochrome *c* were recorded using a Jasco V660 spectrophotometer. In order to obtain the spectrum of the reduced form, a 100 μM solution was deoxygenated before adding 1 mg ml^{-1} sodium dithionite in excess. The solution was then diluted to 20 μM and the spectrum recorded.

4.2.3 EW-CRDS Set-up

The EW-CRDS set-up was identical to that described in Section 2.1 with the exception of the light source. In these experiments, the second harmonic (generated using Type I β-barium borate crystal) of a commercially available femtosecond Ti-Sapphire laser (SpectraPhysics XP Regenerative amplifier), which had been passed through a single-mode optical fiber, was employed as the light source. The repetition rate was 1 kHz. The advantage of using this laser compared to the diode lasers employed in the experiments described in other chapters was the ability to tune the wavelength. For these studies λ = 400 nm was chosen as the difference in absorption spectra for the reduced

and oxidised forms of cytochrome *c* was more pronounced at this wavelength compared to 405 nm used previously (see Figure 4.2).

4.2.4 Electrochemistry

A platinum working electrode (Pt disc, diameter 2 mm, insulating sheath diameter 6 mm) was positioned over the evanescent field at a distance of a few hundred nanometers from the surface. Electrochemical measurements were performed with a Ag/AgCl quasi reference electrode and a platinum wire counter electrode using a home-built potentiostat. The electrochemical signal was measured using a National Instruments card (NI PCIE-6251 M Series Multifunction DAQ Device). Custom written LabView software ensured optimal synchronization between the EW-CRDS signal and electrochemical data acquisition.

4.3 Results and Discussion

4.3.1 UV-Visible Absorption Spectroscopy

The UV-visible absorption spectra for various concentrations of oxidised cytochrome *c* in 0.1 M KCl are shown in Figure 4.1. The inset shows the absorbance at 400 nm against cytochrome *c* concentration. The line of best fit through the data gave an extinction coefficient for oxidised cytochrome *c* at 400 nm of

ε_O = 5.87 (± 0.08) × 10^4 dm^3 mol^{-1} cm^{-1}.

The UV-visible absorption spectra of the reduced and oxidised forms of cytochrome *c* are shown in Figure 4.2. The positions of the peaks for the reduced spectrum are in good agreement with previously reported cytochrome *c* UV-visible

spectra indicating that the protein is completely reduced.[6e] The extinction coefficients of the reduced form of cytochrome *c* at 400 nm in solution was found to be ε_R = 3.79 × 10^4 dm^3 mol^{-1} cm^{-1}. The values of ε_O and ε_R were used to calculate the coverages of reduced and oxidised cytochrome *c* on the prism surface during the electrochemical experiments.

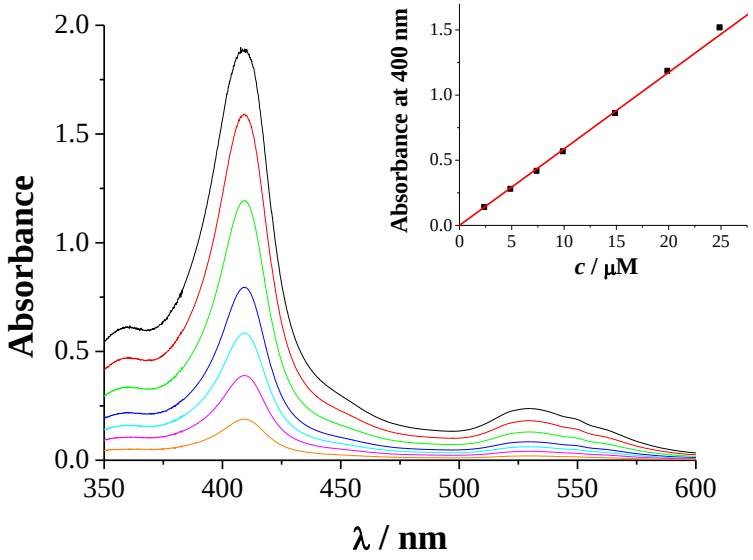

Figure 4.1 UV-Visible absorption spectra of oxidised cytochrome *c* in 0.1 M KCl. The concentrations of cytochrome *c* were 2.5 μM (orange), 5 μM (magenta), 7.5 μM (cyan), 10 μM (blue), 15 μM (green), 20 μM (red) and 25 μM (black). The inset shows the absorbance at 400 nm plotted against the cytochrome *c* concentration. The linear fit to the data gives ε_{400nm} = 58700 dm^3 mol^{-1} cm^{-1}.

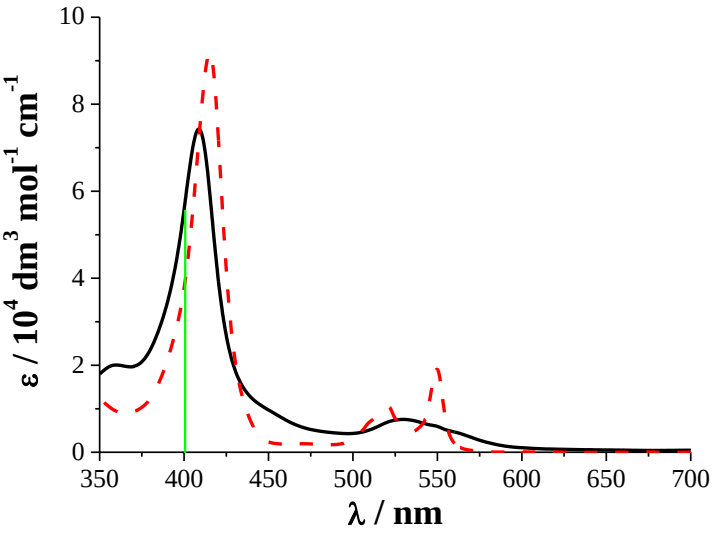

Figure 4.2 UV-visible spectra of the oxidised (black) and reduced (red) forms of cytochrome *c*.

4.3.2 Adsorption of Cytochrome *c* on Silica

Figure 4.3 shows the change in optical absorbance resulting from placing 5 μM of cytochrome *c* in 0.1 M KCl onto the prism surface. The shape of the transient, in which there is a gradual change in optical absorbance up to a limiting value, indicates that the response is due to the adsorption of cytochrome *c* at the interface. Assuming that the extinction coefficient of surface bound cytochrome *c* is the same as in bulk solution[14], the maximum absorbance of 0.004 corresponds to a surface coverage of 6.8×10^{-11} mol cm^{-2}. Assuming that a monolayer of cytochrome *c* would completely cover the surface, and considering that cytochrome *c* is roughly a spherical molecule with diameter 3.4 nm,[15] the maximum monolayer surface concentration was evaluated as approximately 1.8×10^{-11} mol cm^{-2}, much less than the coverage obtained in the data shown in Figure 4.3. We conclude that the cytochrome *c* forms a strongly bound monolayer to the silica surface with weakly bound layers of cytochrome *c* on top. This is corroborated by the

removal of some, but not all, material on the surface during washing with 0.1 M KCl and by other experiments (data not shown) in which cytochrome *c* adsorbed in submonolayer coverages could not be washed off with 0.1 M KCl. The conformation of the cytochrome *c* is believed to be unchanged upon adsorption to silica as demonstrated in a previous report by Cheng *et al.* [14].

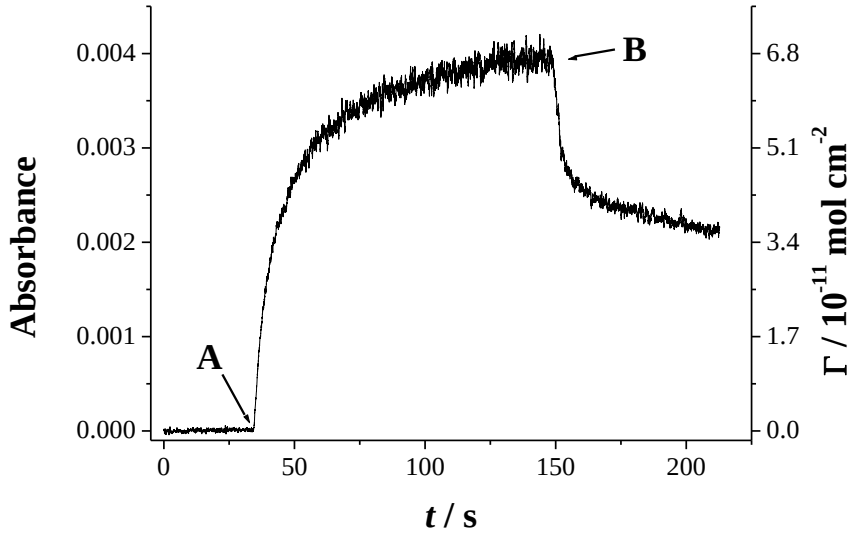

Figure 4.3 The EW-CRDS response to the adsorption of cytochrome *c* to the bare prism surface. At point A, the cytochrome *c* solution is introduced to the prism surface. At point B, the surface is washed with 0.1 M KCl. The second y-ordinate shows the surface coverage calculated from the optical absorbance using the extinction coefficients calculated in Section 4.3.1.

4.3.3 Reduction of cytochrome *c* by $FeEDTA^{2-}$

Once the cytochrome *c* had been adsorbed and the surface washed, the $FeEDTA^{-}$ solution was introduced to the cell. This process had no effect on the ring-down time indicating that the mediator did not reduce the cytochrome nor cause it to desorb from the surface. The Pt working electrode was positioned 100 μm from the prism surface forming

a thin layer cell between the electrode and prism surface. The potential at the electrode was stepped from open circuit to -0.5 V vs. Ag/AgCl for 60 seconds and then returned to open circuit in order to reduce the $FeEDTA^-$ to $FeEDTA^{2-}$. The EW-CRDS signal was recorded simultaneously and a typical response is shown in Figure 4.4. The potential was stepped at $t = 0$ s, which causes the $FeEDTA^-$ at the electrode to be reduced at a diffusion-limited rate. There is then a short lag time in the EW-CRDS response, which is the time required for the $FeEDTA^{2-}$ to diffuse from the working electrode to the prism surface, followed by a reduction in the absorbance due to the $FeEDTA^{2-}$ reducing the cytochrome *c* on the surface. Representative potential and current responses during these chronoamperometry experiments are displayed in Figure 4.5A and Figure 4.5 B, respectively.

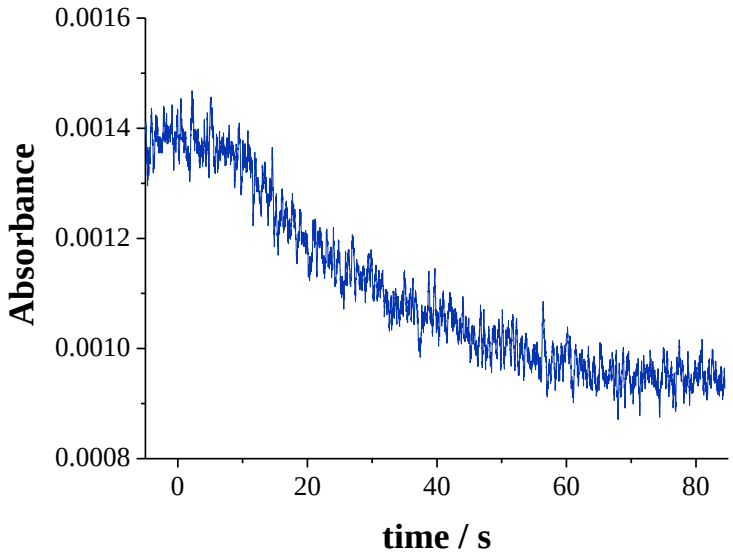

Figure 4.4 A typical EW-CRDS response to a 60 second potential step at the Pt electrode. The $FeEDTA^-$ concentration was 1 mM and the supporting electrolyte was 0.1 M KCl.

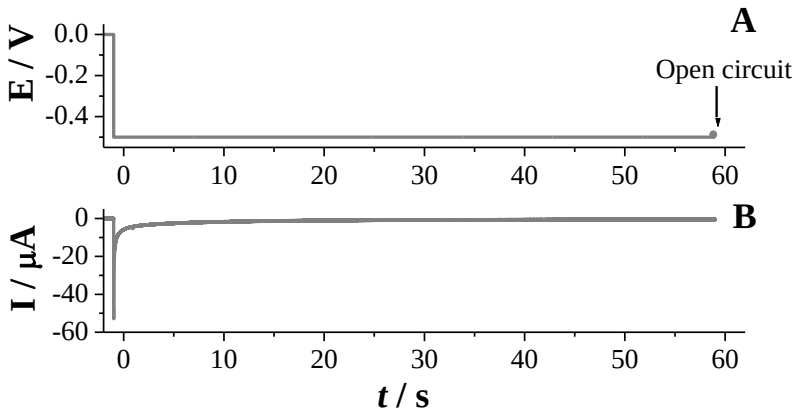

Figure 4.5 The electrode potential and the current response during a 60 second potential step. The $FeEDTA^-$ concentration for this dataset was 1 mM.

The experiment was repeated for three different $FeEDTA^-$ concentrations: 0.5 mM, 0.75 mM and 1 mM. Control experiments in which $FeEDTA^-$ was reduced in the thin layer cell without cytochrome *c* adsorbed to the surface showed no change in the ring-down signal (see Figure 4.6) confirming that any changes in absorbance during experiments with cytochrome *c* bound to the surface must be due to changes in the redox state of the cytochrome. A change in absorbance was not observed during similar experiments probing using a diode laser at λ = 405 nm where the difference in the two spectra of the reduced and oxidised cytochrome *c* was much smaller, indicating that this change was not due to cytochrome *c* desorbing from the surface.

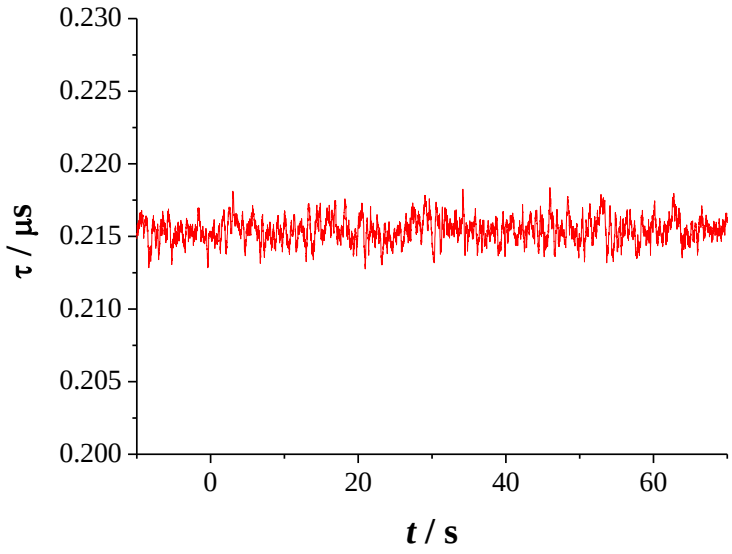

Figure 4.6 The ring-down response to the reduction of FeEDTA$^-$ with no cytochrome *c* adsorbed to the prism surface. The potential was stepped at *t* = 0 s from open circuit to 0.5 V.

It was difficult to obtain exactly the same cytochrome *c* coverage for each experiment, so to compare the EW-CRDS data for different FeEDTA$^-$ concentrations, the ratio of oxidised cytochrome *c* to total cytochrome *c* on the surface, $\theta_O(t)$, is plotted against time for all three concentrations in Figure 4.7. The ratio was calculated using the extinction coefficients of reduced and oxidised cytochrome *c* obtained by UV-visible spectroscopy. Initially all of the surface adsorbed cytochrome *c* is oxidised, and the surface coverage, N, is

$$N = Abs(0) / \varepsilon_{\mathrm{O}} \tag{4.1}$$

where $Abs(0)$ is the initial absorbance. The absorbance at time t, $Abs(t)$ is the sum of absorbance due to oxidised and reduced cytochrome *c*:

$$Abs(t) = N\varepsilon_{\mathrm{O}}\theta_{\mathrm{O}}(t) + N\varepsilon_{\mathrm{R}}\theta_{\mathrm{R}}(t) \tag{4.2}$$

where is $\theta_{\mathrm{R}}(t)$ is the ratio of reduced cytochrome *c* to total cytochrome *c* on the surface.

Substituting $\theta_O(t)+\theta_R(t)=1$ into equation (4.2) we obtain an expression for $\theta_O(t)$:

$$\theta_O(t)=(Abs(t)-N\varepsilon_R)/N(\varepsilon_O-\varepsilon_R) \quad (4.3)$$

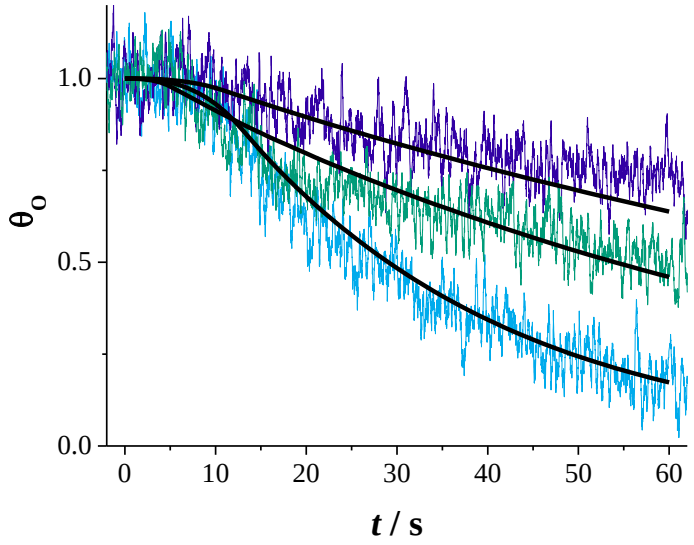

Figure 4.7 The fraction of oxidised cytochrome c on the prism surface with time during a 60 second potential step. The FeEDTA$^-$ concentrations were 0.5 mM (cyan), 0.75 mM (green), 1 mM (navy).

Figure 4.7 shows that for 1 mM FeEDTA$^-$, nearly all of the cytochrome *c* on the surface is reduced by the end of the potential step. As expected, the reduction process proceeds slower for lower concentrations of FeEDTA$^-$ as the effective concentration of FeEDTA^{2-} at the surface is less.

The data in Figure 4.7 were modelled to obtain the rate constant for reduction using a commercially available software package, COMSOL Multiphysics 3.5. The 1D diffusion equation was solved for the concentration of FeEDTA$^-$, c_O, between the electrode and the prism. It was assumed that the diffusion coefficients for the reduced and oxidised form of the mediator were equal so it was unnecessary to model the FeEDTA^{2-} concentration. The boundary condition at the electrode was $c_O=0$. The rate of ET was

potential-dependent set largely by the local ratio of $FeEDTA^-$ to $FeEDTA^{2-}$ as described by Jin and Bethke,[16] and so the boundary condition at the prism surface was:

$$D\frac{\partial c_O}{\partial x} = k_0\left(c^* - c_O\right)\theta_O \exp\left(-\frac{F\Delta E}{2RT}\right) \tag{4.4}$$

$$N\frac{d\theta_O}{dt} = -k_0\left(c^* - c_O\right)\theta_O \exp\left(-\frac{F\Delta E}{2RT}\right) \tag{4.5}$$

where D is the diffusion coefficient of $FeEDTA^-$, N is the surface coverage (in mol cm^2), and k_0 is the intrinsic rate constant (at $\Delta E = 0$) in cm s^{-1}. The potential drop at the interface, ΔE was assumed to be poised by the concentrations of the reduced and oxidised forms of the mediator as has been demonstrated at liquid-liquid interfaces[17] and at conducting polymer films[18] and is assumed to also be the case for electron transfer through the respiratory chain[16]

$$\Delta E = E_{FeEDTA} - E_{cytc} + \frac{RT}{nF}\ln\left(\frac{c_O}{c^* - c_O}\right). \tag{4.6}$$

E_{FeEDTA} is the formal redox potential of the $FeEDTA^{-/2-}$ couple (120 mV vs NHE)[19] and E_{cytc} the formal redox potential of cytochrome *c* (260 mV vs NHE)[8]. The data could not be fit successfully using simpler boundary conditions at the prism surface such as simple second-order rate equations and an Elovich-type equation (as used to fit the data in Chapter 5). The best fits to the data were found by varying k_0, with the optimal found to be 4.0 (± 0.1) $\times 10^{-9}$ cm s^{-1}, 4.0 (± 0.1) $\times 10^{-9}$ cm s^{-1} and 5.0 (± 0.1) $\times 10^{-9}$ cm s^{-1} for $FeEDTA^-$ concentrations of 0.5 mM, 0.75 mM and 1 mM, respectively, giving the mean rate constant of 4.3 (± 0.6) $\times 10^{-9}$ cm s^{-1}. This is equivalent to a second order rate constant of k = 2.7 ± 0.6 M^{-1} s^{-1}, where $k = k_0 \exp(E_{FeEDTA} - E_{cytc})/N$.

The electron transfer rate constant between $FeEDTA^{2-}$ and oxidised cytochrome *c* in solution has been reported to be in the range of 4.10-5.83 × 10^3 M^{-1} s^{-1}, depending on ionic strength and pH [6d, e, 6j, 20]. The comparatively slow electron transfer observed in our experiments is perhaps not unexpected since immobilisation of cytochrome *c* on the silica surface may result in an unfavourable orientation of the heme group due to electrostatic interactions between the positively charged lysine residues surrounding the heme and the negatively charged silica surface. However, the results are interesting in this regard because, as mentioned in the Chapter 1, many biophysical processes involve immobilised proteins. The authors are only aware of one other reported electron transfer rate constant between surface immobilised cytochrome *c* and a solution based mediator. In this report cytochrome *c* was adsorbed to a carboxylic acid-terminated self assembled monolayer on a gold electrode held at a potential sufficient to drive the reduction of the cytochrome *c* layer.[6c] Scanning electrochemical microscopy was used to study the heterogeneous electron transfer between $Fe(CN)_6^{3-}$ generated at an ultramicroelectrode, and the cytochrome *c* at the electrode. The bimolecular electron transfer rate constant was deconvoluted from the observed experimental rate constant and was found to be 2 × 10^4 M^{-1} s^{-1}. It is not surprising that the rate constant is different to ours, because the environment used was quite distinct and because the electrode potential was not considered in the analysis of the data.

4.4 Conclusions

In this chapter, the ability to apply EW-CRDS combined with electrochemical techniques to monitor the redox mediated electrochemistry of surface bound cytochrome

c has been demonstrated. Furthermore, by modelling the thin layer cell arrangement we have obtained the rate constant for the reduction of cytochrome *c* by $FeEDTA^{2-}$. The rate constant was found to be slower than in bulk solution which is not unexpected due to the likelihood of the redox active centre to be oriented unfavourably for electron transfer with the solution-based redox mediator.

The ability to directly monitor electron transfer between surface immobilised proteins and other molecules or proteins, coupled with the ease in which the prism surface can be modified, affords the opportunity of studying electron transfer between biomolecules in a more biologically relevant environment.

4.5 References

1. Gennis, R. B., *Biomembranes : molecular structure and function*. Springer-Verlag: New York, 1989.

2. (a) Gorton, L.; Lindgren, A.; Larsson, T.; Munteanu, F. D.; Ruzgas, T.; Gazaryan, I., Direct electron transfer between heme-containing enzymes and electrodes as basis for third generation biosensors. *Analytica Chimica Acta* **1999,** *400* (1-3), 91-108; (b) Stoica, L.; Ludwig, R.; Haltrich, D.; Gorton, L., Third-generation biosensor for lactose based on newly discovered cellobiose dehydrogenase. *Analytical Chemistry* **2006,** *78* (2), 393-398.

3. (a) Cracknell, J. A.; Vincent, K. A.; Armstrong, F. A., Enzymes as working or inspirational electrocatalysts for fuel cells and electrolysis. *Chemical Reviews* **2008,** *108* (7), 2439-2461; (b) Barton, S. C.; Gallaway, J.; Atanassov, P., Enzymatic biofuel cells for Implantable and microscale devices. *Chemical Reviews* **2004,** *104* (10), 4867-4886; (c) Hambourger, M.; Gervaldo, M.; Svedruzic, D.; King, P. W.; Gust, D.; Ghirardi, M.;

Moore, A. L.; Moore, T. A., FeFe -Hydrogenase-Catalyzed H-2 production in a photoelectrochemical biofuel cell. *Journal of the American Chemical Society* **2008,** *130* (6), 2015-2022; (d) Katz, E.; Willner, I., A biofuel cell with electrochemically switchable and tunable power output. *Journal of the American Chemical Society* **2003,** *125* (22), 6803-6813.

4. Vincent, K. A.; Li, X.; Blanford, C. F.; Belsey, N. A.; Weiner, J. H.; Armstrong, F. A., Enzymatic catalysis on conducting graphite particles. *Nature Chemical Biology* **2007,** *3* (12), 760-761.

5. Pita, M.; Katz, E., Multiple logic gates based on electrically wired surface-reconstituted enzymes. *Journal of the American Chemical Society* **2008,** *130* (1), 36-+.

6. (a) Bansch, B.; Meier, M.; Martinez, P.; Vaneldik, R.; Su, C.; Sun, J.; Isied, S. S.; Wishart, J. F., Mechanistic information from the first volume profile analysis for a reversible intermolecular electron-transfer reaction involving pentaammine(isonicotinamide)ruthenium and cytochrome-*c*. *Inorganic Chemistry* **1994,** *33* (21), 4744-4749; (b) Hodges, J. T.; Looney, J. P.; vanZee, R. D., Response of a ring-down cavity to an arbitrary excitation. *Journal of Chemical Physics* **1996,** *105* (23), 10278-10288; (c) Holt, K. B., Using scanning electrochemical microscopy (SECM) to measure the electron-transfer kinetics of cytochrome *c* immobilized on a COOH-terminated alkanethiol monolayer on a gold electrode. *Langmuir* **2006,** *22* (9), 4298-4304; (d) Holwerda, R. A.; Read, R. A.; Scott, R. A.; Wherland, S.; Gray, H. B.; Millett, F., Electron-transfer reactions of trifluoroacetylated horse heart cytochrome-*c*. *Journal of the American Chemical Society* **1978,** *100* (16), 5028-5033; (e) Macyk, J.; van Eldik, R., Kinetics of the reduction of cytochrome c by Fe-II(EDTA)(H_2O) (2-): outer-sphere vs.

inner-sphere electron transfer mechanisms. *Dalton Transactions* **2003,** (13), 2704-2709; (f) Meier, M.; Sun, J.; Wishart, J. F.; vanEldik, R., Comparative kinetic analysis of reversible intermolecular electron-transfer reactions between a series of pentaammineruthenium complexes and cytochrome *c*. *Inorganic Chemistry* **1996,** *35* (6), 1564-1570; (g) Meier, M.; Van Eldik, R., Volume profile analysis for intermolecular electron-transfer between cytochrome-*c* and Co(terpy)(2)(2+/3+). *Inorganica Chimica Acta* **1994,** *225* (1-2), 95-101; (h) Meier, M.; vanEldik, R., Kinetic and thermodynamic study of the mechanism of reversible intermolecular electron-transfer reactions between horse heart cytochrome *c* and a series of cobalt imine complexes. *Chemistry-a European Journal* **1997,** *3* (1), 39-46; (i) Silvestrini, M. C.; Tordi, M. G.; Colosimo, A.; Antonini, E.; Brunori, M., The Kinetics of Electron-Transfer Between *Pseudomonas-Aeruginosa* Cytochrome C-551 and its Oxidase. *Biochemical Journal* **1982,** *203* (2), 445-451; (j) Wherland, S.; Gray, H. B., Metalloprotein Electron-Transfer Reactions - Analysis of Reactivity of Horse Heart Cytochrome-*c* with Inorganic Complexes. *Proceedings of the National Academy of Sciences of the United States of America* **1976,** *73* (9), 2950-2954.

7. Eddowes, M. J.; Hill, H. A. O., Novel Method for Investigation of Electrochemistry of Metalloproteins - Cytochrome-*c*. *Journal of the Chemical Society-Chemical Communications* **1977,** (21), 771-772.

8. Yeh, P.; Kuwana, T., Reversible Electrode-Reaction Of Cytochrome-*c*. *Chemistry Letters* **1977,** (10), 1145-1148.

9. Bernhardt, P. V., Enzyme Electrochemistry - Biocatalysis on an electrode. *Australian Journal of Chemistry* **2006,** *59* (4), 233-256.

10. Armstrong, F. A., Protein film voltammetry: Revealing the mechanisms of biological oxidation and reduction. *Russian Journal of Electrochemistry* **2002,** *38* (1), 49-62.

11. Leger, C.; Bertrand, P., Direct electrochemistry of redox enzymes as a tool for mechanistic studies. *Chemical Reviews* **2008,** *108* (7), 2379-2438.

12. Armstrong, F. A., Recent developments in dynamic electrochemical studies of adsorbed enzymes and their active sites. *Current Opinion in Chemical Biology* **2005,** *9* (2), 110-117.

13. Friedrich, M. G.; Plum, M. A.; Santonicola, M. G.; Kirste, V. U.; Knoll, W.; Ludwig, B.; Naumann, R. L. C., In situ monitoring of the catalytic activity of cytochrome *c* oxidase in a biomimetic architecture. *Biophysical Journal* **2008,** *95* (3), 1500-1510.

14. Cheng, Y. Y.; Lin, S. H.; Chang, H. C.; Su, M. C., Probing Adsorption, Orientation and Conformational Changes of Cytochrome c on Fused Silica Surfaces with the Soret Bandâ€. *The Journal of Physical Chemistry A* **2003,** *107* (49), 10687.

15. Cheng, Y. Y.; Lin, S. H.; Chang, H. C.; Su, M. C., Probing adsorption, orientation and conformational changes of cytochrome c on fused silica surfaces with the soret band. *Journal of Physical Chemistry A* **2003,** *107* (49), 10687-10694.

16. Jin, Q. S.; Bethke, C. M., Kinetics of electron transfer through the respiratory chain. *Biophysical Journal* **2002,** *83* (4), 1797-1808.

17. Solomon, T.; Bard, A. J., Reverse (uphill) electron-transfer at the liquid/liquid interface. *Journal of Physical Chemistry* **1995,** *99* (49), 17487-17489.

18. Whitworth, A. L.; Mandler, D.; Unwin, P. R., Theory of scanning electrochemical microscopy (SECM) as a probe of surface conductivity. *Physical Chemistry Chemical Physics* **2005,** *7* (2), 356-365.

19. Kolthoff, I. M.; Auerbach, C., Studies on the System Iron-Ethylenediamine Tetraacetate1. *Journal of the American Chemical Society* **1952,** *74* (6), 1452-1456.

20. Hodges, H. L.; Holwerda, R. A.; Gray, H. B., Kinetic studies of reduction of ferricytochrome-*c* by Fe(EDTA)2. *Journal of the American Chemical Society* **1974,** *96* (10), 3132-3137.

Chapter 5. Kinetics of Porphyrin Adsorption and DNA-Assisted Desorption at the Silica-Water Interface

This chapter describes the application of EW-CRDS to study *in situ* the kinetics of the adsorption of 5,10,15,20-tetrakis(4-N-methylpyridiniumyl)porphyrin (TMPyP) from pH 7.4 phosphate buffer solution (PBS) to the silica–water interface and the interaction of calf thymus DNA (CT-DNA) with the resulting TMPyP-functionalised surface. TMPyP was delivered to the silica surface using an impinging jet technique (as outlined in Section 2.2) to allow relatively fast surface kinetics to be accessed. Adsorption was first-order in TMPyP and the initial adsorption rate constant at the bare surface was found to be $= 4.1 (\pm 0.6) \times 10^{-2}$ cm s^{-1}. A deceleration in the adsorption kinetics was observed at longer times that could be described semi-quantitatively using an Elovich-type kinetic expression. The limiting value of the absorbance corresponded approximately to monolayer coverage (6.2×10^{13} molecules cm^{-2}). Exposure of the TMPyP-modified silica surface to CT-DNA, achieved by flowing CT-DNA solution over the functionalised surface, resulted in efficient desorption of the TMPyP. The desorption process was driven by the interaction of TMPyP with CT-DNA, which UV-visible spectroscopy indicated involved intercalative binding. The desorption kinetics were also simulated using complementary finite element modelling of convection-diffusion coupled to a surface process.

5.1 Introduction

Porphyrins are heterocyclic organic rings containing four pyrrole subunits linked via methine bridges. They have been investigated extensively in various fields, for example, as potent anti-viral and anti-tumor therapeutic agents,[1] for specific sensing of DNA sequences,[2] and as photosensitisers in artificial solar energy systems.[3] These, and other applications, arise because porphyrins exhibit strong absorption bands in the visible region, possess interesting non-linear optical properties,[4] are relatively easy to synthesise, and their physicochemical properties can be tuned through careful choice of peripheral substituents and inserted metal ions.[5]

In the past decade, the interest in supramolecular interactions of water-soluble cationic porphyrins like 5,10,15,20-tetra(N-methylpyridinium-4-yl)porphyrin (TMPyP, see Figure 5.1 for chemical structure) with biological molecules has increased steadily, as a consequence of the desire to understand the structure and functions of biomacromolecules.[5-6] The binding of water-soluble porphyrins to nucleic acids has been studied in solution with a variety of spectroscopic methods, including resonance Raman (RR),[7] UV-visible spectroscopy, circular dichroism (CD),[8] and fluorescence.[9] Resonance light scattering (RLS) spectra have also been reported.[10] There have been relatively few studies investigating the binding behavior at surfaces. Lei *et al.*[11] determined the rate constant for the binding of FeTMPyP to a surface-immobilised Salmon testis double stranded DNA-polymer film using a quartz crystal microbalance. Naue *et al.*[12] studied the binding of a tetrapyridylporphyrin to surface-bound CT-DNA using surface plasmon resonance (SPR).

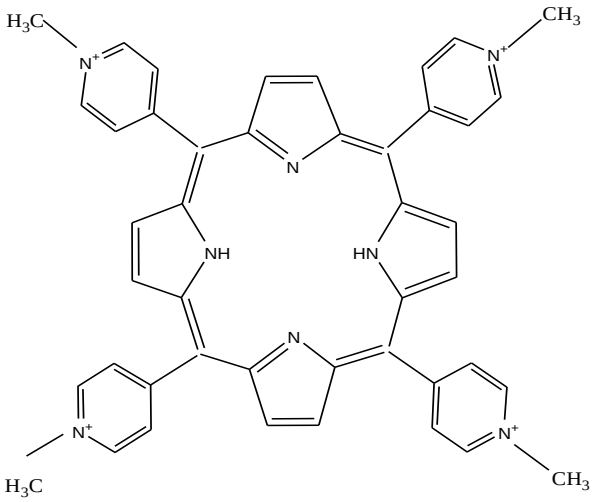

Figure 5.1 Chemical structure of TMPyP.

5.2 Experimental

5.2.1 Materials

All chemicals were used as received. These were: sodium phosphate dibasic (SigmaUltra, minimum 99.0%, Sigma-Aldrich); sodium phosphate monobasic monohydrate (98.0-102.0% from Sigma-Aldrich); methyl alcohol (99.9% from Acros); poly-L-lysine hydrobromide (mol wt 30,000-70,000 from Sigma); sodium chloride (99+ % from Aldrich). Ultrapure water was obtained from a Milli-Q plus 185 system from Millipore (resistivity of 18.2 MΩ cm at 25ºC).

5,10,15,20-Tetrakis(1-methyl-4-pyridinio)porphyrin tetra (*p*-toluenesulfonate) (TMPyP·TTS) was purchased from Fluka (BioChemika, for fluorescence, ≥ 95% (N)) and used without further purification. Porphyrin stock solution was made by dissolving the solid TMPyP·TTS in phosphate buffer solution (PBS, 1mM, pH 7.4.) and the resulting solution was stored at 4ºC in the dark to prevent photodegradation.

Concentrations of the TMPyP solutions were determined via spectrophotometry at a wavelength of 422 nm, using an extinction coefficient, ε_{422} of 2.26×10^5 M^{-1} cm^{-1}.[13]

Deoxyribonucleic acid (DNA) sodium salt from calf thymus (CT) was obtained from Sigma (Type I fibers). This highly polymerised DNA (prepared from male and female calf thymus tissue) contains both double stranded and single stranded forms. The single-to-double stranded DNA ratio in PBS was determined to be 19:81 by the analysis of the experimental DNA melting curve (data not shown). The molecular weight was stated to be between 10-15 million daltons. DNA from calf thymus is 41.9 mole % Guanine-Cytosine and 58.1 mole % Adenine-Thymine.[14] To prepare the CT-DNA stock solution, CT-DNA was dissolved in PBS at 4ºC for 48 h with occasional stirring to ensure the formation of a homogenous solution. Concentrations, expressed in moles of base pairs per litre, were deduced spectrophotometrically using an $\varepsilon_{260} = 1.32 \times 10^4$ M^{-1} cm^{-1} for CT-DNA.[15]

In all experiments, the porphyrin and DNA solutions were freshly prepared from stock solutions before spectral analysis and were protected from light until they were added into the cell compartments. All measurements were taken at room temperature (20 ± 1°C). The EW-CRDS set-up with flow was used as outlined in Section 2.1.

5.3 Simulation and Modelling

5.3.1 TMPyP Adsorption Kinetics

The axially symmetric geometry for the fluid flow problem is shown in Figure 5.2. In order to obtain the velocities, u and v, in the r and z directions, respectively, the

time-independent incompressible Navier-Stokes equation was solved at each mesh point in the domain shown in Figure 5.2. No-slip boundary conditions were applied to the walls of the pipe and the silica surface, and the following boundary conditions applied at the inlet of the pipe:

$$u = 0, v = \frac{2v_f}{\pi r_{in}^2}\left(1 - \frac{r^2}{r_{in}^2}\right) \quad z = H, \quad 0 \le r \le r_{in} \tag{5.1}$$

where v_f is the flow rate in $m^3\ s^{-1}$ and r_{in} is the pipe inner radius. There was assumed to be no pressure at the outlet ($r = r_{out}, 0 \le z \le d$). The use of equation (5.1) assumes fully-developed laminar (Poiseuille) flow in the pipe (before the outlet) and is reasonable for the flow rates and the nozzle used (diameter 2 mm; length 5 cm).

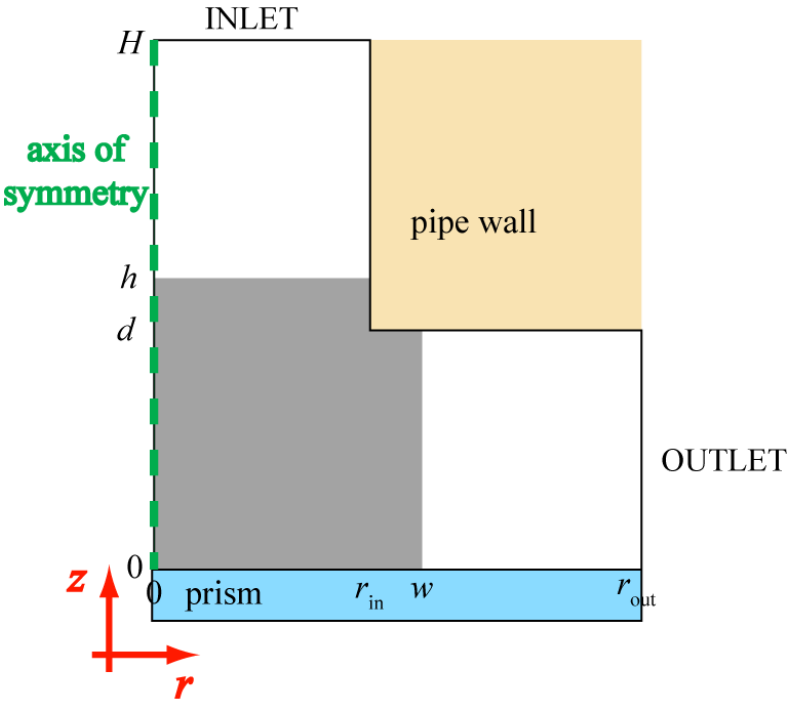

Figure 5.2 Geometry used for simulating adsorption and desorption using the pipe-flow system.

The solution of the convection-diffusion equation for the concentration of porphyrin, c_p, in the adsorption model was obtained in the subdomain shaded in grey in Figure 5.2. No-flux boundary conditions were applied to the pipe walls and a convective flux boundary condition was applied to the outlet ($r = w, 0 \le z \le d$). The boundary condition at the solution inlet ($z = h, 0 \le r \le r_{in}$) was that the solution concentration was equal to that of bulk, $c_p = c_p^*$.

Polarisation dependent EW-CRDS, performed in a folded cavity arrangement by Simon Neil in Oxford did not determine any preferred orientation for surface adsorbed porphyrin molecules under similar conditions to those used here (see Section 5.4.4). In addition, since there are also likely to be significant surface-coverage dependent adsorbate-adsorbate interactions as well as surface potential effects from the charged interface and charged adsorbate,[16] we use an Elovich-type equation to model the adsorption process which can be considered to incorporate these various factors in a semi-empirical manner. The Elovich equation has proven successful in describing the kinetics of a wealth of adsorption and desorption processes,[17] including adsorption at heterogeneous surfaces[18] and the desorption of ions from soil samples.[19] The boundary condition at the prism surface for the adsorption model was:

$$D_p \frac{\partial c_p}{\partial z} = -k c_p (1-\theta) e^{-\lambda\theta} \qquad (5.2)$$

$$N \frac{d\theta}{dt} = k c_p (1-\theta) e^{-\lambda\theta}, \qquad (5.3)$$

where D_p is the diffusion coefficient of porphyrin in solution, θ is the fractional surface coverage of porphyrin, N is monolayer surface coverage of porphyrin, λ is a factor

describing the change in the apparent adsorption rate coefficient with surface coverage (for $\theta = 0$) and k is the initial adsorption rate constant. The initial conditions were $\theta = 0$ and $c_p = c_p^*$. The adoption of an irreversible adsorption model was justified by the fact that silica surfaces modified by TMPyP could be rinsed with water with negligible detectable desorption (as evidenced by EW-CRDS).

5.3.2 Modelling DNA-Assisted TMPyP Desorption

To obtain the rate constant for DNA-assisted TMPyP desorption from the silica surface, a similar model to that described above was adopted, except that the convection-diffusion equation was solved for the concentration of DNA base pairs in solution, c_{bp}, and the boundary condition at the prism surface was changed to describe the removal of porphyrin from the prism surface by CT-DNA. For similar reasons as for the model above, the following Elovich-type boundary condition was applied at the prism surface:

$$D_{DNA} \frac{\partial c_{bp}}{\partial z} = -k' c_{bp} N \theta e^{\lambda' \theta} \tag{5.4}$$

$$\frac{d\theta}{dt} = -k' c_{bp} \theta e^{\lambda' \theta} \tag{5.5}$$

where D_{DNA} is the diffusion coefficient of the CT-DNA (calculated to be 1.2×10^{-8} cm^2 s^{-1} according to the literature[57]), λ' is a parameter which defines the surface-coverage dependence of the desorption coefficient value, and k' is the desorption constant. The parameters N and θ again refer to the coverage of the silica surface by TMPyP. The initial conditions were $\theta = 1$ and $c_{bp} = c_{bp}^*$.

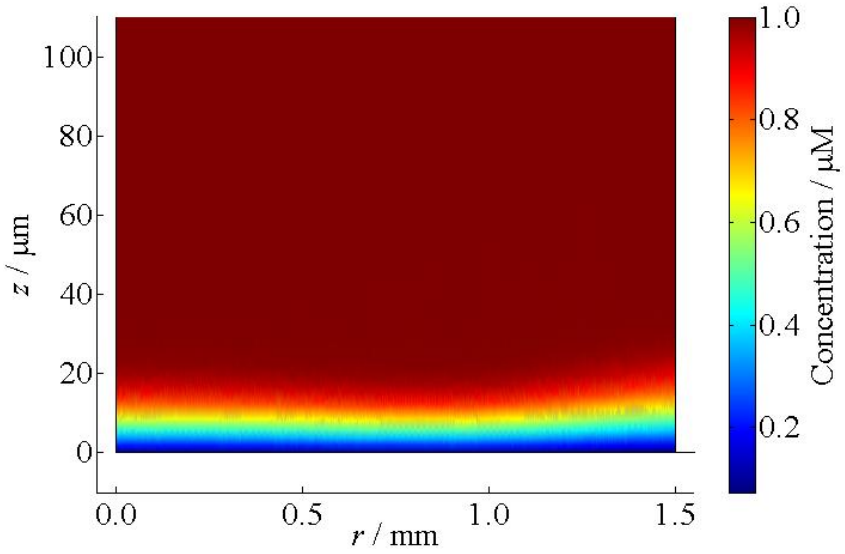

Figure 5.3 Velocity profile from the simulation with a flow rate of 5 mL min^{-1}.

An example flow profile and a concentration profile derived from these simulations are shown in Figure 5.3 and Figure 5.4, respectively, after 1 s for a flow rate of 5 mL min^{-1} and nozzle-to-prism separation of 500 μm for the TMPyP adsorption process, with [TMPyP] = 1 μM and k = 0.035 cm s^{-1}. Note that since the nozzle outer diameter is larger than the footprint of the laser at the TIR interface, we assume the flux profile in the region probed by EW-CRDS is fairly uniform. This was a deliberate consequence of the nozzle design, which was such that the stagnation zone of the impinging jet was probed where mass transport to the interface was uniform.[20]

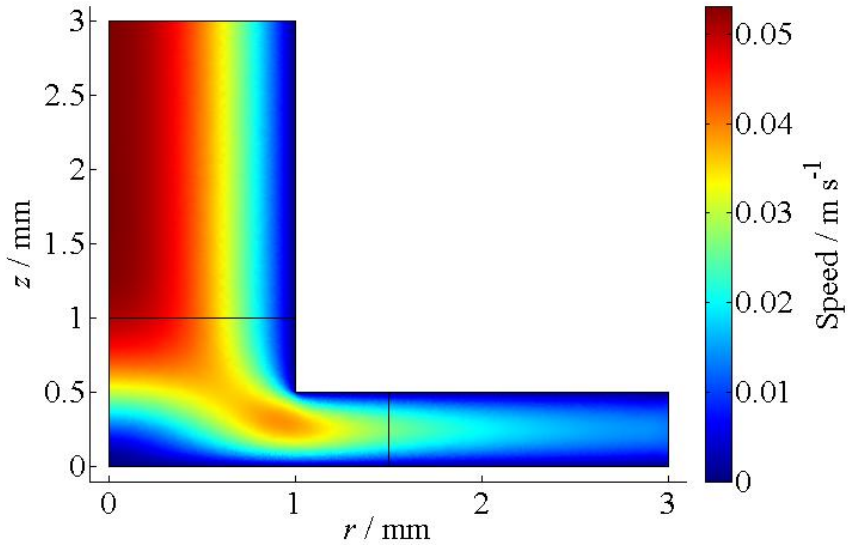

Figure 5.4 Typical concentration profile from the simulation for a porphyrin concentration of 1 μM, k = 0.0035 cm s^{-1} and λ = 3 after 1 second.

5.4 Results and Discussion

5.4.1 Solution Properties of TMPyP, CT-DNA and the TMPyP-(CT-DNA) Complex

UV-visible spectroscopy was employed to identify the solution properties of TMPyP and related complexes. Optical absorption spectra were recorded over the wavelength range 350-800 nm for TMPyP for concentrations between 5×10^{-7} and 1×10^{-5} M in 1 mM PBS at pH 7.4 (Figure 5.5). The Soret band appears at 422 nm and the maximum obeyed the Beer-Lambert law (Figure 5.5 insert) in that there was no deviation from linearity, which indicates that there was no self-aggregation of the porphyrin. From the slope of the inset in Figure 5.5, the extinction coefficient of TMPyP was determined to be $\varepsilon_{422\ nm} = 2.26 \times 10^5$ M^{-1} cm^{-1} in agreement with previous findings.[13] The extinction

coefficients and positions of the other four peaks were also in agreement with the literature indicating the purity of the sample.[13]

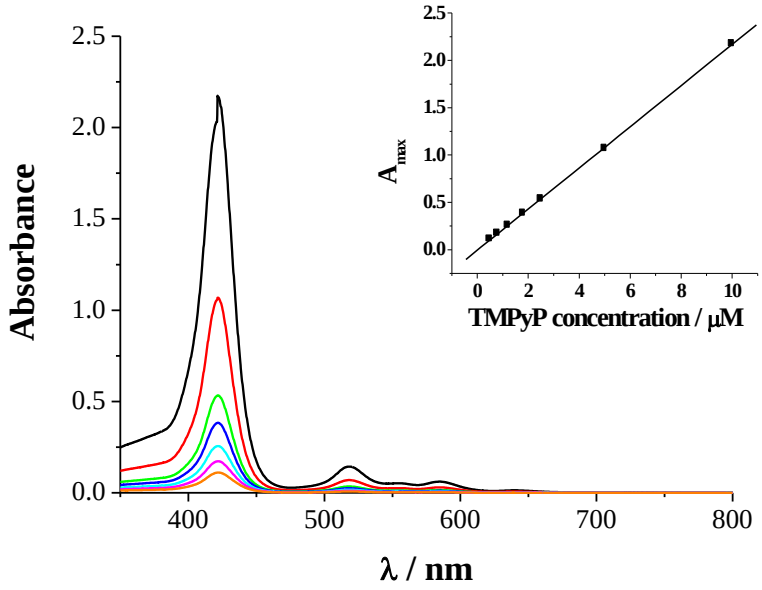

Figure 5.5 UV-visible spectra of TMPyP at different concentrations in 1 mM PBS at pH 7.4: 10 μM (black), 5 μM (red), 2.5 μM (green), 1.8 μM (blue), 1.2 μM (cyan), 0.8 μM (magenta), 0.5 μM (orange). The inset is the absorbance at the Soret band as a function of TMPyP concentration.

The purity of DNA samples is commonly assessed by comparing the ratio of the optical absorbances at 260 nm and 280 nm.[21] A CT-DNA solution of 0.05 mg mL^{-1} in 1 mM PBS gave a ratio of 1.84:1 (see Figure 5.6), indicating there was no protein contamination. The base pair concentration of CT-DNA was determined to be 5.5×10^{-5} M from absorbance measurements using $\varepsilon = 1.32 \times 10^4$ M^{-1} cm^{-1} at the maximum near 260 nm.[44] Assuming a molecular weight of $1 - 1.5 \times 10^7$ g mol^{-1} (11-16.5 kbp), the molecular concentration of CT-DNA in this solution was calculated to be 3.3 – 5 nM.

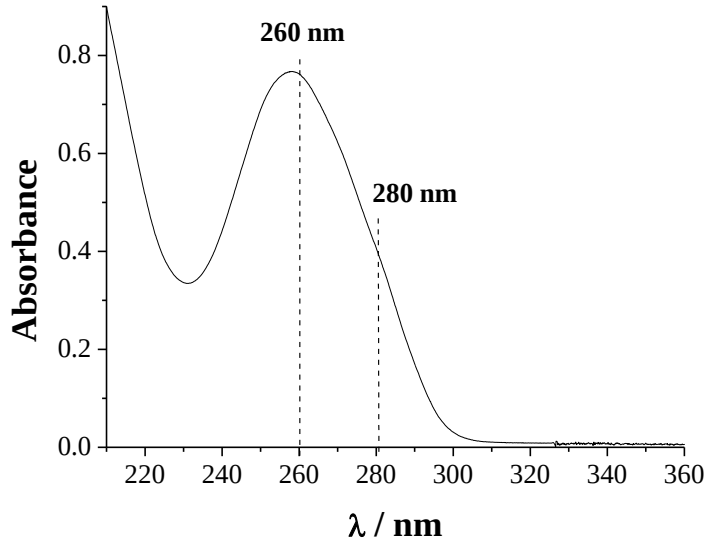

Figure 5.6 The absorbance of CT-DNA in 0.05 mg mL^{-1} in 1 mM PBS at pH 7.4.

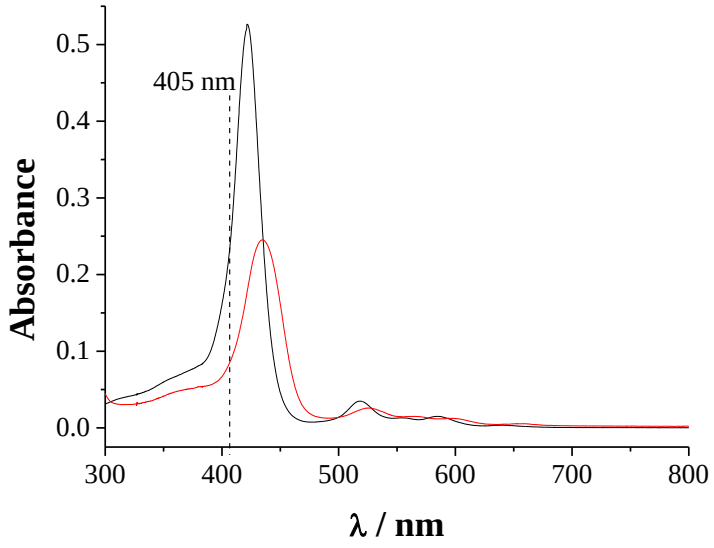

Figure 5.7 Absorption spectra of 2.5 μM TMPyP without (black) and with (red) 0.025 mg mL^{-1} CT-DNA in 1 mM PBS at pH 7.4.

The absorption spectra of 2.5 μM TMPyP without (black line) and with (red line) 0.025 mg mL^{-1} CT-DNA (2.8×10^{-5} M base pairs concentration) are shown in Figure 5.7. This is a sufficient excess of DNA to complex all of the available porphyrin under these conditions as was demonstrated by spectrophotometric titration (see Figure 5.8). To ensure that the TMPyP-(CT-DNA) system was at equilibrium, the spectrum was collected 5 min after adding the CT-DNA solution and was found to be time-invariant on longer time scales. The formation of the TMPyP-(CT-DNA) complex produces a 13 nm bathochromic shift of the Soret maximum from 422 nm to 435 nm and a hypochromic effect of 53 %. This is consistent with intercalation of the porphyrin into the DNA base pairs.[8, 22] DNA groove binding is typically characterised by no (or minor) changes of the UV-vis spectrum and outside binding to DNA is accompanied by a red shift in the Soret band , $\Delta\lambda \leq 8$ nm and weak hypochromism (typically $\Delta H \leq 10$ % of the Soret band). For intercalation of TMPyP with CT-DNA, the hydrophobic effect, the van der Waals interactions with the DNA bases, and coulombic interactions — involving the positively charged pyridiniumyl substituents — all promote uptake.[3a] From the spectrum in Figure 5.7, the extinction coefficient ε_{435} of the TMPyP-(CT-DNA) complex was calculated to be 9.81×10^4 M^{-1} cm^{-1}. Finally, it is also clear from Figure 5.7 that at 405 nm (the wavelength for EW-CRDS measurements) there is a decrease by a factor of 3.35 in the absorbance of porphyrin upon DNA-complexation.

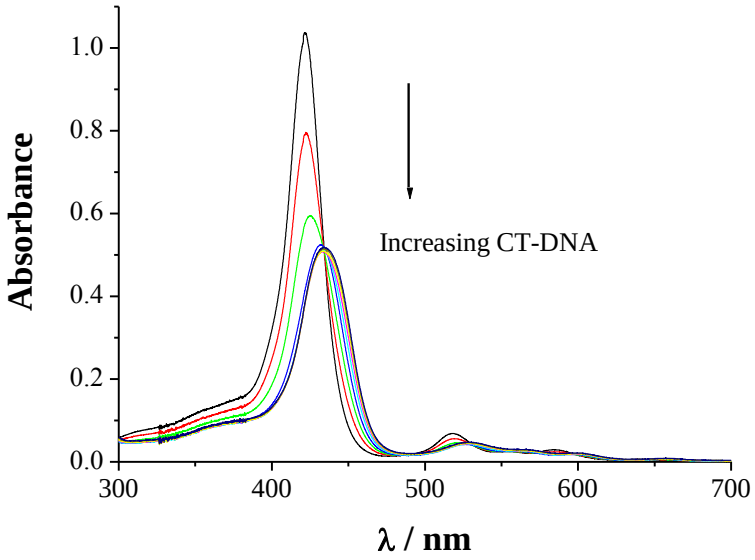

Figure 5.8 Spectrophotometric titration of 5 μM TMPyP with increasing CT-DNA concentrations from 0 mg mL^{-1} to 0.014 mg mL^{-1}.

5.4.2 EW-CRDS Bulk Absorbance Measurements

To calculate the absorbance measured by EW-CRDS due to TMPyP in the bulk, the EW-CRDS signal was measured with a positively-charged film on the prism surface to prevent adsorption (similar to the experiments described in Section 3.3.2). As explained in Section 2.3, in order to determine the absorbance due to surface adsorbed species, A_s (and thus the surface concentration of adsorbed porphryin), from the EW-CRDS signal it was necessary to subtract the bulk absorbance, A_b. To obtain A_b the EW-CRDS signal was recorded for a solution of 7.38 μM TMPyP in 1 mM PBS (pH 7.4) on a PLL-modified surface (the background ring-down time in this case was with 1 mM PBS with a PLL-modified prism). The TMPyP was expected not to adsorb to the PLL as a result of the strong electrostatic repulsion between the positively-charged porphyrin

molecules and the positively-charged surface. This was confirmed by the morphology of the EW-CRDS transients, as shown in our previous work and in Figure 3.4.[23] The bulk absorbance of 7.38 μM TMPyP was 4.9×10^{-4}. The optical absorbance of TMPyP bulk solution followed the Beer-Lambert law, so all other bulk absorbances could be calculated accordingly, allowing A_s to be determined in subsequent measurements.

5.4.3 Adsorption of TMPyP to Silica Surfaces

Initial studies of the effect of NaCl on the adsorption of 1.2 μM TMPyP to silica (glass vial) surfaces from PBS (1mM, pH 7.4) were carried out using UV-visible spectroscopy. For the results summarised in Figure 5.9, all spectroscopic measurements were taken within 2 min of solution preparation in a glass vial and then transferred to a quartz cuvette. Even so, a strong electrolyte effect on the magnitude of the absorbance is evident, which can be attributed to different degrees of porphyrin adsorption from solution to the glass vial surface. As can be seen from the inset of Figure 5.9, as the ionic strength increases, the TMPyP Soret band absorbance increases, as Na^+ effectively competes with TMPyP to adsorb on the vial surface and the concentration of TMPyP in solution does not change.

UV-vis absorption spectra of 1.2 μM TMPyP (1 mM PBS, pH 7.4) were measured at three different time scales (2 min, 3 h and 70 h) for 0 mM, 50 mM and 200 mM NaCl. The relative absorbance at the Soret band for these spectra are displayed in Figure 5.10. As the time increases from 2 min to 70 h, the absorbance of TMPyP dramatically decreases for each of the three different NaCl solutions, again showing that the adsorption of TMPyP to the silica (glass vial) surface can be effectively inhibited by increasing the concentrations of NaCl in solution.

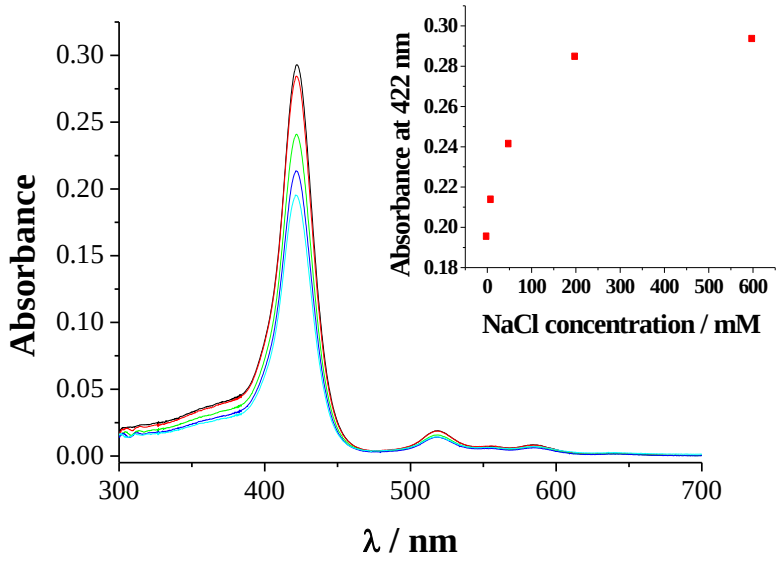

Figure 5.9 The effect of NaCl concentration on TMPyP adsorption. The UV-visible absorption spectra of 1.2 μM TMPyP in PBS (1mM, pH 7.4) stored in a glass vial for 2 minutes with different NaCl concentrations: 600 mM (black), 200 mM (red), 50 mM (green), 10 mM (blue), 0 mM (cyan). The inset shows the dependence of the absorbance at 422 nm on the NaCl concentration.

To complement the above experiments, the effect of ionic strength on the adsorption of 1.2 μM TMPyP (1 mM PBS, pH 7.4) to silica prism surface was also followed *in situ* by EW-CRDS. To this end solutions of TMPyP in different NaCl concentrations were dropped onto the prism surface and the EW-CRDS response monitored in real time (see Figure 5.11). Adsorption of TMPyP was clearly inhibited by the presence of NaCl. With salt concentrations much higher than those of TMPyP (≥ 50 mM NaCl), competitive binding between the TMPyP cation and Na^+ occurs, resulting in a lower concentration of surface-adsorbed TMPyP and thus a lower value of A_s. These data are qualitatively consistent with the UV-visible absorption data in Figure 5.9, but in Figure 5.11, the

interfacial adsorption of TMPyP is measured *directly*, *in situ* and in *real time* (see second y-ordinate).

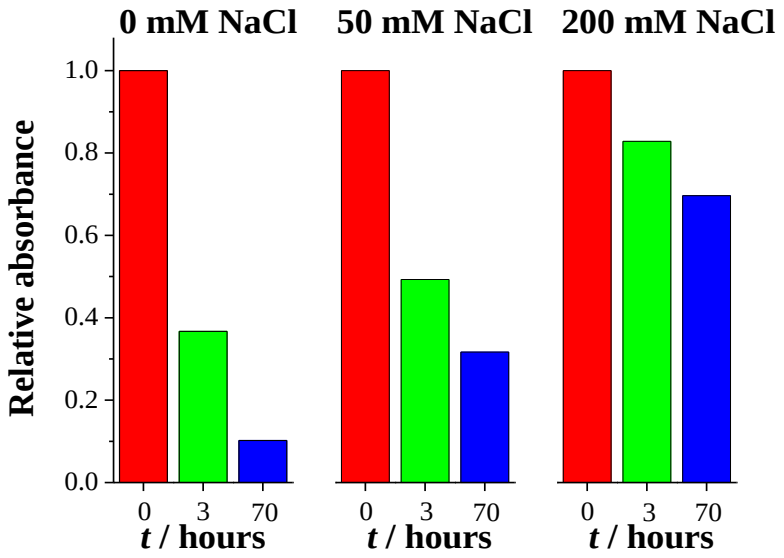

Figure 5.10 Competitive binding of TMPyP and Na^+ to a glass vial as a function of time and NaCl concentration.

The formation of a monolayer of TMPyP on the silica surface is controlled by the assembly of the individual TMPyP units in response to the surface charge and the ionic strength of the bulk solution. The silica has a surface potential at pH 7.4 of the order -75 mV.[24] This potential arises from the dissociation of the silanol groups on the silica surface which leaves the surface partially charged. There are two types of groups with pK_a of 4.5 and 8.5.[25] At pH 7.4, 99.7% of [−SiOH] groups are deprotonated in solution, giving a $-SiO^-$ surface density of ~ 0.93 nm^{-2} and hence a surface charge density of ~ 0.93 e nm^{-2}. TMPyP adsorption takes place onto this surface but Na^+ can compete to bind at these deprotonated sites.

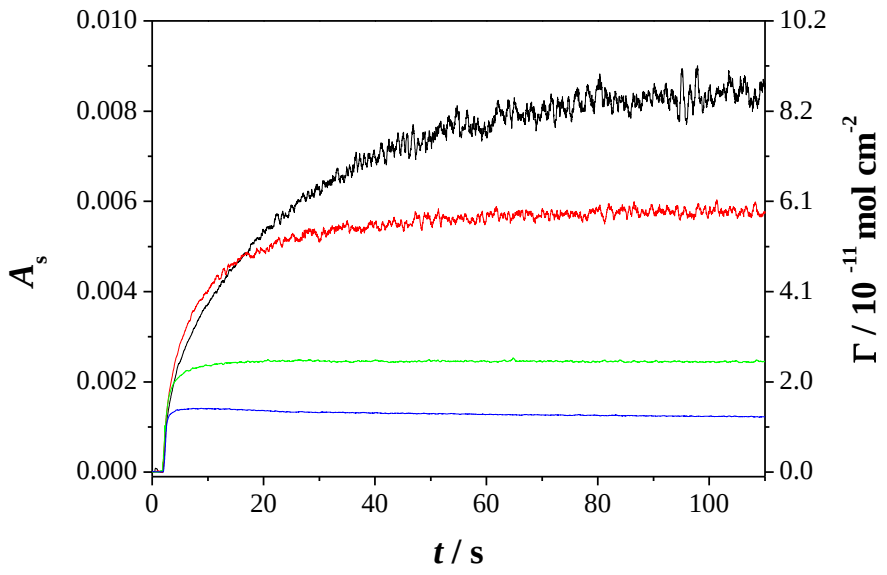

Figure 5.11 EW-CRDS signal for 1.2 μM TMPyP adsorption to silica at various NaCl concentrations in buffer (1 mM PBS, pH 7.4). The NaCl concentrations were 0 mM (black), 50 mM (green), 200 mM (red), 600 mM (blue).

5.4.4 Monitoring TMPyP Adsorption Using EW-CRDS

Initial EW-CRDS experiments to monitor the adsorption of TMPyP to the silica surface involved simply dropping solutions of TMPyP onto the prism surface. The effect of different TMPyP concentrations is shown in Figure 5.12. For all concentrations of TMPyP studied, the absorbance value tends to 0.009 indicating that the adsorption is irreversible. Using the extinction coefficient of TMPyP at 405 nm ($\varepsilon_{405\ nm}$ = 8.71 ×10^4 M^{-1} cm^{-1}), this corresponds to a surface concentration of 6.2 × 10^{13} molecules cm^{-2}, which is in good agreement with a previous report.[26] As expected, the greater the TMPyP concentration in solution the faster the adsorption proceeds. Although this data makes sense qualitatively, as the TMPyP solutions were pipetted onto the prism surface and not

delivered in a well-defined way, it was not possible to model this data to obtain the adsorption rate constant. In order to do this, further experiments were performed in which the flow-cell system described in Section 2.2 was employed to deliver solution to the prism surface.

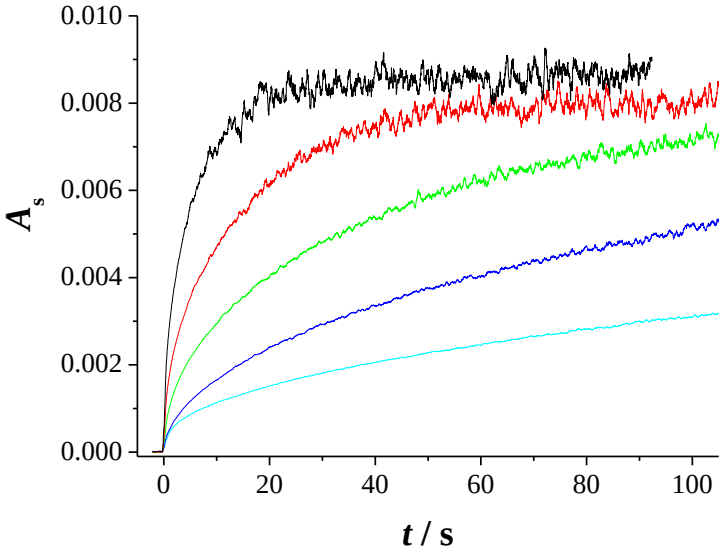

Figure 5.12 EW-CRDS response to the exposure of the prism surface to TMPyP in 1 mM PBS (pH 7.4). The solutions were simply dropped onto the prism using a pipette. The TMPyP concentrations were 2.5 μM (black), 1.8 μM (red), 1.2 μM (green), 0.8 μM (blue) and 0.5 μM (cyan).

Polarisation-dependent EW-CRDS measurements were carried out by Simon Neil at the Physical and Theoretical Chemistry Laboratory at Oxford University to determine whether the TMPyP adsorbed in a preferred orientation and whether this changed with TMPyP surface coverage as has been previously reported.[26] Figure 5.13 shows the polarisation-dependent EW-CRDS response to the adsorption of 0.5 μM TMPyP in 1 mM PBS (pH 7.4). The absorbance plateaus after 150 seconds indicating that monolayer coverage is achieved. The absorbance transients shown in Figure 5.13 B agree qualitatively with the data in Figure 5.12 for TMPyP adsorption.

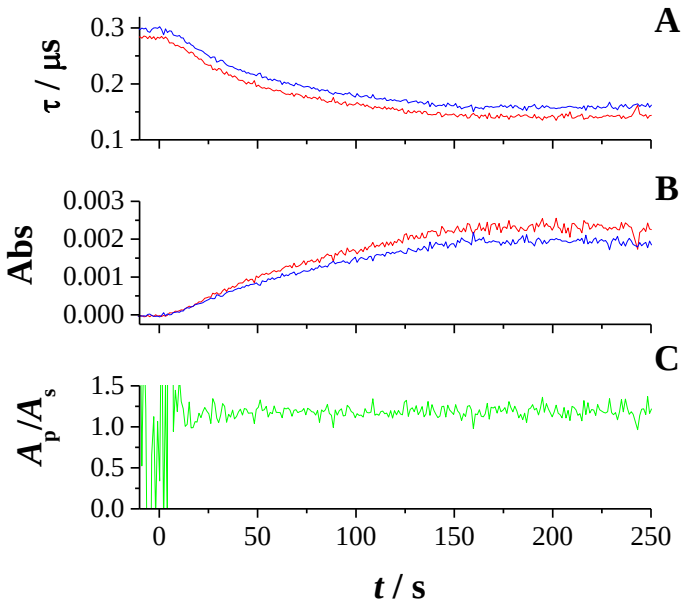

Figure 5.13 Data from a typical polarisation-dependent EW-CRDS measurement. At *t* = 0 seconds 0.5 μM TMPyP in 1 mM PBS (pH 7.4) was introduced to the prism surface. A) The change in ring-down time with time for the *p*-polarised component (red) and the *s*-polarised component (blue). B) The time-dependent absorbances in the p-polarised component (red) and s-polarised component (blue). C) The dichroic ratio, A_p/A_s as a function of time.

The dichroic ratio, A_p / A_s, during both the adsorption and DNA-assisted desorption processes is displayed in Figure 5.13 C. Within experimental error, the ratio does not deviate from 1.18 which indicates that the TMPyP at the prism surface is oriented randomly even when the surface concentration approaches monolayer coverage. At a surface concentration of 6.2×10^{13} molecules cm^{-2}, each molecule occupies approximately 1.6 nm^2. According to Bos *et al.*,[26] in a compact monolayer in which molecules are adsorbed with the TMPyP adsorbed perpendicular to the surface, each molecule would occupy 0.8 nm^2, and if all the molecules were adsorbed lying flat, each

molecule would occupy 2 nm^2. Therefore, in our experiments, the TMPyP molecules have enough space to adopt a wide range of orientations on the surface.

5.4.5 Kinetics of TMPyP Adsorption

To investigate the kinetics of porphyrin adsorption from solution (1 mM PBS pH 7.4) to the silica – water interface, EW-CRDS combined with the flow cell system described in Section 2.2 was used to monitor *in situ* the absorbance signal. The solution was introduced from the nozzle to the surface at a volume flow rate of 5 mL min^{-1} so that the rapid adsorption process could be captured. Figure 5.14 shows the absorbance due to surface adsorbed TMPyP for different concentrations of the bulk solution. As the concentration of TMPyP in solution increases from 0.5 µM to 2.9 µM, the adsorption rate increases markedly. For the larger concentrations, following a rapid initial increase, the TMPyP adsorption reaches a plateau within *ca*. 20 s at which point the silica surface is saturated with TMPyP. The surface concentration of TMPyP (right hand axis in Figure 5.14) can be obtained using the extinction coefficient at 405 nm (ε_{405nm} = 8.71 ×10^4 M^{-1} cm^{-1}), and the limiting value of the optical absorbance (~0.0090) corresponds approximately to full monolayer coverage (6.2 × 10^{13} molecules/cm^2). The data in this figure is noisy at absorbances of around 0.009 due to deterioration of the anti-reflective coatings on the prisms used for these kinetic runs decreasing the background ring-down time to around 320 ns, limiting the maximum optical absorbance that can be measured. Despite this, the limiting monolayer coverage of 0.009 was consistent with the EW-CRDS experiments performed on better quality prisms where TMPyP was simply dropped onto the prism (see Section 5.4.4) surface rather than delivered using the impinging jet flow-cell, and previous reports.[26] The charge on TMPyP (4+, see Figure

5.1) prevents a second layer of molecules depositing on the first. In addition, the tetraphenyl moieties may prevent the stacking of TMPyP for multilayer adsorption. The initial adsorption rate constant for the attachment of TMPyP to a clean silica surface was k = 4.1 (± 0.6) × 10^{-2} cm s^{-1} and the whole data set could be modelled satisfactorily for all surface coverages, and solution concentrations with the Elovich model described in Section 5.3.1 with λ = 3.

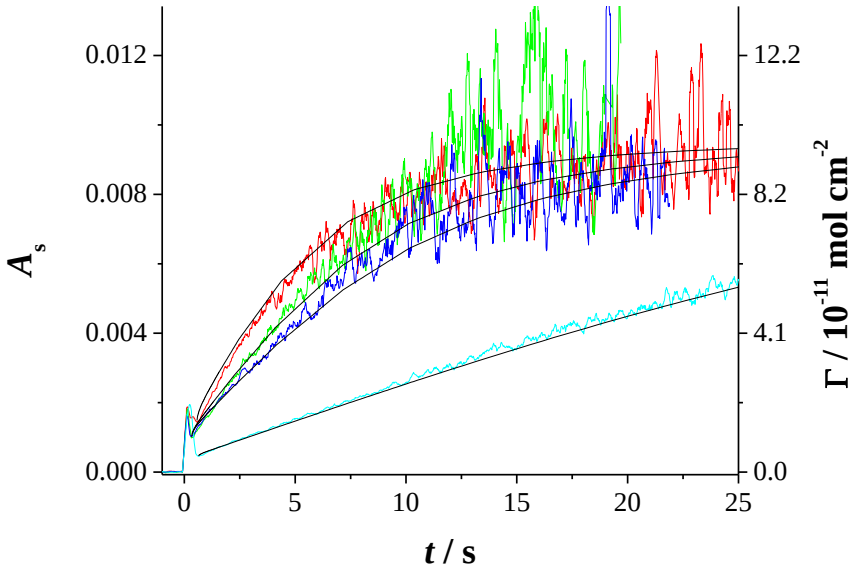

Figure 5.14 Typical EW-CRDS optical absorbance (and equivalent surface concentration) transients and simulations for TMPyP at the silica – water interface at different concentrations in 1 mM PBS (pH 7.4): 2.9 μM (red), 2.0 μM (green), 1.6 μM (blue), 0.5 μM (cyan). The data have been analysed using the model outlined with k = 4.1 (± 0.6) × 10^{-2} cm s^{-1} and λ = 3. The flow rate was 5 mL min^{-1} and the nozzle-prism separation was 500 μm.

To illustrate the sensitivity of the modelling to *k*, Figure 5.15 shows the data for 2.9 μM TMPyP adsorption with different *k* demonstrating that the kinetics can be resolved – i.e., the response is not simply mass transport controlled. The red line is the best fit to the

data with k = 0.05 cm s^{-1} (λ = 3). The blue line shows the results of the simulation for k = 0.07 cm s^{-1} and λ = 3. The model was equally sensitive to the parameter λ.

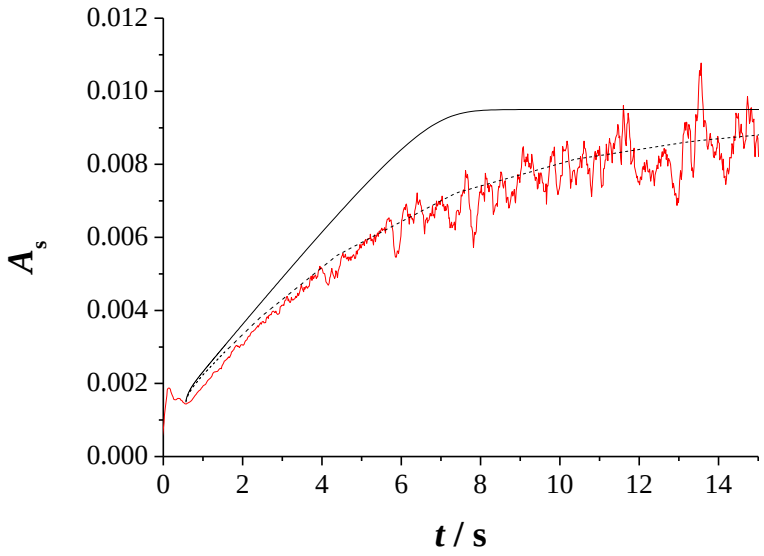

Figure 5.15 Data for 2.9 μM (red) TMPyP adsorption to the silica surface, The dotted line is the best fit to the data with k = 0.05 cm s^{-1} (λ = 3). The solid black line shows the results of the simulations for k = 0.07 cm s^{-1} (λ = 3) to demonstrate that finite kinetics can be resolved.

5.4.6 Interaction of DNA with TMPyP-Functionalised Silica Surfaces

Figure 5.16 shows how the EW-CRDS response changes when a TMPyP-functionalised silica surface is exposed to different concentration CT-DNA solutions. The absorbance due to surface-adsorbed TMPyP decreases significantly upon introduction of the DNA solution as a result of TMPyP desorption. It was demonstrated earlier (Figure 5.7) that a TMPyP-(CT-DNA) complex forms readily in solution and this drives the desorption of TMPyP from the silica surface. The absorbance signal tends to zero at long times, indicating that the TMPyP-(CT-DNA) complex desorbs from the silica surface into

the solution rather than binding of the DNA to the surface. This is probably due to the large electrostatic repulsion between the negatively charged CT-DNA and the silica surface. To confirm that no DNA remained on the surface, *in situ* AFM experiments were carried out which showed the surface remained clear (data not shown).

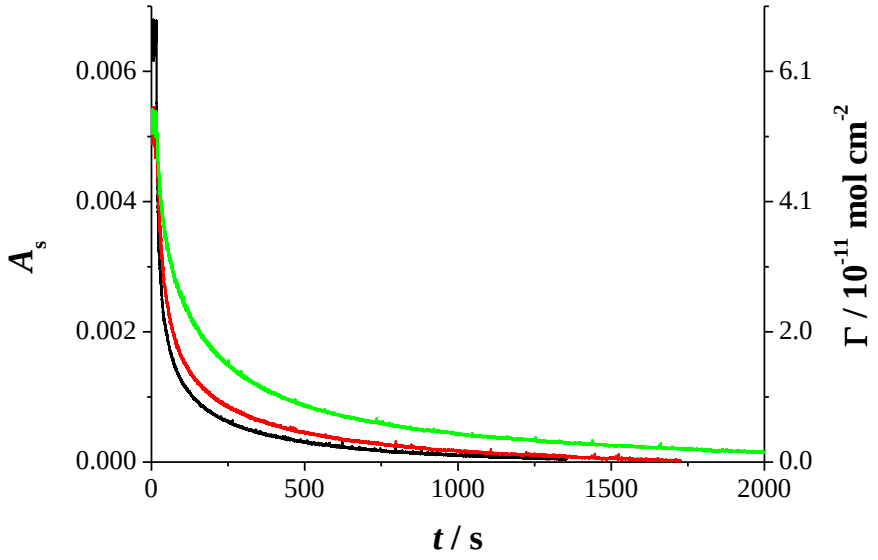

Figure 5.16 EW-CRDS measurements of TMPyP-modified silica surface after exposure to solutions of CT-DNA with concentrations of 0.3 mg mL^{-1} (black), 0.1 mg mL^{-1} (red) and 0.05 mg mL^{-1} (green) in buffer (1 mM PBS, 10 mM NaCl, pH 7.4). In each case 0.5 mL of solution was dropped into the cell with a pipette.

To determine if the CT-DNA solution effected the orientation of the surface adsorbed TMPyP, further polarisation-dependent EW-CRDS experiments were performed. The prism was modified by a monolayer of TMPyP by adsorbing 0.5 μM TMPyP in 1 mM PBS (pH 7.4) until the signal reached a plateau. The surface was then washed using 1 mM PBS at pH 7.4. 1 mg mL^{-1} CT-DNA in 1 mM PBS (pH 7.4) was then introduced the surface and the polarisation-dependent EW_CRDS response is shown in

Figure 5.17. The results agree qualitatively with those displayed in Figure 5.16 and show no deviation in the dichroic ratio from 1.18 indicating that the adsorbed TMPyP is randomly oriented throughout the experiment.

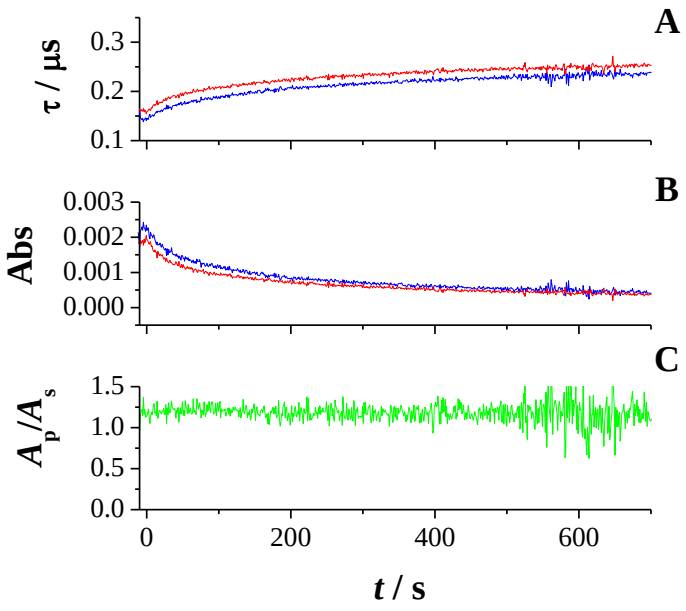

Figure 5.17 Polarisation-dependent EW-CRDS measurement of the DNA-assisted desorption of TMPyP. At *t* = 0 seconds 1 mg mL^{-1} CT-DNA in 1 mM PBS (pH 7.4) was introduced to the TMPyP-modified prism surface. A) The change in ring-down time with time for the *p*-polarised component (red) and the *s*-polarised component (blue). B) The time-dependent absorbances in the *p*-polarised component (red) and *s*-polarised component (blue). C) The dichroic ratio, A_p/A_s as a function of time.

To study the kinetics of DNA-induced porphyrin desorption in detail, the flow cell system was used to introduce CT-DNA solution with the flow rate of 1 mL min^{-1}. The TMPyP-functionalised silica surface was again prepared as before and the CT-DNA solution was then flowed over this surface as the interfacial absorbance was monitored via the EW-CRDS signal. Figure 5.18 shows the TMPyP coverage as a fraction of the initial TMPyP surface concentration as a function of time. The desorption rate was, as

expected, dependent on the concentration of CT-DNA with the surface coverage decreasing more rapidly as the DNA concentration increased from 0.05 to 0.3 mg mL^{-1}.

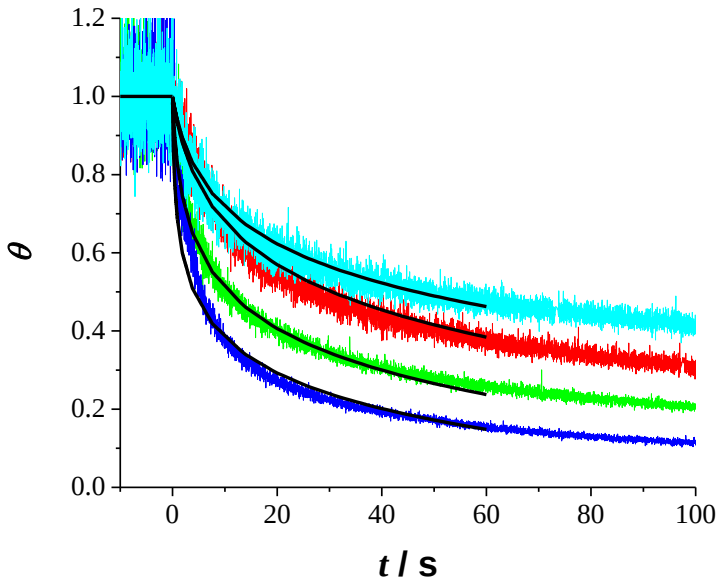

Figure 5.18 EW-CRDS measurements of a TMPyP-functionalised silica prism during exposure to different CT-DNA concentrations: 0.3 mg mL^{-1} (blue), 0.2 mg mL^{-1} (green), 0.1 mg mL^{-1} (red) and 0.05 mg mL^{-1} (cyan) in buffer (1 mM PBS, 10 mM NaCl, pH 7.4). The flow rate was 1 mL min^{-1} and the nozzle-to-prism distance was 500 μm. The black lines are the fits to the model with k' = (1.9 ± 0.1) × 10^{-4} cm^3 mol^{-1} s^{-1} with λ = 9.9 ± 0.6.

Using the model outlined earlier, the desorption rate of TMPyP from the surface due to binding with CT-DNA was found to be k' = 1.9 (± 0.1) × 10^{-4} cm^3 mol^{-1} s^{-1} with λ = 9.9 ± 0.6 (see Figure 5.18 for the best fits to the experimental data). From these parameters the initial binding rate constant was determined to be k_0 = 4.3 (± 0.2) cm^3 mol^{-1} s^{-1}. These data indicate that the kinetics of the desorption process are strongly affected by the DNA concentration in solution and such an approach may be interesting for the quantitative analysis of DNA in solution.

5.5 Conclusions

The adsorption kinetics of TMPyP at the silica-water interface (1 mM PBS, pH 7.4) were probed using a fast flow impinging (confined) jet system and, on a clean surface, is characterised by a first order heterogeneous rate constant, $k = 4.1\ (\pm\ 0.6) \times 10^{-2}$ cm s^{-1}. The limiting value of the optical absorbance of adsorbed TMPyP corresponded approximately to full monolayer coverage (6.2×10^{13} molecules/cm^2). Competitive binding between the TMPyP ion and Na^+ was observed and quantified using both UV-visible spectroscopy and EW-CRDS.

Further studies investigated the effect of CT-DNA on a TMPyP-functionalised silica surface. Efficient DNA-assisted desorption of TMPyP from the silica surface was observed with an initial rate constant of 4.3 ($\pm$ 0.2) cm^3 mol^{-1} s^{-1}. This suggests that TMPyP-functionalised surfaces, and related functionalised surfaces, coupled to a surface-sensitive spectroscopic technique such as EW-CRDS may be useful as a DNA sensor.

The studies herein provide further evidence of the sensitivity (in terms of both time and surface concentration) of EW-CRDS as a technique for probing kinetics at condensed phase interfaces and was the first demonstration of EW-CRDS combined with such a flow-cell system which should allow the study of biomolecular interactions on the timescale highlighted herein, or better.

5.6 References

1. (a) Marzilli, L. G. In *Medical Aspects Of Dna-Porphyrin Interactions*, Conf on New Perspectives in Organometallic Chemistry, Konigstein Am Taunus, Fed Rep Ger, Sep 25-29; Konigstein Am Taunus, Fed Rep Ger, 1989; pp 409-420; (b) Villanueva, A.; Juarranz, A.; Diaz, V.; Gomez, J.; Canete, M., Photodynamic Effects Of A Cationic Mesosubstituted Porphyrin In Cell-Cultures. *Anti-Cancer Drug Design* **1992,** *7* (4), 297-303.

2. Eggleston, M. K.; Crites, D. K.; McMillin, D. R., Studies of the base-dependent binding of Cu(T4) to DNA hairpins (H(2)T4 = meso-tetrakis(4-(N-methylpyridiumyl))porphyrin). *Journal of Physical Chemistry A* **1998,** *102* (28), 5506-5511.

3. (a) Butler, W. L., Primary Photochemistry Of Photosystem II Of Photosynthesis. *Accounts of Chemical Research* **1973,** *6* (6), 177-184; (b) Kay, A.; Gratzel, M., Artificial photosynthesis .1. Photosensitization of TiO2 solar-cells with chlorophyll derivatives and related natural porphyrins. *Journal of Physical Chemistry* **1993,** *97* (23), 6272-6277.

4. McMillin, D. R.; Shelton, A. H.; Bejune, S. A.; Fanwick, P. E.; Wall, R. K., Understanding binding interactions of cationic porphyrins with B-form DNA. *Coordination Chemistry Reviews* **2005,** *249* (13-14), 1451-1459.

5. McMillin, D. R.; Shelton, A. H.; Bejune, S. A.; Fanwick, P. E.; Wall, R. K. In *Understanding binding interactions of cationic porphyrins with B-form DNA*, 15th International Symposium on Photochemistry and Photophysics of Coordination Compounds, Hong Kong, Peoples R China, Jul 04-09; Hong Kong, Peoples R China, 2004; pp 1451-1459.

6. (a) Kim, M. Y.; Gleason-Guzman, M.; Izbicka, E.; Nishioka, D.; Hurley, L. H., The different biological effects of telomestatin and TMPyP4 can be attributed to their selectivity for interaction with intramolecular or intermolecular G-quadruplex structures. *Cancer Research* **2003,** *63* (12), 3247-3256; (b) Wei, C. Y.; Jia, G. Q.; Yuan, J. L.; Feng, Z. C.; Li, C., A spectroscopic study on the interactions of porphyrin with G-quadruplex DNAs. *Biochemistry* **2006,** *45* (21), 6681-6691; (c) Parkinson, G. N.; Ghosh, R.; Neidle, S., Structural basis for binding of porphyrin to human telomeres. *Biochemistry* **2007,** *46* (9), 2390-2397.

7. Blom, N.; Odo, J.; Nakamoto, K.; Strommen, D. P., Resonance Raman Studies of Metal Tetrakis(4-N-Methylpyridyl)Porphine - Band Assignments, Structure-Sensitive Bands, and Species Equilibria. *Journal of Physical Chemistry* **1986,** *90* (13), 2847-2852.

8. Sehlstedt, U.; Kim, S. K.; Carter, P.; Goodisman, J.; Vollano, J. F.; Norden, B.; Dabrowiak, J. C., Interaction of cationic porphyrins with Dna. *Biochemistry* **1994,** *33* (2), 417-426.

9. Jasuja, R.; Jameson, D. M.; Nishijo, C. K.; Larsen, R. W., Singlet excited state dynamics of tetrakis(4-N-methylpyridyl)porphine associated with DNA nucleotides. *Journal of Physical Chemistry B* **1997,** *101* (8), 1444-1450.

10. Pasternack, R. F.; Bustamante, C.; Collings, P. J.; Giannetto, A.; Gibbs, E. J., Porphyrin assemblies on DNA as studied by a resonance light-scattering technique. *Journal of the American Chemical Society* **1993,** *115* (13), 5393-5399.

11. Lei, J. P.; Ju, H. X.; Ikeda, O., Supramolecular assembly of porphyrin bound DNA and its catalytic behavior for nitric oxide reduction. *Electrochimica Acta* **2004,** *49* (15), 2453-2460.

12. Naue, J. A.; Toma, S. H.; Bonacin, J. A.; Araki, K.; Toma, H. E., Probing the binding of tetraplatinum(pyridyl)porphyrin complexes to DNA by means of surface plasmon resonance. *Journal of Inorganic Biochemistry* **2009,** *103* (2), 182-189.

13. Kalyanasundaram, K.; Neumannspallart, M., Photophysical and redox properties of water-soluble porphyrins in aqueous-media. *Journal of Physical Chemistry* **1982,** *86* (26), 5163-5169.

14. Marmur, J.; Doty, P., Determination of the base composition of deoxyribonucleic acid from its thermal denaturation temperature. *Journal of Molecular Biology* **1962,** *5* (1), 109-118.

15. Pasternack, R. F.; Gibbs, E. J.; Villafranca, J. J., Interactions of porphyrins with nucleic-acids. *Biochemistry* **1983,** *22* (10), 2406-2414.

16. (a) Burt, D. P.; Cervera, J.; Mandler, D.; Macpherson, J. V.; Manzanares, J. A.; Unwin, P. R., Scanning electrochemical microscopy as a probe of Ag^+ binding kinetics at Langmuir phospholipid monolayers. *Physical Chemistry Chemical Physics* **2005,** *7* (15), 2955-2964; (b) Slevin, C. J.; Unwin, P. R., Lateral proton diffusion rates along stearic acid monolayers. *Journal of the American Chemical Society* **2000,** *122* (11), 2597-2602.

17. Low, M. J. D., Kinetics of chemisorption of gases on solids. *Chemical Reviews (Washington, DC, United States)* **1960,** *60*, 267-312.

18. (a) Jaroniec, M., Elovich-type equations for description of the adsorption rates of gas mixtures. *Journal of Catalysis* **1979,** *57* (1), 187-90; (b) Rudzinski, W.; Panczyk, T., Surface heterogeneity effects on adsorption equilibria and kinetics. Rationalizations of the Elovich equation. *Surfactant Science Series* **1999,** *78* (Surfaces of Nanoparticles and Porous Materials), 355-389.

19. (a) Elkhatib, E. A.; Mahdy, A. M.; Saleh, M. E.; Barakat, N. H., Kinetics of copper desorption from soils as affected by different organic ligands. *International Journal of Environmental Science and Technology* **2007,** *4* (3), 331-338; (b) Hellal, F. A.; Amer, A. K.; Zaghloul, A. M., Effect of applied iron on iron desorption in soil and uptake by wheat plants. *Journal of Applied Biological Sciences* **2008,** *2* (2), 79-86; (c) Nafiu, A.; Agbenin, J. O.; Raji, B. A., Kinetic desorption of native phosphorus from soils of varying lithogenic origins in the Nigerian Savanna. *Soil Science* **2008,** *173* (12), 837-844; (d) Yang, Y.; Liang, L.; Wang, D., Effect of dissolved organic matter on adsorption and desorption of mercury by soils. *Journal of Environmental Sciences (Beijing, China)* **2008,** *20* (9), 1097-1102.

20. Bitziou, E.; Rudd, N. C.; Edwards, M. A.; Unwin, P. R., Visualization and Modeling of the Hydrodynamics of an Impinging Microjet. *Analytical Chemistry* **2006,** *78* (5), 1435-1443.

21. Sambrook, J.; Russell, D. W., *Molecular Cloning A Laboratory Manual*. 3 ed.; Cold Spring Harbor Laboratory Press: Cold Spring Harbor, New York, 2001; Vol. 1.

22. Lugo-Ponce, P.; McMillin, D. R. In *DNA-binding studies of Cu(T4), a bulky cationic porphyrin*, 13th International Symposium on Photochemistry and Photophysics of Coordination Compounds (ISPPCC), Lipari, Italy, Jun 27-Jul 02; Lipari, Italy, 1999; pp 169-191.

23. Powell, H. V.; Schnippering, M.; Mazurenka, M.; Macpherson, J. V.; Mackenzie, S. R.; Unwin, P. R., Evanescent Wave Cavity Ring-Down Spectroscopy as a Probe of Interfacial Adsorption: Interaction of Tris(2,2 '-bipyridine)ruthenium(II) with Silica Surfaces and Polyelectrolyte Films. *Langmuir* **2009,** *25* (1), 248-255.

24. Bard, A. J.; Faulkner, L. R., *Electrochemical Methods: Fundamentals and Applications*. 2nd ed.; John Wiley & Sons Inc.: 2001.

25. Fan, H. F.; Li, F.; Zare, R. N.; Lin, K. C., Characterization of Two Types of Silanol Groups on Fused-Silica Surfaces Using Evanescent-Wave Cavity Ring-Down Spectroscopy. *Anal. Chem.* **2007,** *79* (10), 3654-3661.

26. Bos, M. A.; Werkhoven, T. M.; Kleijn, J. M., Adsorption behavior and orientation of tetrakis(methylpyridiniumyl)porphyrin on silica. *Langmuir* **1996,** *12* (16), 3980-3985.

Chapter 6. Bilayer Formation and Porphyrin Adsorption

This chapter describes the study of the formation of cationic supported lipid bilayers (SLBs) of 1,2-dioleoyl-3-trimethylammonium-propane chloride salt (DOTAP) on a silica substrate *in situ* using EW-CRDS. Complementary Quartz Crystal Microbalance with Dissipation (QCM-D) and Atomic Force Microscopy (AFM) measurements confirmed the formation of bilayers on the surface. The subsequent interaction of the anionic porphyrin, 5,10,15,20-Tetraphenyl-21H, 23H-porphine-p,p′,p″,p‴-tetrasulfonic acid tetrasodium hydrate (TPPS) with the bilayer-modified silica surface was studied using EW-CRDS combined with an impinging-jet to deliver analyte to the surface in a well-defined way. The adsorption of the TPPS to the bilayer was kinetically controlled and the adsorption rate constant was found to be $(1.66 \pm 0.59) \times 10^{-4}$ cm s^{-1} from finite element models of the flow and convection-diffusion coupled to a first-order surface process describing the adsorption. This work provides a platform for the study of the kinetics of the associations of ions, peptides and proteins with biomembranes using EW-CRDS or even to study the electrochemistry of redox active proteins in a biomimetic environment.

6.1 Introduction

6.1.1 Supported Lipid Bilayers as Biomimetic Membranes

Processes occurring at biological membranes are fundamental to a multitude of important biological pathways *in vivo*.[1] Elucidating the kinetics and mechanisms of such

processes is important for understanding processes such as cell signalling[2, 3] and energy transduction,[4] and is also essential for developing and optimising bio-devices[5] for sensors,[6, 7] biofuel cells,[8] bio energy production,[9] chemical production and separation,[10] and for therapeutic applications as explained in Chapter 1.[11] Since the first demonstration of a planar phospholipid bilayer by Mueller *et al.* in 1962,[12] such biomembrane mimics have received considerable attention. One particular class of these planar bilayers, solid-supported lipid bilayers (SLBs), has been used extensively as models for cellular membranes.[6, 13] Cationic phospholipids[14] have received considerable attention due to their applicability to drug delivery,[15] transfection,[16] gene silencing[17] and the ability to form supermolecular complexes with DNA.[18]

6.1.2 Techniques to Form SLBs

The most popular method used to form SLBs is the vesicle fusion method.[2, 19] The principle behind this method is that under appropriate conditions, small unilamellar vesicles (SUV) of phospholipids in solution adsorb to a solid substrate and subsequently rupture (either spontaneously or once a critical surface coverage has been achieved) to form a bilayer on the substrate. There are a number of ways to form solutions of SUV including ultracentrifugation,[20] sonication[21] and extrusion.[22] The popularity of the vesicle fusion method is most likely due to its simplicity and because it is relatively straightforward to incorporate membrane proteins into the SLB by forming proteoliposomes.[23] However, the disadvantage to this method is the extreme sensitivity of the resulting film to the vesicle size,[24] substrate (charge and morphology are both important),[25] the electrolytes in solution and the ionic strength,[26-28] the pH of the buffer,[29]

and the temperature.[29, 30] If the conditions are not right, the vesicles may adsorb but not rupture leaving a layer of intact vesicles.[31, 32]

Other commonly used methods of forming SLBs include the Langmuir-Blodgett and Langmuir-Schaeffer techniques.[33, 34] In this method, the substrate is pulled vertically through a lipid monolayer formed at the air-water interface, followed by pushing the substrate horizontally through the monolayer. The first step forms a monolayer on the substrate while the second deposits a further monolayer to complete the bilayer. It is also possible to use adsorb vesicles to a monolayer created using the Langmuir-Blodgett technique.[35] Less commonly used bilayer formation techniques include spin coating[36-38] and air bubble collapse.[39]

6.1.3 Current Techniques Used to Study SLB Formation

Probably the most well established technique used to follow the kinetics of SLB formation is QCM-D.[25, 26, 29, 30, 32, 40-44] Using this technique, two pathways of bilayer formation were identified.[32] In pathway 1, the vesicles adsorb to the surface and rupture spontaneously to form bilayer patches. The characteristic QCM-D response in this case is a decrease in frequency which plateaus at -27 Hz, and little or no change in the dissipation. In pathway 2, the vesicles adsorb but do not rupture until a critical surface coverage is reached. The QCM-D response to bilayer formation by this pathway is a decrease in frequency accompanied by an increase in dissipation, followed by an increase in frequency and decrease in dissipation. The final frequency and dissipation values are -27 Hz and 0.5×10^{-6}, respectively. The formation of supported vesicle layers (no rupture) can also be identified by a frequency curve that decreases and plateaus at a frequency below -27 Hz which is combined with a large change in dissipation. Surface plasmon

resonance (SPR),[41, 42, 45-47] atomic force microscopy (AFM),[30, 46, 48-50] attenuated total reflectance infrared spectroscopy,[51] ellipsometry[28, 40, 52] and fluorescence[42, 49] have also been used to follow the formation of supported lipid bilayers. Characterisation of the supported lipid bilayers once formed is achieved by a wide-range of techniques. Spectroscopic methods such as neutron reflectivity,[36, 38, 53, 54] X-ray scattering,[38, 54, 55] Sum Frequency Vibrational Spectroscopy,[34] and Raman Spectroscopy[56] are commonly used. Scanning probe techniques including spatially resolved mass spectrometry to determine lipid distribution in the bilayer[57] and AFM[37, 47, 58] to characterise the topology of the bilayer and possibly identify domains of lipids. Fluorescence recovery after photobleaching (FRAP) is often used to demonstrate the fluidity of the bilayer.[59]

6.2 Experimental

6.2.1 Materials

1,2-dioleoyl-3-trimethylammonium-propane chloride salt (DOTAP) and 1,2-dioleoyl-sn-glycero-3-phosphocholine (DOPC) were purchased from Avanti Polar Lipids and stock solutions were stored in chloroform at -20º C. 5,10,15,20-Tetraphenyl-21*H*, 23*H*-porphine-*p*,*p*′,*p*″,*p*‴-tetrasulfonic acid tetrasodium hydrate (TPPS – see Figure 6.1) was purchased from Sigma-Aldrich and solutions were prepared prior to experiments. Two buffers were used: phosphate buffer solution (PBS - pH 7.4) was prepared from sodium phosphate dibasic (Sigma-Aldrich) and sodium phosphate monobasic monohydrate (Sigma-Aldrich), and Buffer A consisted of 150 mM NaCl (Fisher Scientific), 10 mM HEPES (Fluka), 2 mM NaN_3 (Sigma) and 2 mM EDTA (Aldrich) and

was adjusted to pH 7.4 using NaOH (Sigma-Aldrich). Ultrapure water was obtained from a Milli-Q plus 185 system from Millipore (resistivity of 18.2 MΩ cm at 25ºC).

6.2.2 UV-visible Spectroscopy

UV-visible spectra of TPPS, DOPC vesicles and DOTAP vesicles were measured using a Lambda 25 UV-visible spectrometer (Perkin-Elmer Instruments) using a 1 cm quartz cuvette.

6.2.3 SUV Preparation

Small unilamellar vesicle (SUV) solutions were prepared as follows. Stock solution of phospholipid was dried in a nitrogen stream and vacuum desiccated for at least 4 hours to remove the chloroform. The lipids were then resuspended in buffer A to a concentration of 0.1 mg mL^{-1}, sonicated for 2 minutes to ensure complete resuspension, freeze-thawed five times before finally being extruded through 100 nm polycarbonate membranes (GC Technology). SUV solutions were used within 4 hours of preparation.

6.2.4 QCM-D of DOTAP and DOPC Adsorption at SiO_2

Quartz Crystal Microbalance measurements were obtained using a Q-Sense Flow Module. SiO_2 coated AT-cut quartz crystals (f_0 = 4.95 MHz, Q-Sense) were cleaned by flowing 10 mg mL^{-1} sodium dodecyl sulfate (Fluka) over the surface for 20 minutes and then ultrapure H_2O (Millipore) for 1 hour, both at 0.2 mL min^{-1}. They were then dried in a stream of nitrogen before being ashed for 3 minutes at 100 W in oxygen plasma (Emitech, K1050X). Once mounted in the flow module, buffer was flowed over the sensor crystal at 10 μl min^{-1} to achieve a stable baseline. The change in frequency and dissipation were recorded as SUV solution was flown over the sensor crystal at 10 μl

min^{-1}. After the signal had stabilised, the bilayer was rinsed by flowing buffer over the crystal surface at 10 μl min^{-1}. All solutions were sonicated for 2 mins prior to introduction to the QCM-D to remove air bubbles.

6.2.5 TM-AFM of DOTAP SLB Formed on Quartz

Single crystal quartz wafers (Hoffman Materials, Inc.) were cleaned by sonicating in acetone for 5 minutes, followed by rinsing with isopropanol, then ashing at 100 W in oxygen plasma for 3 minutes. 100 μl of 0.1 mg mL^{-1} DOTAP SUV solution was pipetted on top and left to adsorb for 15 minutes. The surface was then washed using 3 mL of buffer A and kept under solution for TM-AFM. Topographical images of the surface were obtained using a Veeco Enviroscope AFM.

6.2.6 Monitoring SLB Formation Using EW-CRDS

The EW-CRDS set-up was as described in Section 2.1. The background ring-down time, τ_0, was recorded with buffer in the cell. The buffer was removed and the EW-CRDS signal recorded as 500 μl of SUV solution was dropped into the cell using a plastic pipette. The resulting bilayer formed from the DOTAP solution (the DOPC vesicles adsorbed to form a layer of intact vesicles - see Section 6.3.3) was rinsed using the impinging jet cell described in Section 2.2. The nozzle-prism separation was chosen to be 500 μm to ensure that it did not penetrate the evanescent field. 10 mL of buffer A was flowed over the bilayer at a rate of 0.5 mL min^{-1} to ensure complete removal of the SUVs in solution and to check the stability of the bilayer under these flow conditions.

6.2.7 EW-CRDS of TPPS on SiO_2 and SLB-Modified SiO_2

To determine if TPPS adsorbs to silica the EW-CRDS signal was recorded as 500 μl of 10 μM TPPS in buffer A was pipetted directly onto the prism surface. To determine the value of the absorbance due to TPPS in bulk solution it was necessary to record the background ring-down time with 500 μl buffer A in the cell first, before adding 500 μl of 10 μM TPPS in buffer A and allowing the EW-CRDS signal to stabilise.

The EW-CRDS signal was recorded as TPPS solutions (concentrations: 0.5 μM, 1 μM, 2 μM, 3 μM, 4 μM and 5 μM) in buffer A were flowed over bilayer-modified prisms using the impinging jet cell described in Section 2.2. The flow rate was again 0.5 mL min^{-1} and the nozzle-prism separation was 500 μm.

6.2.8 Simulations and Modelling

The model used to simulate the adsorption of TPPS to the bilayer-modified surface was similar to that described in Section 5.3.1. The axially symmetric geometry for the fluid flow problem is shown in Figure 5.2. The time-independent incompressible Navier-Stokes equation was solved to obtain the velocities, u and v, in the r and z directions respectively, at each mesh point in the domain shown in Figure 5.2. No slip boundary conditions were applied to the walls of the pipe and the silica surface, and the following boundary conditions applied at the inlet of the pipe:

$$u = 0, v = \frac{2v_f}{\pi r_{in}^2}\left(1 - \frac{r^2}{r_{in}^2}\right) \quad z = H, \quad 0 \le r \le r_{in} \tag{6.1}$$

where v_f is the flow rate in $m^3\ s^{-1}$ and r_{in} is the pipe inner radius. There was assumed to be no pressure at the outlet ($r = r_{out}, 0 \le z \le d$). The use of equation (6.1) assumes fully-

developed laminar (Poiseuille) flow in the pipe (before the outlet) and is reasonable for the flow rates and the nozzle used, of diameter 2 mm and length 5 cm.

The solution of the convection-diffusion equation for the concentration of TPPS, c, in the adsorption model was obtained in the subdomain shaded in grey in Figure 5.2. No flux boundary conditions were applied to the pipe walls and a convective flux boundary condition was applied to the outlet ($r = w, 0 \le z \le d$). The boundary condition at the solution inlet ($z = h, 0 \le r \le r_{in}$) was that the solution concentration was equal to that of bulk, $c = c^*$.

Due to the large extinction coefficient of TPPS at 405 nm and the high sensitivity of EW-CRDS, we focused on monitoring the adsorption profile of small surface coverages of TPPS at the bilayer due to the upper limit of detection of EW-CRDS. In this regime, it was possible to model the adsorption as a first-order surface process. Thus, the boundary condition at the prism surface was:

$$D\frac{\partial c}{\partial z} = -kc \tag{6.2}$$

$$\frac{d\Gamma}{dt} = kc \tag{6.3}$$

where D is the diffusion coefficient of TPPS in solution, Γ is the surface coverage of TPPS, and k is the initial adsorption rate constant. The initial conditions were $\Gamma = 0$ and $c = c^*$. Desorption processes were not considered and assumed to be negligible at such low surface coverages, and for conditions where the adsorption process was so far from equilibrium.

6.3 Results and Discussion

6.3.1 UV-visible Absorption Spectroscopy

The UV-visible absorption spectra of 2 μM, 5 μM, 10 μM TPPS in buffer A are shown in Figure 6.2 A. The main peak is at 413 nm for all three spectra and the absorbance is linear with concentration indicating that the TPPS does not form aggregates at these concentrations. The inset of Figure 6.2 A shows the dependence of the absorbance at 405 nm on the TPPS concentration. A linear fit to the data gives the extinction coefficient as $\varepsilon_{405} = 1.15 \times 10^5$ dm^3 mol^{-1} cm^{-1}.

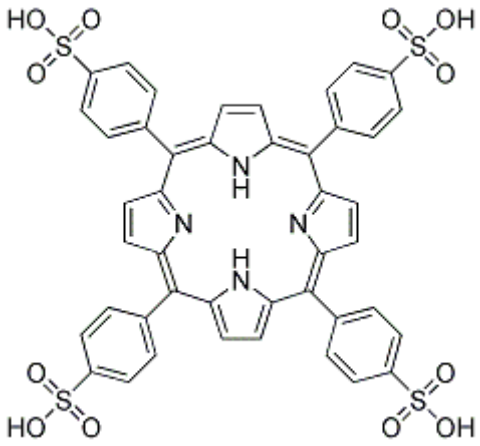

Figure 6.1 The TPPS molecule.

The absorption spectrum of 1 mg mL^{-1} DOTAP vesicle solution in buffer A (pH 7.4) is shown in Figure 6.2 B. The spectrum for DOPC vesicles was practically identical. The spectrum was dominated by the scattering due to the vesicles so it was not possible to obtain the absorbance due to the phospholipids in this environment. The optical extinction of a 1 mg mL^{-1} DOTAP SUV solution at 405 nm was 0.35. If the phospholipids in a vesicle occupy the same area per molecule as when supported on a

substrate (determined to be 55 $Å^2$ by Keller *et al.*[43]), the mass per vesicle can be estimated from the radius of the vesicles, which can in turn be used to estimate the vesicle concentration in solution. With a vesicle radius of 50 nm, the concentration of vesicles in solution, c_V, was estimated to be 1.13×10^{-11} moles cm^{-3}. A scattering "extinction coefficient" per mole of vesicles at 405 nm was then calculated using the Beer-Lambert law to give $\varepsilon_V^{405} = 3.1 \times 10^{10}$ cm^2 mol^{-1}. The amount of optical extinction was assumed to be linear wth vesicle concentration so that ε_V^{405} could be used in the analysis of the EW-CRDS data in Section 6.3.3.

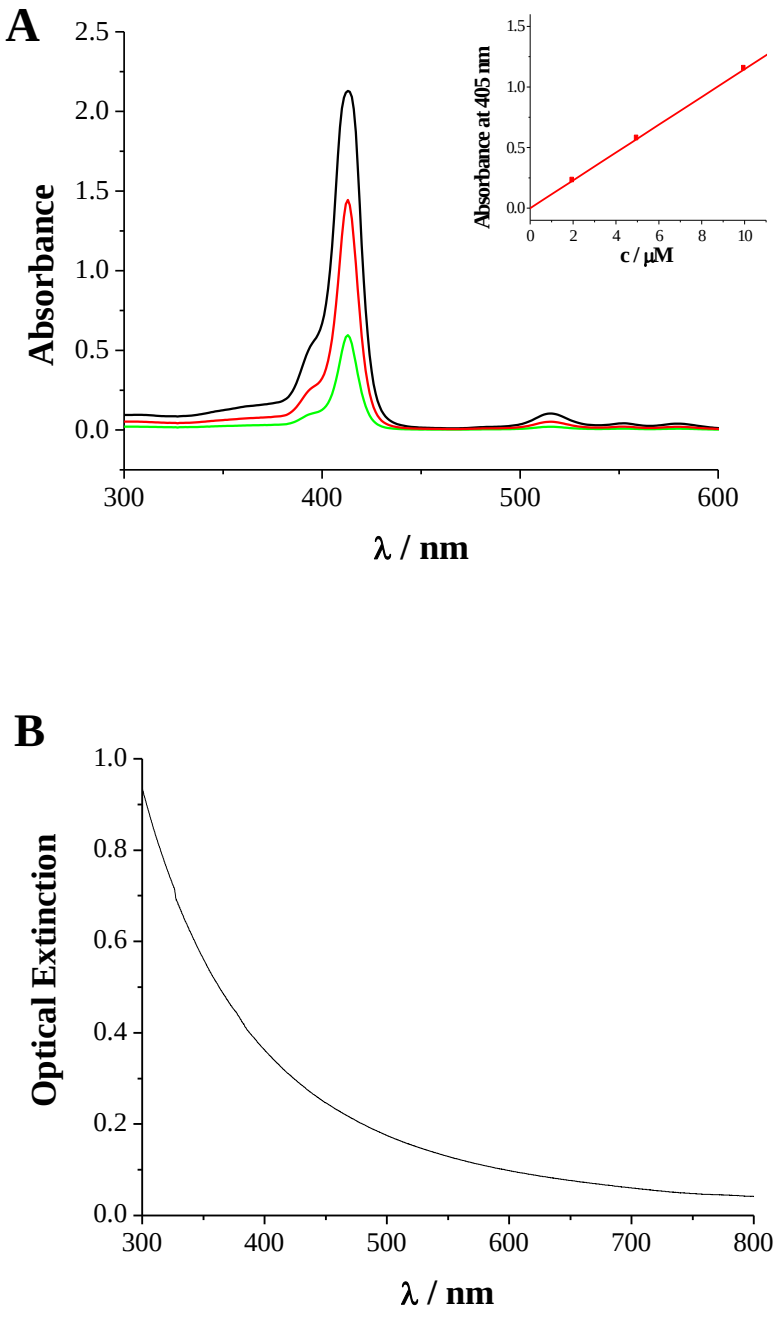

Figure 6.2 A) UV-visible absorption spectra for 2 μM (green), 5 μM (red) and 10 μM (black) TPPS in buffer A. Inset: The absorbance at 405 nm plotted against the TPPS concentration. The line of best fit to the data gives ε_{405nm} = 1.15 × 10^5 dm^3 mol^{-1} cm^{-1}. B) UV-visible absorption spectrum of 1 mg mL^{-1} DOTAP in buffer A (pH 7.4).

6.3.2 Characterisation of SLB-Modified Silica by QCM-D and AFM

The QCM-D response to the flow of 1 mg mL^{-1} DOPC in 10 mM PBS (pH 7.4) with 0.1 M NaCl over SiO_2 QCM-D crystals at 100 μl min^{-1} is shown in Figure 6.3. Upon the introduction of DOPC to the sensor chip, the frequency starts to decrease and the dissipation increases. After 1 hour the experiment was stopped and as can be seen from the data in Figure 6.3, the frequency changed by -146 Hz and was still decreasing and the dissipation was 57×10^{-6} and still increasing. Such large changes in frequency and dissipation are characteristic of the formation of a supported vesicle layer.[32]

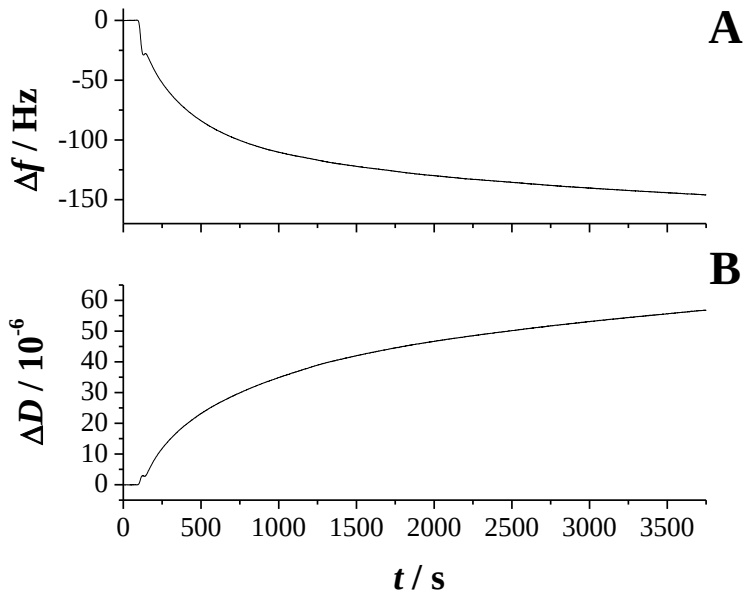

Figure 6.3 The QCM-D response to the flow of 1 mg mL^{-1} DOPC in 10 mM PBS (pH 7.4) and 0.1 M KCl. A shows the change in frequency and B the dissipation.

In contrast, the QCM-D response upon flowing 0.1 mg mL^{-1} DOTAP SUV solutions over the sensor crystals at a rate of 10 μl min^{-1} is shown in Figure 6.4. Upon

addition of DOTAP to the cell (t = 1000 s), the frequency (Figure 6.4 A) decreased to a minimum of -50 Hz after a further 9 minutes (to t = 1550 s) and then increased until it reached a stable value of -37 Hz after a further 6 minutes (t = 1900 s). The morphology of the curves was consistent with the formation of a SLB, but the final change in frequency was slightly larger than previous results for other lipids.[26, 29, 43, 44, 46, 50, 60] At t = 2000 s, the DOTAP solution was exchanged with buffer A solution to wash the surface. There was no change in the QCM-D signal indicating that the bilayer was stable under the flow of buffer A. The corresponding dissipation (Figure 6.4 B) initially increased with time to a maximum value and then decreased slightly before reaching a stable value, consistent with the formation of a SLB. The final change in dissipation was $\Delta D = 3.6 \times 10^{-6}$, which was greater than the value of $\Delta D = 0.5 \times 10^{-6}$ quoted in the literature for the dissipation of a SLB. The deviation in final values for Δf and ΔD suggested that some vesicles could still remain intact on parts of the surface in these particular experiments.

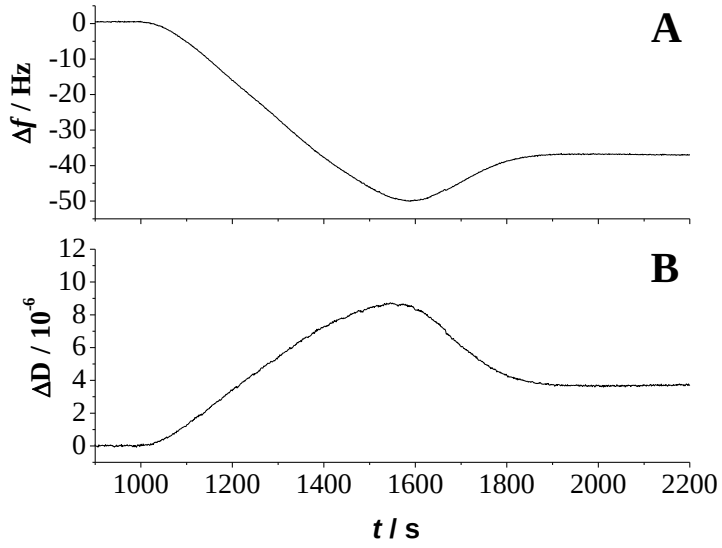

Figure 6.4 Change in frequency (A) and dissipation (B) recorded on the QCM-D upon flowing 0.1 mg mL^{-1} DOTAP in buffer A (pH 7.4) over the SiO_2 sensor chip.

In order to determine the extent of the surface on which bilayer had formed upon adsorption of DOTAP to silica, complementary *in situ* TM-AFM experiments were performed. SLBs were formed on single crystal quartz by adsorbing SUVs from 100 μl of 0.1 mg mL^{-1} DOTAP in buffer A for 15 minutes and then rinsing the surface with 3 mL of buffer A. A representative *in situ* TM-AFM image of the surface is shown in Figure 6.5 which is similar to the images obtained in previous reports.[32] In all areas imaged, the surface was uniform with the exception of a few 1-2 nanometer pits and bulges, and there was no evidence of adsorbed vesicles. Since the surface morphology is very similar to that of the underlying silica, contact mode AFM was used to cause deformation of the surface, which was subsequently imaged in tapping mode. The change in morphology after such an experiment (see Figure 6.6), indicated that a film had been formed on the surface.

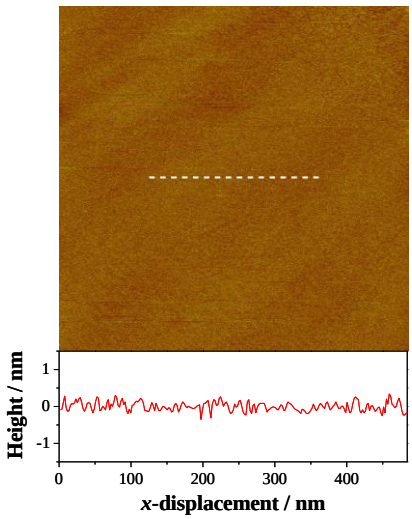

Figure 6.5 A typical 1 μm × 1 μm TM-AFM image of the surface after the adsorption of 0.1 mg mL^{-1} DOTAP for 15 minutes, and the height data through the cross-section shown.

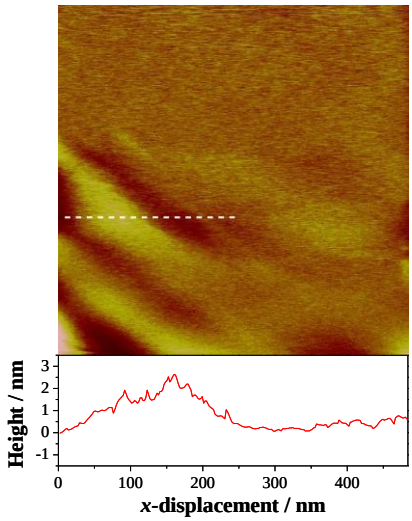

Figure 6.6 A TM-AFM image of the same area as shown in Figure 6.5 but after the surface has been deformed using contact mode AFM.

6.3.3 Following SUV Adsorption and SLB Formation Using EW-CRDS

The EW-CRDS response to the addition of 1 mg mL^{-1} DOPC in 10 mM PBS (pH 7.4) and 0.1 M KCl is shown in Figure 6.7. The optical absorbance increases from zero for an empty cavity, monotonically with time and even after 6 hours is still increasing.

The large change in the absorbance was attributed to the adsorption of vesicles to the prism surface, which would be expected to scatter strongly. The continuing increase in absorbance even after 6 hours of adsorption shows that the vesicles did not rupture during this time, which is in agreement with the results obtained with the QCM-D in Section 6.3.2.

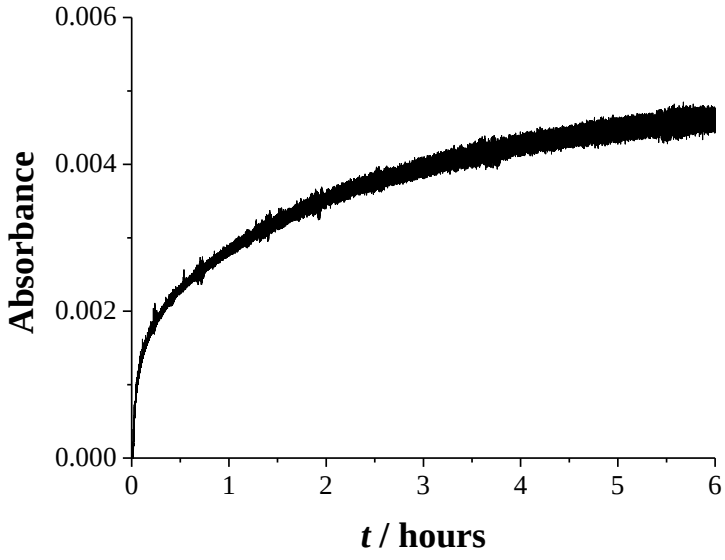

Figure 6.7 Change in absorbance due to the introduction of 1 mg mL^{-1} DOPC in 10 mM PBS (pH 7.4) and 0.1 M KCl.

Figure 6.8 shows the EW-CRDS response upon the introduction of 0.1 mg mL^{-1} DOTAP SUV solution to the prism surface. Unlike the data shown in Figure 6.7, the optical absorbance initially increased to a value of 1.7×10^{-4} after 16 s and then decreased to 1.1×10^{-5} after 60 s. The initial rise can be attributed to the adsorption of SUVs at the prism surface which would be expected to scatter light in the evanescent field. Assuming that the critical adsorbed mass of the vesicles is the same as the mass of the supported lipid bilayer (468 ng cm^{-2}, also determined by Keller *et al.*[43]), the number

of moles of vesicles per unit area was 5.3×10^{-15} mol cm^{-2}, which gave an absorbance on the surface of 1.6×10^{-4}, which is in very good agreement with the maximum of the surface absorbance in the EW-CRDS data shown in Figure 6.8.

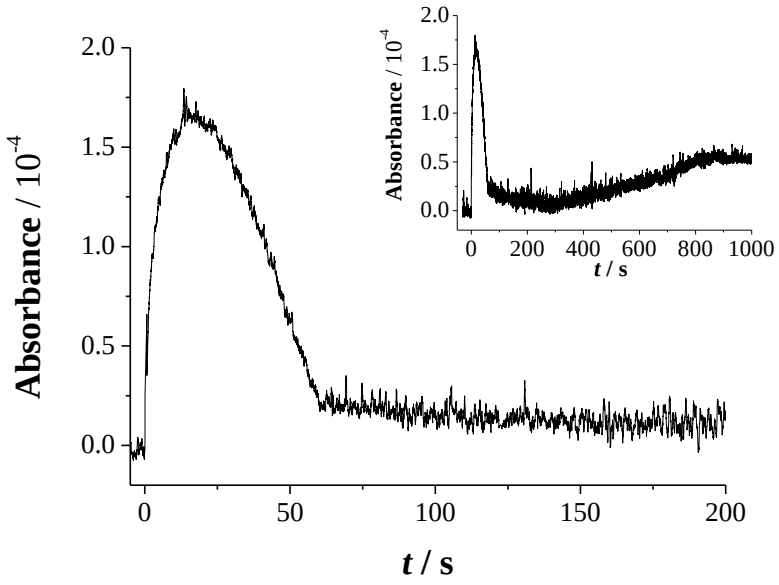

Figure 6.8 EW-CRDS response to the addition of 0.1 mg mL^{-1} DOTAP in buffer A (pH 7.4) to the prism surface. The inset shows the response over a longer time period to show the effect of washing the bilayer with buffer A using the flow cell described in Section 2.2.

After reaching the maximum of 1.7×10^{-4}, the optical absorbance decreases and reaches a steady value of 1.5×10^{-5} after 60 s. This can be explained by the rupturing of surface-adsorbed vesicles to form a SLB. The low final absorbance value, combined with the AFM data, suggest that the bilayer is uniform with little or no vesicles still intact. The difference between these data and the QCM-D results can be attributed to the need to sonicate the lipid solution prior to use in the QCM-D which may result in smaller vesicles[21, 22] which may be less likely to rupture.[61]

To remove excess vesicles from solution, 5 mL of buffer A was flowed over the surface in the impinging jet cell arrangement with a flow rate of 0.5 mL min^{-1} and a nozzle-prism separation of 500 μm. The inset of Figure 6.8 shows optical absorbance obtained from EW-CRDS over a longer time-period to show the response when buffer A was flowed over the surface at t = 300 s. The minor change in the optical absorbance of 3.1×10^{-5} is possibly due to rearrangements in the bilayer due to the shear force experienced from the fluid flow. It occurs, however, on a much longer timescale than the TPPS adsorption measurements reported in Section 6.3.4. We thus conclude from these studies that a homogeneous and stable bilayer can be formed for EW-CRDS experiments with flow.

6.3.4 EW-CRDS of TPPS on Silica and SLB-Modified Silica

As explained in Section 2.3, in order to obtain values of surface coverage it is necessary to determine what proportion of the EW-CRDS signal is due to absorbance by bulk solution. To this end, the EW-CRDS response was monitored upon the addition of TPPS to the cell. At pH 7.4, the silica surface is negatively charged[62] meaning that the negatively-charged TPPS would not be expected to adsorb to silica on electrostatic grounds. The EW-CRDS signal was recorded as 500 μl of 10 μM TPPS in buffer A was pipetted directly onto the prism surface and is shown in Figure 6.9 A. The immediate decrease in ring-down time to a steady-state indicates that the change is due solely to TPPS in bulk solution as adsorbing TPPS would cause the signal to decrease more gradually over time (as seen in Figure 3.4). In order to calculate the absolute absorbance by TPPS in bulk, it was first necessary to measure τ_0 with buffer A on the prism. Figure 6.9 B then shows the addition of 500 μl of 10 μM TPPS in buffer A to 500 μl of buffer A

in the cell above the prism. The absorbance increase in this case is more gradual than the change in ring-down time displayed in Figure 6.9 A, due to the mixing of the solution in the cell. The steady-state value of the optical absorbance, $A = 3.2 \times 10^{-4}$, corresponds to the bulk absorbance of 5 μM TPPS in buffer A. For the results that follow, the Beer-Lambert Law with the extinction coefficient determined in Section 6.3.1 was used to calculate A_b for each TPPS concentration, from which the optical absorbance due to analyte in the vicinity of the surface was calculated as outlined in Section 2.3.

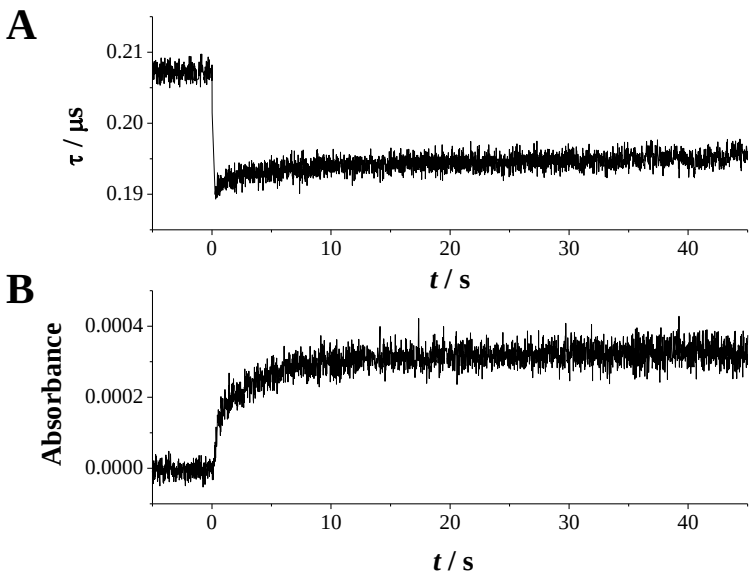

Figure 6.9 EW-CRDS response to the addition of 10 μM TPPS in buffer A (pH 7.4) to the prism surface. A) TPPS was directly pipetted onto a dry prism surface. B) 500 μl of 10 μM TPPS in buffer A was added to 500 μl of buffer A on the prism surface.

The adsorption of TPPS to the bilayer-modified prism was achieved by flowing solutions of TPPS in buffer A over the prism using the impinging jet cell. Figure 6.10 shows the bulk-corrected EW-CRDS response to the flow of TPPS concentrations of 0.5 μM, 1 μM, 2 μM, 3 μM, 4 μM and 5 μM over the prism surface at a rate of 0.5 mL min^{-1}.

The second y-ordinate in Figure 6.10 is the concentration of TPPS at the bilayer-aqueous interface calculated using the extinction coefficient, ε_{405} = 1.15 × 10^5 dm^3 mol^{-1} cm^{-1}, determined by UV-visible spectroscopy. The transients were essentially linear with time.

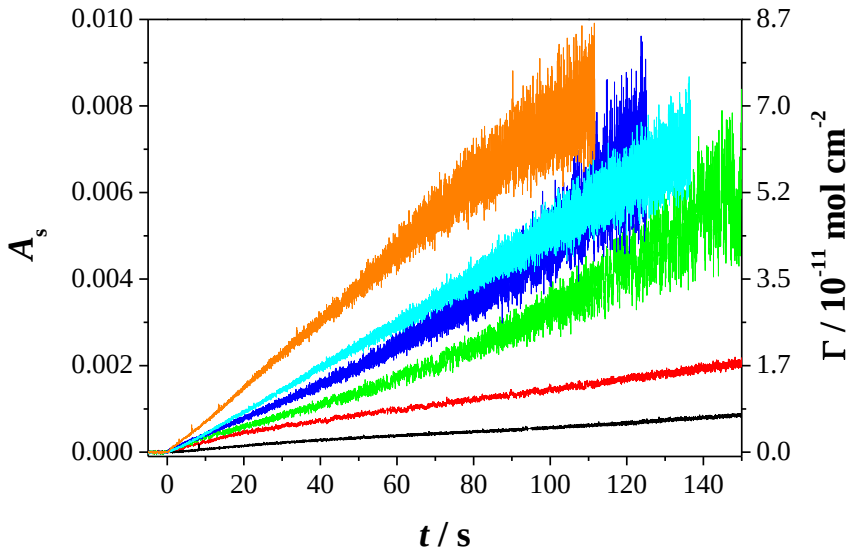

Figure 6.10 The EW-CRDS response to the flow of TPPS in buffer A over the bilayer-modified prism surface. The TPPS concentrations were 0.5 μM (black), 1 μM (red), 2 μM (green), 3 μM (blue), 4 μM (cyan), 5 μM (orange).

The effect of flow rate on the adsorption process for a bulk TPPS concentration of 0.5 μM can be seen in Figure 6.11. The EW-CRDS response shows only a small effect due to mass transport for the flow rates of 0.5 mL min^{-1}, 0.75 mL min^{-1} and 1 mL min^{-1}. This indicates that at the flow rate of 0.5 mL min^{-1}, the adsorption was kinetically controlled and so the transients in Figure 6.10 were fitted to a pseudo first-order adsorption process in the concentration of TPPS in solution as described in Section 6.2.8 above. The results of this fit are displayed in Figure 6.12. The average rate constant was found to be k = 1.66 (± 0.59) × 10^{-4} cm s^{-1}.

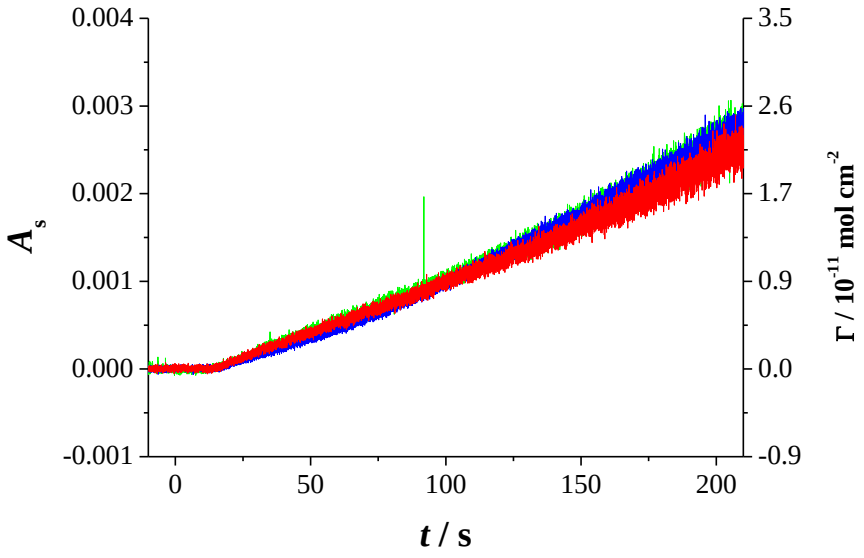

Figure 6.11 The effect of flow rate on the adsorption of TPPS to the bilayer-modified prism surface. The flow rates were 0.5 mL min^{-1} (red), 0.75 mL min^{-1} (green), and 1 mL min^{-1} (blue).

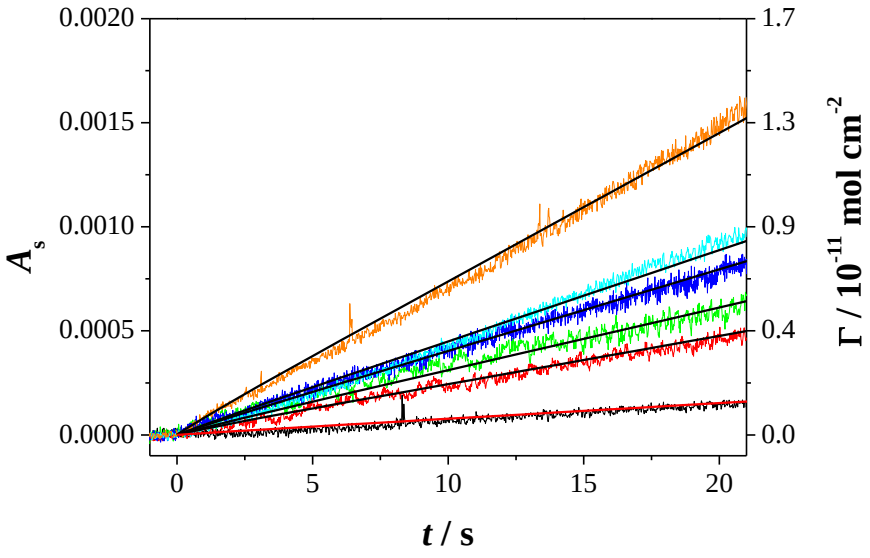

Figure 6.12 The EW-CRDS response to the adsorption of TPPS to the bilayer in addition to the fits the data using the model described in Section 6.2.8.

6.4 Conclusions and Outlook

This was the first study of the formation of a SLB via the method of vesicle fusion and molecular adsorption kinetics at the resulting SLBs using EW-CRDS. The contrast between the EW-CRDS data for DOPC and DOTAP clearly shows that it is possible to differentiate between the formation of a stable intact vesicle layer (DOPC) and a supported lipid bilayer (DOTAP) using EW-CRDS. To confirm that a supported lipid bilayer was formed from the DOTAP vesicles, complementary QCM-D and AFM experiments were performed. The *in situ* TM-AFM images showed that the resulting bilayer was uniform and free from defects. Furthermore, the DOTAP SLB was sufficiently optically transparent to allow the study of the adsorption of the anionic porphyrin, TPPS, in real-time to the bilayer-modified surface. The adsorption process was modelled using the finite element method, and the rate constant for the association of TPPS to the bilayer was found to be $(1.66 \pm 0.59) \times 10^{-4}$ cm s^{-1}. The ability to form a SLB on the prism inherent in EW-CRDS, and to monitor the interactions of biomolecules with the bilayer *in situ* and in real time, expands the applicability of EW-CRDS to the study of biomolecules in a biologically relevant environment.

6.5 References

1. Kotyk, A., Biomembranes as catalysts of mass, energy and information-transfer. *Journal of Radioanalytical and Nuclear Chemistry-Articles* **1992,** *163* (1), 37-45.

2. McConnell, H. M.; Watts, T. H.; Weis, R. M.; Brian, A. A., Supported planar membranes in studies of cell-cell recognition in the immune-system. *Biochimica Et Biophysica Acta* **1986,** *864* (1), 95-106.

3. Kam, L. C., Capturing the nanoscale complexity of cellular membranes in supported lipid bilayers. *J Struct Biol* **2009,** *168* (1), 3-10; Perez, T. D.; Nelson, W. J.; Boxer, S. G.; Kam, L., E-cadherin tethered to micropatterned supported lipid bilayers as a model for cell adhesion. *Langmuir* **2005,** *21* (25), 11963-11968.

4. O'Rourke, B., Mitochondrial ion channels. *Annual Review of Physiology* **2007,** *69*, 19-49; Tien, H. T., Membrane photobiophysics and photochemistry. *Progress in Surface Science* **1989,** *30* (1-2), 1-199.

5. Ottova, A. L.; Tien, H. T., Bilayer lipid-membranes - an experimental system for biomolecular electronic devices development. *Progress in Surface Science* **1992,** *41* (4), 337-445.

6. Ottova, A. L.; Tien, H. T., Self-assembled bilayer lipid membranes: from mimicking biomembranes to practical applications. *Bioelectrochemistry and Bioenergetics* **1997,** *42* (2), 141-152.

7. Tien, H. T.; Wurster, S. H.; Ottova, A. L., Electrochemistry of supported bilayer lipid membranes: Background and techniques for biosensor development. *Bioelectrochemistry and Bioenergetics* **1997,** *42* (1), 77-94; Tien, H. T., Self-assembled lipid bilayers for biosensors and molecular electronic devices. *Advanced Materials* **1990,** *2* (6-7), 316-318; Nikolelis, D. P.; Siontorou, C. G., Bilayer-lipid membranes for flow-injection monitoring of acetylcholine, urea, and penicillin. *Analytical Chemistry* **1995,** *67* (5), 936-944; Buranda, T.; Huang, J.; Ramarao, G. V.; Ista, L. K.; Larson, R. S.; Ward, T. L.; Sklar, L. A.; Lopez, G. P., Biomimetic molecular assemblies on glass and mesoporous silica microbeads for biotechnology. *Langmuir* **2003,** *19* (5), 1654-1663.

8. Su, L. Y.; Hawkridge, F. M.; Rhoten, M. C., Electroreduction of oxygen by cytochrome *c* oxidase immobilized in electrode-supported lipid bilayer membranes. *Chemistry & Biodiversity* **2004,** *1* (9), 1281-1288.

9. Steinberg Yfrach, G.; Liddell, P. A.; Hung, S. C.; Moore, A. L.; Gust, D.; Moore, T. A., Conversion of light energy to proton potential in liposomes by artificial photosynthetic reaction centres. *Nature* **1997,** *385* (6613), 239-241; Steinberg-Yfrach, G.; Rigaud, J. L.; Durantini, E. N.; Moore, A. L.; Gust, D.; Moore, T. A., Light-driven production of ATP catalysed by F0F1-ATP synthase in an artificial photosynthetic membrane. *Nature* **1998,** *392* (6675), 479-482.

10. Khairutdinov, R. F.; Hurst, J. K., Cyclic transmembrane charge transport by pyrylium ions in a vesicle-based photocatalytic system. *Nature* **1999,** *402* (6761), 509-511; Chiantia, S.; Kahya, N.; Schwille, P., Dehydration damage of domain-exhibiting supported bilayers: An AFM study on the protective effects of disaccharides and other stabilizing substances. *Langmuir* **2005,** *21* (14), 6317-6323.

11. Krull, U. J., Planar artificial biomembranes optimized for biochemical assay. *Analytica Chimica Acta* **1987,** *197*, 203-215; Loidl-Stahlhofen, A.; Hartmann, T.; Schottner, M.; Rohring, C.; Brodowsky, H.; Schmitt, J.; Keldenich, J., Multilamellar liposomes and solid-supported lipid membranes (TRANSIL): Screening of lipid-water partitioning toward a high-throughput scale. *Pharmaceutical Research* **2001,** *18* (12), 1782-1788.

12. Mueller, P.; Rudin, D. O.; Tien, H. T.; Wescott, W. C., Reconstitution of cell membrane structure in vitro and its transformation into an excitable system. *Nature* **1962,** *194* (4832), 979.

13. Tien, H. T., Planar bilayer lipid-membranes. *Progress in Surface Science* **1985,** *19* (3), 169-274; Sackmann, E., Supported membranes: Scientific and practical applications. *Science* **1996,** *271* (5245), 43-48.

14. Lonez, C.; Vandenbranden, M.; Ruysschaert, J. M., Cationic liposomal lipids: From gene carriers to cell signaling. *Progress in Lipid Research* **2008,** *47* (5), 340-347; Safinya, C. R., Structures of lipid-DNA complexes: supramolecular assembly and gene delivery. *Current Opinion in Structural Biology* **2001,** *11* (4), 440-448.

15. Liu, J. W.; Stace-Naughton, A.; Jiang, X. M.; Brinker, C. J., Porous Nanoparticle Supported Lipid Bilayers (Protocells) as Delivery Vehicles. *Journal of the American Chemical Society* **2009,** *131* (4), 1354-+.

16. Generosi, J.; Piccinini, M.; Marcelli, A.; Belardinelli, S.; Pozzi, D.; Castellano, A. C., Characterization of solid supported lipoplexes by FTIR microspectroscopy. *Infrared Physics & Technology* **2007,** *50* (1), 14-20.

17. Desigaux, L.; Sainlos, M.; Lambert, O.; Chevre, R.; Letrou-Bonneval, E.; Vigneron, J. P.; Lehn, P.; Lehn, J. M.; Pitard, B., Self-assembled lamellar complexes of siRNA with lipidic aminoglycoside derivatives promote efficient siRNA delivery and interference. *Proceedings of the National Academy of Sciences of the United States of America* **2007,** *104*, 16534-16539.

18. Wurpel, G. W. H.; Sovago, M.; Bonn, M., Sensitive probing of DNA binding to a cationic lipid monolayer. *Journal of the American Chemical Society* **2007,** *129* (27), 8420; Fang, Y.; Yang, J., Two-dimensional condensation of DNA molecules on cationic lipid membranes. *Journal of Physical Chemistry B* **1997,** *101* (3), 441-449.

19. Castellana, E. T.; Cremer, P. S., Solid supported lipid bilayers: From biophysical studies to sensor design. *Surface Science Reports* **2006,** *61* (10), 429-444.

20. Barenholz, Y.; Gibbes, D.; Litman, B. J.; Goll, J.; Thompson, T. E.; Carlson, F. D., Simple Method for Preparation of Homogeneous Phospholipid Vesicles. *Biochemistry* **1977,** *16* (12), 2806-2810.

21. Maulucci, G.; De Spirito, M.; Arcovito, G.; Boffi, F.; Castellano, A. C.; Briganti, G., Particle size distribution in DMPC vesicles solutions undergoing different sonication times. *Biophysical Journal* **2005,** *88* (5), 3545-3550.

22. Lapinski, M. M.; Castro-Forero, A.; Greiner, A. J.; Ofoli, R. Y.; Blanchard, G. J., Comparison of liposomes formed by sonication and extrusion: Rotational and translational diffusion of an embedded chromophore. *Langmuir* **2007,** *23* (23), 11677-11683.

23. Mimms, L. T.; Zampighi, G.; Nozaki, Y.; Tanford, C.; Reynolds, J. A., Phospholipid vesicle formation and transmembrane protein incorporation using octyl glucoside. *Biochemistry* **1981,** *20* (4), 833-840; Graneli, A.; Rydstrom, J.; Kasemo, B.; Hook, F., Formation of supported lipid bilayer membranes on SiO_2 from proteoliposomes containing transmembrane proteins. *Langmuir* **2003,** *19* (3), 842-850; Salafsky, J.; Groves, J. T.; Boxer, S. G., Architecture and function of membrane proteins in planar supported bilayers: A study with photosynthetic reaction centers. *Biochemistry* **1996,** *35* (47), 14773-14781.

24. Reimhult, E.; Hook, F.; Kasemo, B., Vesicle adsorption on SiO_2 and TiO_2: Dependence on vesicle size. *Journal of Chemical Physics* **2002,** *117* (16), 7401-7404.

25. Pfeiffer, I.; Seantier, B.; Petronis, S.; Sutherland, D.; Kasemo, B.; Zaech, M., Influence of Nanotopography on Phospholipid Bilayer Formation on Silicon Dioxide. *J. Phys. Chem. B* **2008,** *112* (16), 5175-5181.

26. Seantier, B.; Kasemo, B., Influence of Mono- And Divalent Ions on the Formation of Supported Phospholipid Bilayers via Vesicle Adsorption. *Langmuir* **2009,** *25* (10), 5767-5772.

27. Boudard, S.; Seantier, B.; Breffa, C.; Decher, G.; Felix, O., Controlling the pathway of formation of supported lipid bilayers of DMPC by varying the sodium chloride concentration. *Thin Solid Films* **2006,** *495* (1-2), 246-251.

28. Pereira, E. M. A.; Petri, D. F. S.; Carmona-Ribeiro, A. M., Adsorption of cationic lipid bilayer onto flat silicon wafers: Effect of ion nature and concentration. *Journal of Physical Chemistry B* **2006,** *110* (20), 10070-10074.

29. Seantier, B.; Breffa, C.; Felix, O.; Decher, G., Dissipation-Enhanced Quartz Crystal Microbalance Studies on the Experimental Parameters Controlling the Formation of Supported Lipid Bilayers. *J. Phys. Chem. B* **2005,** *109* (46), 21755-21765.

30. Seantier, B.; Breffa, C.; Felix, O.; Decher, G., In situ investigations of the formation of mixed supported lipid bilayers close to the phase transition temperature. *Nano Letters* **2004,** *4* (1), 5-10.

31. Richter, R. P.; Berat, R.; Brisson, A. R., Formation of solid-supported lipid bilayers: An integrated view. *Langmuir* **2006,** *22* (8), 3497-3505.

32. Richter, R.; Mukhopadhyay, A.; Brisson, A., Pathways of lipid vesicle deposition on solid surfaces: A combined QCM-D and AFM study. *Biophysical Journal* **2003,** *85* (5), 3035-3047.

33. Mardilovich, A.; Kokkoli, E., Patterned biomimetic membranes: Effect of concentration and pH. *Langmuir* **2005,** *21* (16), 7468-7475; Nikolov, V.; Lin, J.; Merzlyakov, M.; Hristova, K.; Searson, P. C., Electrical measurements of bilayer membranes formed by Langmuir-Blodgett deposition on single-crystal silicon. *Langmuir* **2007,** *23* (26), 13040-13045; Li, M.; Chen, M.; Sheepwash, E.; Brosseau, C. L.; Li, H.; Pettinger, B.; Gruler, H.; Lipkowski, J., AFM studies of solid-supported lipid bilayers formed at a Au(111) electrode surface using vesicle fusion and a combination of Langmuir-Blodgett and Langmuir-Schaefer techniques. *Langmuir* **2008,** *24* (18), 10313-10323; Dominska, M.; Krysinski, P.; Blanchard, G. J., Interrogating interfacial organization in planar bilayer structures. *Langmuir* **2008,** *24* (16), 8785-8793.

34. Liu, J.; Conboy, J. C., Structure of a gel phase lipid bilayer prepared by the Langmuir-Blodgett/Langmuir-Schaefer method characterized by sum-frequency vibrational spectroscopy. *Langmuir* **2005,** *21* (20), 9091-9097.

35. Purrucker, O.; Fortig, A.; Jordan, R.; Tanaka, M., Supported membranes with well-defined polymer tethers-incorporation of cell receptors. *Chemphyschem* **2004,** *5* (3), 327-335; Kalb, E.; Frey, S.; Tamm, L. K., Formation of supported planar bilayers by fusion of vesicles to supported phospholipid monolayers. *Biochimica Et Biophysica Acta* **1992,** *1103* (2), 307-316.

36. Domenici, F.; Castellano, C.; Congiu, A.; Pompeo, G.; Felici, R., Ordering and lyotropic behavior of a silicon-supported cationic and neutral lipid system studied by neutron reflectivity. *Applied Physics Letters* **2008,** *92* (19), 3.

37. Pompeo, G.; Girasole, M.; Cricenti, A.; Cattaruzza, F.; Flamini, A.; Prosperi, T.; Generosi, J.; Castellano, A. C., AFM characterization of solid-supported lipid multilayers

prepared by spin-coating. *Biochimica Et Biophysica Acta-Biomembranes* **2005,** *1712* (1), 29-36.

38. Generosi, J.; Castellano, C.; Pozzi, D.; Castellano, A. C.; Felici, R.; Natali, F.; Fragneto, G., X-ray and neutron reflectivity study of solid-supported lipid membranes prepared by spin coating. *Journal of Applied Physics* **2004,** *96* (11), 6839-6844.

39. Mager, M. D.; Almquist, B.; Melosh, N. A., Formation and Characterization of Fluid Lipid Bilayers on Alumina. *Langmuir* **2008,** *24* (22), 12734-12737; Mager, M. D.; Melosh, N. A., Lipid bilayer deposition and patterning via air bubble collapse. *Langmuir* **2007,** *23* (18), 9369-9377.

40. Richter, R. P.; Brisson, A. R., Following the formation of supported lipid bilayers on mica: A study combining AFM, QCM-D, and ellipsometry. *Biophysical Journal* **2005,** *88,* 3422-3433.

41. Reimhult, E.; Zach, M.; Hook, F.; Kasemo, B., A multitechnique study of liposome adsorption on Au and lipid bilayer formation on SiO_2. *Langmuir* **2006,** *22* (7), 3313-3319.

42. Knoll, W.; Koper, I.; Naumann, R.; Sinner, E. K., Tethered bimolecular lipid membranes - A novel model membrane platform. *Electrochimica Acta* **2008,** *53* (23), 6680-6689.

43. Keller, C. A.; Kasemo, B., Surface specific kinetics of lipid vesicle adsorption measured with a quartz crystal microbalance. *Biophysical Journal* **1998,** *75* (3), 1397-1402.

44. Viitala, T.; Hautala, J. T.; Vuorinen, J.; Wiedmer, S. K., Structure of anionic phospholipid coatings on silica by dissipative quartz crystal microbalance. *Langmuir* **2007,** *23* (2), 609-618.

45. Zhang, L. Q.; Longo, M. L.; Stroeve, P., Mobile phospholipid bilayers on a polyion/alkylthiol layer pair. *Langmuir* **2000,** *16* (11), 5093-5099; Rossi, C.; Briand, E.; Parot, P.; Odorico, M.; Chopineau, J., Surface response methodology for the study of supported membrane formation. *Journal of Physical Chemistry B* **2007,** *111* (26), 7567-7576; Jonsson, M. P.; Joensson, P.; Hoeoek, F., Simultaneous Nanoplasmonic and Quartz Crystal Microbalance Sensing: Analysis of Biomolecular Conformational Changes and Quantification of the Bound Molecular Mass. *Anal. Chem. (Washington, DC, U. S.)* **2008,** *80* (21), 7988-7995.

46. Keller, C. A.; Glasmastar, K.; Zhdanov, V. P.; Kasemo, B., Formation of supported membranes from vesicles. *Physical Review Letters* **2000,** *84* (23), 5443-5446.

47. Shao, Y.; Jin, Y. D.; Wang, J. L.; Wang, L.; Zhao, F.; Dong, S. J., Conducting polymer polypyrrole supported bilayer lipid membranes. *Biosensors & Bioelectronics* **2005,** *20* (7), 1373-1379.

48. Egawa, H.; Furusawa, K., Liposome adhesion on mica surface studied by atomic force microscopy. *Langmuir* **1999,** *15* (5), 1660-1666; Dufrene, Y. F.; Lee, G. U., Advances in the characterization of supported lipid films with the atomic force microscope. *Biochimica Et Biophysica Acta-Biomembranes* **2000,** *1509* (1-2), 14-41.

49. Kim, Y. H.; Rahman, M. M.; Zhang, Z. L.; Misawa, N.; Tero, R.; Urisu, T., Supported lipid bilayer formation by the giant vesicle fusion induced by vesicle-surface electrostatic attractive interaction. *Chemical Physics Letters* **2006,** *420* (4-6), 569-573.

50. Richter, R. P.; Brisson, A., QCM-D on mica for parallel QCM-D-AFM studies. *Langmuir* **2004,** *20* (11), 4609-4613.

51. Reinl, H. M.; Bayerl, T. M., Lipid transfer between small unilamellar vesicles and single bilayers on a solid support - self-assembly of supported bilayers with asymmetric lipid distribution. *Biochemistry* **1994,** *33* (47), 14091-14099; Erbe, A.; Bushby, R. J.; Evans, S. D.; Jeuken, L. J. C., Tethered bilayer lipid membranes studied by simultaneous attenuated total reflectance infrared spectroscopy and electrochemical impedance spectroscopy. *Journal of Physical Chemistry B* **2007,** *111* (13), 3515-3524.

52. Benes, M.; Billy, D.; Benda, A.; Speijer, H.; Hof, M.; Hermens, W. T., Surface-dependent transitions during self-assembly of phospholipid membranes on mica, silica, and glass. *Langmuir* **2004,** *20* (23), 10129-10137.

53. Majewski, J.; Wong, J. Y.; Park, C. K.; Seitz, M.; Israelachvili, J. N.; Smith, G. S., Structural studies of polymer-cushioned lipid bilayers. *Biophysical Journal* **1998,** *75* (5), 2363-2367; Vacklin, H. P.; Tiberg, F.; Fragneto, G.; Thomas, R. K., Composition of supported model membranes determined by neutron reflection. *Langmuir* **2005,** *21* (7), 2827-2837.

54. Kucerka, N.; Nagle, J. F.; Sachs, J. N.; Feller, S. E.; Pencer, J.; Jackson, A.; Katsaras, J., Lipid bilayer structure determined by the simultaneous analysis of neutron and x-ray scattering data. *Biophysical Journal* **2008,** *95* (5), 2356-2367.

55. Generosi, J.; Margaritondo, G.; Sanghera, J. S.; Aggarwal, I. D.; Tolk, N. H.; Piston, D. W.; Castellano, A. C.; Cricenti, A., Spectroscopic infrared near-field microscopy and x-ray reflectivity studies of order and clustering in lipid membranes. *Applied Physics Letters* **2006,** *89* (23), 3.

56. Lee, C. S.; Bain, C. D., Raman spectra of planar supported lipid bilayers. *Biochimica Et Biophysica Acta-Biomembranes* **2005,** *1711* (1), 59-71.

57. Kraft, M. L.; Weber, P. K.; Longo, M. L.; Hutcheon, I. D.; Boxer, S. G., Phase separation of lipid membranes analyzed with high-resolution secondary ion mass spectrometry. *Science* **2006,** *313* (5795), 1948-1951.

58. Zhang, L. F.; Spurlin, T. A.; Gewirth, A. A.; Granick, S., Electrostatic stitching in gel-phase supported phospholipid bilayers. *Journal of Physical Chemistry B* **2006,** *110* (1), 33-35; Reviakine, I.; Brisson, A., Formation of supported phospholipid bilayers from unilamellar vesicles investigated by atomic force microscopy. *Langmuir* **2000,** *16* (4), 1806-1815; Burns, A. R., Domain structure in model membrane bilayers investigated by simultaneous atomic force microscopy and fluorescence imaging. *Langmuir* **2003,** *19* (20), 8358-8363.

59. Hochrein, M. B.; Reich, C.; Krause, B.; Radler, J. O.; Nickel, B., Structure and mobility of lipid membranes on a thermoplastic substrate. *Langmuir* **2006,** *22* (2), 538-545; Hull, M. C.; Cambrea, L. R.; Hovis, J. S., Infrared spectroscopy of fluid lipid bilayers. *Analytical Chemistry* **2005,** *77* (18), 6096-6099.

60. Anderson, T. H.; Min, Y. J.; Weirich, K. L.; Zeng, H. B.; Fygenson, D.; Israelachvili, J. N., Formation of Supported Bilayers on Silica Substrates. *Langmuir* **2009,** *25* (12), 6997-7005.

61. Zhdanov, V. P.; Kasemo, B., Comments on rupture of absorbed vesicles. *Langmuir* **2001,** *17* (12), 3518-3521; Hamai, C.; Yang, T. L.; Kataoka, S.; Cremer, P. S.; Musser, S. M., Effect of average phospholipid curvature on supported bilayer formation on glass by vesicle fusion. *Biophysical Journal* **2006,** *90* (4), 1241-1248.

62. Fan, H. F.; Li, F.; Zare, R. N.; Lin, K. C., Characterization of Two Types of Silanol Groups on Fused-Silica Surfaces Using Evanescent-Wave Cavity Ring-Down Spectroscopy. *Anal. Chem.* **2007,** *79* (10), 3654-3661.

Chapter 7. Conclusions and Outlook

In this thesis we have demonstrated the first steps towards applying EW-CRDS with electrochemical and fluidic methods to the study of biologically relevant processes. In all experiments described herein, electrochemical or microfluidic methods were used as a means to induce surface processes which could then be followed in real-time and *in situ* using EW-CRDS. The spectral sensitivity of EW-CRDS allowed the detection of submonolayer concentrations of molecules at the silica-water interface, at wavelengths often removed from the peak in the absorption spectrum (see Chapter 3), without the need to label (as in fluorescence spectroscopy) or the use of biologically unfriendly metal layers such as those used in SPR.

The well-defined delivery methods employed in the experiments described in this thesis allowed the development of mathematical models of the underlying physics, which were used to fit the experimental data, to further understand the reaction mechanisms and extract rate constants where appropriate (in Chapters 4, 5 and 6), or allowed the use of other surface science techniques to provide further information on the processes studied (namely the use of CLSM as described in Chapter 3). Furthermore, the use of flow — as described in Chapters 5 and 6 — should enable the study of exceptionally fast processes.

One of the key results of Chapter 3 was one of the first demonstrations of the modification of the prism inherent in the EW-CRDS set-up in order to investigate a wider range of surface interactions. Although simple in concept, this initial set of experiments on the adsorption of $[Ru(bpy)_3]^{2+}$ to polyelectrolyte-modified silica has opened up a wide-range of possible interactions that could be studied using EW-CRDS with

electrochemistry. In Chapter 6, the ability to form a supported lipid bilayer on the prism surface was demonstrated, and more importantly, the possibility of studying interactions with the bilayer was investigated. This has huge potential for the study of the interactions of proteins, ions, drugs with biomembranes and for the optimisation of biofilms for use in biosensors, biofuel cells and bioeletronics.

In Chapter 4, the redox properties of surface immobilised cytochrome *c* were investigated using EW-CRDS with chronoamperometry. Oxidised cytochrome *c* on silica was reduced by a solution based redox mediator whose redox state was controlled by an electrode. The reduction of the cytochrome *c* was monitored in real time by the EW-CRDS signal using the difference in the absorbance cross-sections of reduced and oxidised cytochrome *c* at 400 nm, and fits to the experimental data allowed the extraction of the electron transfer rate constant. This study is particularly exciting as it could easily be extended to the study of the electron transfer between proteins and mediators or proteins and proteins in a biomimetic environment such as adsorbed to a supported lipid bilayer on the prism surface. Such an approach could be complementary to protein voltammetry to study electron transfer to proteins in which communication between electrode and protein is difficult.

In Chapter 5, the study of the DNA-assisted TMPyP desorption from a silica surface was initially intended as a means to study the interaction between TMPyP and DNA for the development of a sensor for DNA. Although this goal was not realised in this particular EW-CRDS set-up, the development of a DNA sensor using other EW-CRDS configurations, notably the fibre loop configuration discussed in Section 1.3, is still a possibility. Further studies on the interaction of porphyrins with different DNA

sequences could determine whether such a sensor could be made selective as well as sensitive. This study has also shown that EW-CRDS could still prove useful for the study of biomolecule interactions. This field is currently dominated by the use of SPR and QCM, but there is no reason why EW-CRDS could not be complementary to these techniques. The sensitivity of EW-CRDS means that it could be used to detect the interaction of small analytes that cannot be detected using SPR, and the ability to monitor spectral changes rather than refractive index or mass changes could help identify structures formed on the surface or conformational changes induced on binding.

The EW-CRDS set-up described in this thesis represents arguably the simplest variation of the technique and has clearly provided a starting point for the study of biological interfaces, however work is being undertaken in our laboratory and by our collaborators, led by Dr. Stuart Mackenzie at Oxford University, to develop more sophisticated variations of the technique. As briefly mentioned in Chapters 1, 2 and 5, an EW-CRDS set-up that can perform polarisation-dependent measurements has been built. This allows the determination of the orientation of molecules at the interface which is important for the characterisation of biofilms in technologies such as biosensors, and may prove useful in the identification of structures formed at the interface.

Another EW-CRDS variant being developed by our collaborators in Oxford, which is expected to provide significant improvements on the existing set-up, is evanescent wave cavity enhanced broadband absorption spectroscopy. This will allow the monitoring of the evolution of entire spectra in real time during a surface process with improved sensitivity over conventional absorption spectroscopic techniques.

It is planned to use EW-CRDS to study chemical propagation laterally across surfaces by employing a UME or micropipette to locally deliver materials to the surface in the evanescent field. As the material diffuses laterally within the evanescent field, a change in absorption would be expected as the concentration changes across the evanescent wave profile. The lateral diffusion of protons, ions or even proteins could be studied in this way.

Finally, the experiments in Chapter 4 demonstrated the ability to couple a femtosecond laser pulse into the EW-CRDS which opens up the possibility to study ultra fast dynamics. This is currently being investigated in collaboration with Dr. Vasilios Stavros in the Chemistry Department at Warwick.